HYDRATE SLURRY AS COLD ENERGY STORAGE AND DISTRIBUTION MEDIUM

ENHANCING THE PERFORMANCE OF REFRIGERATION SYSTEMS

HYDRATE SLURRY AS COLD ENERGY STORAGE AND DISTRIBUTION MEDIUM

ENHANCING THE PERFORMANCE OF REFRIGERATION SYSTEMS

Proefschrift

ter verkrijging van de graad van doctor
aan de Technische Universiteit Delft,
op gezag van de Rector Magnificus prof. ir. K.C.A.M. Luyben
voorzitter van het College voor Promoties,
in het openbaar te verdedigen op maandag 8 mei 2017 om 10:00 uur

door

Hongxia ZHOU

Master of Science, Guangzhou Institute of Energy Conversion,
Chinese Academy of Science, China
geboren te Shijiazhuang, Hebei, China.

Dit proefschrift is goedgekeurd door de

promotor: Prof. dr. ir. T.J.H. Vlugt
copromotor: Dr. ir. C.A. Infante Ferreira

Samenstelling promotiecommissie:

Rector Magnificus,	voorzitter
Prof. dr. ir. T.J.H. Vlugt	Promotor
Dr. ir. C.A. Infante Ferreira	Copromotor
Onafhankelijke leden:	
Prof. dr. A. Coronas	Universiteit Rovira I Virgili, Tarragona, Spain
Prof. dr. ir. A.A. van Steenhoven	Technische Universiteit Eindhoven
Dr. ir. P. Pronk	Tata Steel, Ijmuiden
Prof. dr. ir. B.J. Boersma	Technische Universiteit Delft
Prof. dr. ir. D.J.E.M. Roekaerts	Technische Universiteit Delft

The author would like to thank KoudeGroup Delft/Wageningen for their financial support. The author would also want to thank Guangzhou Elite Project of Guangzhou Municipal Government for their financial support.

Keywords: Hydrate slurry, Air conditioning, Growth model, Energy efficiency

Printed by: Ridderprint BV

ISBN 978-94-6299-595-6

An electronic version of this dissertation is available at
`http://repository.tudelft.nl/`.

To my parents,
my beloved husband Yuewei Ma

CONTENTS

III CO_2 hydrate slurry 93

4 CO_2 hydrate slurry production in a FBHE 95

NOMENCLATURE

List of symbols

A	Area, m^2
a	Lattice constant in Eq.(4.5)
$A^{'}$	Coefficient in Eq.(3.2)
B	Guest molecule
c_p	Specific heat, $\mathrm{J\ kg^{-1}\ K^{-1}}$
c_r	Circulation ratio
d	Diameter, m
D_c	Coil diameter, m
D	Diffusion coefficient, $\mathrm{m^2\ s^{-1}}$
d_h	Hydraulic diameter, m
f	Friction factor
$\dot{G}$	Mass flux, $\mathrm{kg\ m^{-2}\ s^{-1}}$
G	Growth rate, $\mathrm{kg\ s^{-1}}$
g	Gravity constant, $\mathrm{m\ s^{-2}}$
G_lin	Linear growth rate, $\mathrm{m\ s^{-1}}$
H	Height, m
h	Enthalpy, $\mathrm{J\ kg^{-1}}$
K	Loss coefficient
k	Mass transfer coefficient, $\mathrm{m\ s^{-1}}$
$K^{'}$	Coefficient in Eq. (2.22)

L	Length, m
M	Molecular weight, kg kmol^{-1}
m	Mass, kg
$\dot{m}$	Mass flow rate, kg s^{-1}
N	Number of molecules
n	Exponent in Eq. (2.22)
N_{cp}	Number of passes
N_0	Avogadro constant in Eq. (4.5)
N_r	Number of tubes in air flow direction
N_t	Number of tubes perpendicular to air flow direction
P	Pressure, Pa
p	Pitch
p_{fin}	Fin pitch, m
$\dot{Q}$	Heat flow, J s^{-1}
$\dot{q}$	Heat flux, J s^{-1} m^{-2}
Q	Energy, J
q	Vapor quality
R	Thermal Resistance, m^2 K W^{-1}
R_p	Roughness, μm
s_{fin}	Fin spacing, m
T	Temperature, °C
t	Time, s
U	Overall heat transfer coefficient, W m^{-2} K^{-1}
u	Velocity, m s^{-1}
$\dot{V}$	Volume flow, m^3 s^{-1}

V	Volume, m^3
W	Power, kW
w	Mass fraction
W_{fin}	Fin thickness, m
x	Molar fraction, $\mathrm{kmol\,kmol^{-1}}$
z	Axial coordinate

Dimensionless Number

Ar	Archimedes number, $= {\frac{gL^3\rho_L(\rho_v-\rho_L)}{\mu_L}}^2$
Bo	Boiling number $= \frac{\dot{Q}/A}{\dot{G}_{eq}\Delta h_{lat}}$
De	Dean number $= \mathrm{Re}\sqrt{\frac{d_i}{D_c}}$
Nu	Nusselt number $= \frac{\alpha d_i}{\lambda}$
Pr	Prandtl number $= \dfrac{c_p\mu}{\lambda}$
Ra_H	Rayleigh number $= g\beta\Delta T H^3\mathrm{Pr}(\frac{\mu}{\rho})^{-2}$
Re_h	Hydraulic Reynolds number, $= \rho u d_{\mathrm{ps}}(\mu(1-\varepsilon))^{-1}$
Re	Reynolds number, $= \frac{\rho d u}{\mu}$
Re_M	Modified Reynolds number, $= \frac{d_i^n u^{2-n}\rho_s}{8^{n-1}K'}$
Sc	Schmidt number, $= \frac{\mu}{\rho D}$
Sh	Sherwood number, $= \frac{kL}{D}$
Ste	Stefan number, $\frac{c_{ps}\dot{q}d_i}{w\Delta h\lambda_s}$

Greek

α	Heat transfer coefficient, $\mathrm{W\,m^{-2}\,K^{-1}}$
β	Thermal expansion coefficient, 1/°C

Δ	Difference
δ	Thickness, m
ϵ	Bed porosity
η	Efficiency
λ	Thermal conductivity, W m^{-1} K^{-1}
μ	Viscosity, Pa s^{-1}
ϕ	Volume fraction
ρ	Density, kg m^{-3}

Subscripts

av	Average
b	Bulk
c	Coil
comp	Compressor
crit	Critical
elec	Electric
eq	Equilibrium/Equivalent
evap	Evaporation
exp	Experimental
fb	Fluidized bed
H	Hydrate
h	Hydraulic
hex	Heat exchanger
i	Internal
in	Inlet
int	Interface

is	Isentropic
L	Liquid
lam	Laminar
lat	Latent
lin	Linear
log	Logarithmic
m	Melting
max	Maximum
mech	Mechanical
o	Outside
out	Outlet
p	Crystal particle
pb	Packed bed
phe	Plate heat exchanger
pred	Predicted
ps	Stainless steel particle
r	Rows
rat	Ratio
ref	Refrigerant
s	Slurry
sat	Saturation
solid	Solid
sol	Solution
sp	Single phase
str	Straight

sup	Superheating
sv	Storage Vessel
t	Tube
tot	Total
turb	Turbulent
v	Vapor
vol	Volumetric
w	Wall

Superscript

$*$	Equilibrium
a'	Coefficient in Eq.(3.2)
b'	Coefficient in Eq.(3.2)
j	Control volume number
t	Time, s

Abbreviations

AFPs	Antifreeze proteins
CFCs	Chlorofluorocarbons
CHS	Clathrate hydrate slurry
COP	Coefficient of performance
DHW	Domestic hot water
EIA	Energy information administration
FBHE	Fluidized bed heat exchanger
GDP	Gross domestic product
HCFCs	Hydrochlorofluorocarbons
HVAC	Heating, ventilation, air-conditioning

IEA	International energy agency
KHI	Kinetic hydrate inhibitor
LHTS	Latent heat thermal storage
PCMs	Phase change materials
PHE	Plate heat exchanger
poly(VP/VC)	N-Vinyl pyrrolidone-co-N-Vinyl caprolactam
PVCap	Polyvinyl Caprolactam
PVP	Polyvinyl Pyrrolidone
Py14-Br	N-butyl-N-methylpyrrolidinium
SHS	Sensible heat storage
SV	Storage vessel
TBAB	Tetra-n-butylammonium bromide
TES	Thermal energy storage
THF	Tetrahydrofuran
THIs	Thermodynamic Hydrate Inhibitors
TPES	Total primary energy supply

I

BACKGROUND

1

INTRODUCTION

This chapter introduces the background of this work, including the importance of applying cold storage systems in refrigeration and air-conditioning systems, the fundamentals of hydrate slurry as well as a review of hydrate slurry generation technology. In the end, the objectives and scope of this thesis are given.

1.1. IMPORTANCE OF COLD STORAGE

The world energy use has been raising concerns due to its rapid growth. Fig. 1.1 shows the energy growth from the year 1971 to the year of 2014. It indicates the total primary energy supply (TPES) of the 34 members of the organization for Economic Co-operation and development increased about 58% during the period of 1971 - 2014. The reason for the concerns about the energy growth includes supply difficulties, exhaustion of energy resources and heavy environmental impacts [82] (global warming, climate change, etc). The CO_2 emissions caused by the growth of energy consumption have increased by 51% from the year of 1990 to the year of 2012, according to the data gathered by the International Energy Agency (Fig.1.2). It shows the increase of CO_2 emission is driven by four factors: population, GDP (Gross domestic product)/population, TPES/GDP and CO_2 emission/TPES. Current predictions from the two figures show that the global energy demand and CO_2 emission growing trends will continue.

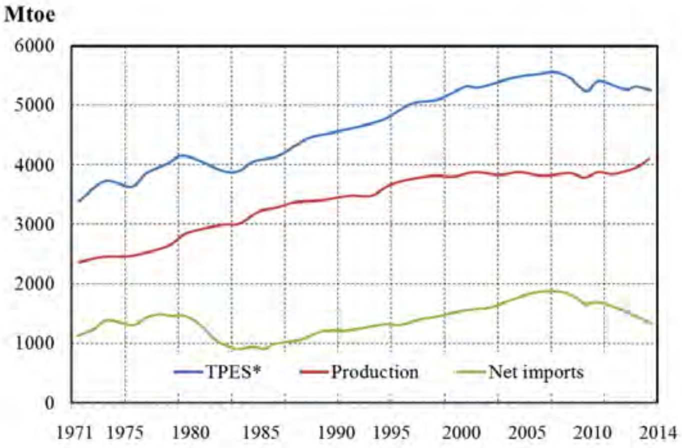

Figure 1.1: Primary energy supply increase from the year 1971 to 2014. The energy production and net imports are also shown in the figure. *TPES: total primary energy supply. Data taken from the International Energy Agency (IEA) [44]

The building sector contributes immensely to the total energy consumption, particularly for its space conditioning and domestic hot water [73]. Energy use and emissions result from both direct sources, such as fossil fuels, and indirect sources (heating, cooling, electricity and energy embodied in different construction materials [77]). It has been reported by the International Energy Agency (IEA) [44] that the energy consumption in the building sector in developed countries is consuming over 40% of the global energy with 24% of greenhouse gas emissions. For instance, the building consumption in Europe was 40% of the

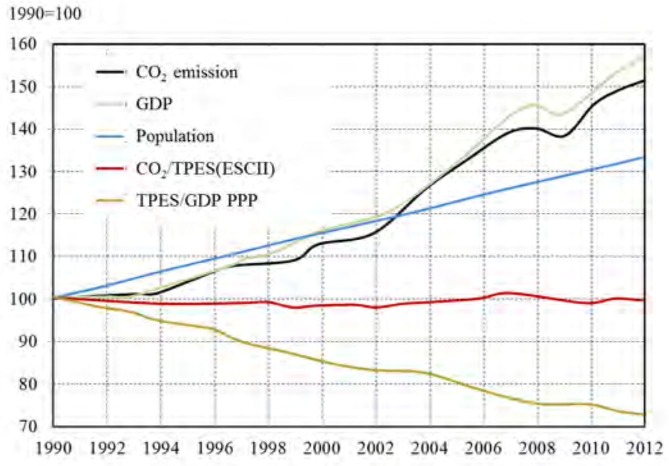

Figure 1.2: CO_2 emission driven by four factors. Data taken from the International Energy Agency (IEA) [44]

total energy consumption according to the Energy Information Administration (EIA) in the year of 2012. Within the energy consumption of the buildings, HVAC (Heating, Ventilation and Air-conditioning) is the major consumer among others (Domestic hot water (DHW); Lighting and appliances). It has now become especially essential due to the demand for thermal comfort. It is the largest energy end use both in residential and non-residential sectors ([82]). The increasing demand of energy has prompted the need for a reduction on CO_2 emissions via significant increase in energy efficiency of buildings. Renewable energy resources have massive energy potential but are not always fully accessible. To sustain economic growth, issues relating to the supply and efficient use of energy must be addressed in the design of low energy buildings and sustainable cities. Central to the problem is the need to store excess energy that would otherwise be wasted and also to bridge the gap between energy generation and consumption as well as shifting peak power demand. In this study, air-conditioning systems are investigated for what concerns the possibility of energy savings.

Air-conditioning is the control of air conditions in, for example, buildings, cars and trains. This is also, called 'climate control'. An air-conditioning system is used to set the temperature and humidity of air in a space to a comfortable level. Especially in high environmental temperature periods the demand of cooled air is high. Air-conditioning systems are used all over the world and have a direct impact on the global energy demand.

Many alternative refrigerants have been commercially introduced to substitute CFCs and HCFCs etc., because of ozone depletion problems. However, there are some defects of the alternative refrigerants including flammability, toxicity, potential metal corrosion and compatibility with oil, which restrict their use [98]. The combination of primary refrigerants with secondary-loop refrigeration is regarded as a solution to overcome the problems aforementioned which have been reported among others by Shi and Zhang (2013) [98]. In the secondary-loop distribution system, environment-friendly working fluids can be employed to store low temperature energy and to distribute it to the different application sites. In this way the amount of primary refrigerant charged to the system is significantly reduced in comparison to conventional distributed direct expansion systems resulting in much smaller leakage risk. Also, the primary refrigerant can be maintained in restricted spaces, again limiting the risk to the environment. Low temperature energy storage can be easily included in secondary-loop refrigeration and air-conditioning systems and is an effective method to shift peak electric load to off-peak time as part of the strategy for energy management in buildings. It also contributes to a reduction of installed power and allows for night time operation when lower heat rejection temperatures are available for the primary refrigeration cycle. High energy storage density and high power capacity for charging and discharging are desirable properties of any storage system [80]. There are three methods of thermal energy storage (TES) in general: sensible, latent and thermal chemical energy storage.

Sensible heat storage (SHS) involves storing thermal energy by raising the temperature of a solid or liquid. The principle is based on temperature change during the process of charging and discharging [58]. The amount of heat storage, is a function of the specific heat of the medium, the temperature change and the mass of the storage medium [58]. In Eq. (1.1), the specific heat of the medium is assumed to be temperature independent.

$$Q = \int_{T_1}^{T_2} mc_p dT = mc_p(T_2 - T_1) \tag{1.1}$$

Latent heat thermal storage (LHTS) relies on the storage material absorbing or releasing heat as it undergoes a solid to solid, solid to liquid or liquid to gas phase change or vice versa [58]. The storage capacity can be given by Eq. 1.2 from Lane (1985) [58].

$$Q = \int_{T_1}^{T_m} mc_{p_{solid}} dT + mw_m \Delta h_m + \int_{T_m}^{T_2} mc_{p_L} dT \tag{1.2}$$

Latent heat thermal storage (LHTS) is a particularly attractive technique because it provides a high energy storage density. When compared to a conventional sensible heat energy storage system, latent heat energy storage requires a smaller mass and volume of material for a given amount of energy [4]. Thermochemical materials store and release heat by a reversible endothermic / exothermic reaction process. This technology has to overcome important barriers such as corrosion, poor heat and mass transfer performance and materials development [16]. Nowadays, the need for the thermal energy storage in industrial and residential buildings is growing steadily with the increase of energy consumption [7]. Thermal storage systems appear to be the only solution to correct the mismatch between supply and demand of energy [20]. Fig. 1.3 shows the process of a thermal storage system in comparison with a conventional system. In the conventional system, the chiller operates only when the building occupants require cold air. In TES systems, the chiller also operates at times other than when the cooling is need [21]. The utilization of thermal energy storage (TES) ranges from heating to cooling, especially in buildings. Combined with solar heating, hot water and cooling applications in buildings, TES systems have attracted much interest in recent years [19], especially for the regions where there is a large difference between day and night temperature.

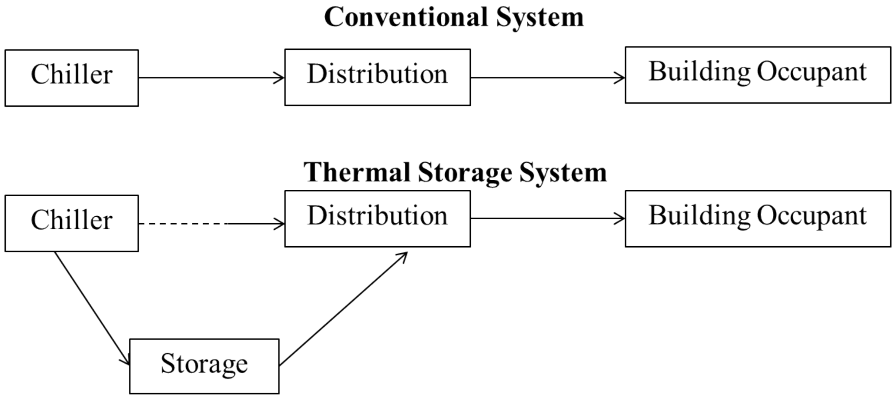

Figure 1.3: Components of cooling for conventional system and TES system: The chiller is the component where the solution is cooled down. ⟶ denotes the flow direction.

The majority of the thermal storage installations makes use of chilled water and ice storage systems. The applications of TES begun to appear in Asia, Australia, Europe and South America since mid-1990s. The advantage of applying TES can be seen from an example in the Netherlands: a ground water aquifer TES system was installed as a innovative space conditioning unit in an office of ANOVA Verzekering Co. [19] in the Netherlands. The energy saving and emissions reductions are shown in Table 1.1.

Table 1.1: The savings and reductions of natural gas, electricity, primary energy, and CO_2 for a ground water aquifer TES system in comparison with a conventional system in the Netherlands [19].

Annual consumptions and emissions	Conventional system	TES system	Reduction
Natural gas (m^3)	215800	95500	120300 (56%)
Electricity (kWh)	395550	511500	-84000 (-21%)
Primary energy (m^3)	322000	179000	143000 (44%)
CO_2 (kg)	608000	346000	262000 (43%)

*The primary energy is calculated as the equivalent amount of natural gas on the basis of the assumption that 0.25 m^3 gas is used in the generation of 1 kWh of electricity.

1.2. PHASE CHANGE MATERIALS AS COLD STORAGE MEDIA

Water is commonly used as low temperature heat storage and distribution fluid as a secondary-loop refrigerant between chiller and the application site. In water systems, water is cooled down from 12 °C to 7 °C in the evaporator of the chiller with an evaporation temperature of around 2 °C. In the application heat exchangers, water is then heated up from 7 to 12 °C while air is cooled from, for example, 30 °C to 18 °C, as shown in Fig. 1.4. Evaporating at temperature of 2 °C for the production of air of 18°C can be improved. In addition, the use of water as storage medium leads to large storage volumes because in the water systems only sensible heat is used. Additionally, the pumping power of the chilled water consumes large amounts of energy.

The interest in using phase change ice slurry coolants has grown significantly in the past twenty years. The utilization of ice slurry has been widely investigated over the world from the fundamental thermal properties to the practical applications [129]. Ice slurry, composed of ice and water, has a high energy storage density because of the latent heat of fusion of its ice crystals. During the cooling process, the ice slurry maintains a constant low temperature level, and provides a higher heat transfer coefficient than water or other single-phase liquids [30]. It has been widely used as a medium for latent heat cold storage due to the properties mentioned above. However, due to the freezing point depression by additives, the cold storage air-conditioning systems using ice slurry require temperatures below 0 °C for ice generation. Consequently, the cold charging process is very energy-consuming due to the required low evaporation temperature, resulting in a low energy efficiency of the system [54].

Phase change materials (PCMs) are promising cold storage media for air conditioning systems, heating and cooling applications due to the high energy storage density and capacity to store energy at constant or near constant temper-

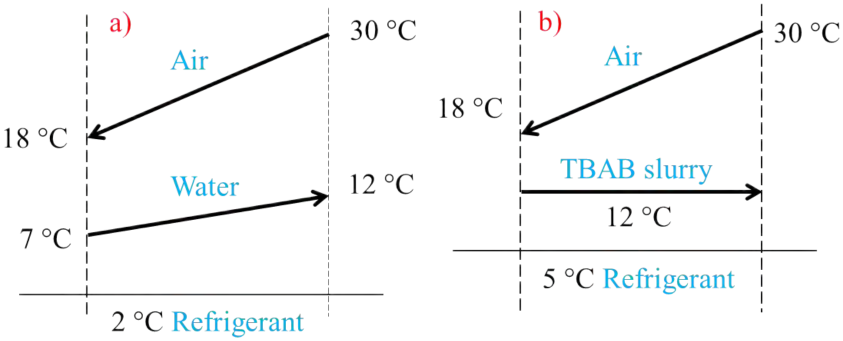

Figure 1.4: a) Principle of water cooling air-conditioning system: In order to cool down the room air temperature from 30 °C to 18 °C, water is heated from 7 °C to 12 °C, with an evaporation temperature of 2 °C; b) Principle of air-conditioning system making use of slurry: TBAB slurry maintains a constant temperature of 12 °C to cool down the same room temperature with an evaporation temperature of 5 °C.

ature. Many authors have carried out investigation into a wide range of PCMs, subdividing them into different groups depending on the material nature: organic, inorganic and eutectic PCMs. The ideal PCM should meet a number of criteria related to the desired thermophysical, kinetic and chemical properties summarized in Table 1.2 [83].

The application of PCMs with a solid-gas or liquid-gas phase transition is limited in thermal storage systems because of the large volume changes associated with the transition-even if they possess a high phase transition latent heat [1]. Solid-solid and solid-liquid transformations have a significantly smaller volume change, which makes PCMs economically and practically attractive as materials for thermal storage systems. Compared with solid-liquid transformations, solid-solid transformations are typically slow and have a rather low heat of fusion. Hydrates are considered one of the most promising phase change materials for cold storage in air-conditioning systems due to the appropriate phase change temperature range (4-20 °C) and large heat of fusion (270-430 kJ kg^{-1})[118]. Compared with ice cold storage systems, hydrate systems can improve the refrigeration efficiency greatly with the hydrate slurries as circulation media rather than antifreeze coolants or brines as illustrated in Fig. 1.4. With the larger heat of fusion than ice or eutectic salt, the hydrate can also decrease the volume of the cold storage tank and the cost for the initial investment [118]. Table 1.3 gives a summary of the performance of different cold storage media. It indicates that in comparison with the system which makes use of water as cold medium, the system which makes use of clathrate hydrate slurry has a higher COP with night mode generation and also a superior heat transfer performance.

Table 1.2: Criteria to select cold storage media [96].

Thermal properties	Melting temperature in the desired operating range; High phase transition latent heat per unit volume; High specific heat to provide significant additional sensible heat; High thermal conductivity of both phases;
Physical properties	Small volume change on phase transformation; Low vapour pressure at the operating temperature; Favourable phase equilibrium; Congruent melting of the PCM; High density to reduce the volume of storage tank;
Kinetic properties	No supercooling; High nucleation; Adequate rate of crystallization;
Chemical properties	Long term chemical stability; Completely reversible freeze/melt cycle; No corrosion influence of the construction materials; Non-toxic, non-flammable and non-explosive to ensure safety;

In this thesis, two different kinds of hydrate slurry (TBAB hydrate slurry and CO_2 hydrate slurry) are investigated to illustrate the advantage of hydrate slurry when applied for air conditioning systems. This work includes both experimental and model investigations. A coil heat exchanger and a fluidized bed heat exchanger are used to produce hydrate slurry. In this first part, a brief introduction of hydrate slurry will be given in section 1.3. Different designs of generators for hydrate production are also presented in this chapter.

1.3. FUNDAMENTALS OF HYDRATE SLURRY

Hydrate slurry is a mixture of hydrate crystals and water. If the crystals concentration is lower than a certain value, the hydrate slurry is pumpable, and can be applied as a secondary refrigerant in air-conditioning systems. The hydrate structures are introduced in this section as well as an overview of hydrate formation kinetics, including nucleation and growth.

Clathrate hydrates (or gas hydrates) are crystalline water-based solids physically resembling ice, in which small guest molecules, such as methane, ethane, propane, carbon dioxide, and hydrogen-sulfides, are trapped inside cages of hydrogen bonded, frozen water molecules. Most low molecular weight gases will form hydrates at suitable temperatures and pressures. Eq. 1.3 reflects the formation process of hydrate. In this equation, B stands for the guest molecules trapped in the cages. The reaction mostly occurs under low temperature and

Table 1.3: Performance and economical features of different cold storage media.

Cold storage medium	water	ice	Eutectic salt	Clathrate hydrates day/night
Phase change temperature (°C)	-	0	8-12	5-12
Evaporating temperature (°C)	2	-10	-4	5
Condensation temperature ((°C))	40	40	40	40/35
COP of primary cycle	5.88	4.03	4.82	6.54/7.89
Heat transfer performance	Superior	Medium	Inferior	Superior
Investment (In comparison with Ice)	< 0.6	1	1.3-2	1.2-1.5

high pressure conditions.

$$B + N\mathrm{H_2O} \rightleftarrows B \cdot N\mathrm{H_2O} \tag{1.3}$$

Clathrates were firstly discovered by Joseph Priestley (1778), but first documented by Sir Humphrey Davy (1811) in the Bakerian lecture to Royal Society in 1810.

Most of the structures known nowadays were synthesized in the nineteenth century. There are mainly three crystallographic structures of hydrates: sI, sII and sH, which differ by the cavity size and shape shown in Table 1.4. Definitive x-ray diffraction data on structure I was obtained by McMullan and Jeffrey (1965) [70], indicating the number of cavities in structure I shown in Table 1.4. In addition, structure I is formed with guest molecules having diameters between 4.2 and 6 $\overset{\circ}{A}$, such as methane, ethane, carbon dioxide and hydrogen sulfide [102]. Mak and McMullan (1965) [68] have undertaken a definitive x-ray diffraction study of structure II hydrate crystals, illustrating how a crystal may be completely defined by the cavities. Nitrogen and small molecules including hydrogen (d < 4.2 $\overset{\circ}{A}$) form structure II as single guests. Larger (6 $\overset{\circ}{A}$ <d <7 $\overset{\circ}{A}$) single guest molecules such as propane or isobutane will form structure II. Still larger molecules (typically 7$\overset{\circ}{A}$<d < 9$\overset{\circ}{A}$) such as iso-pentane or neohexane can form structure H when accompanied by smaller molecules such as methane, hydrogen sulfide or nitrogen [102]. The early studies focused on the identification of the molecules forming hydrates, and their formation conditions. Later on in 1930, hydrocarbon clathrate hydrates invoked considerable amount of applied research. In this occasion, the studies were the consequence of a major problem faced by the oil and gas industry, the plugging of transportation pipelines by gas hydrates. Investigations on hydrate formation thermodynamics followed, in addition, thermodynamic inhibitors and promoters were identified.

Table 1.4: Geometry of cavities that assemble the three hydrate crystal structures.

Hydrate crystal structure	I		II		H		
Cavity Description	small 5^{12}	large $5^{12}\,6^{2}$	small 5^{12}	large $5^{12}\,6^{4}$	small 5^{12}	medium $4^{3}\,5^{6}\,6^{3}$	large $5^{12}\,6^{8}$
Number of cavities	2	6	16	8	3	2	1
Number of water molecules	20	24	20	28	20	20	36

*Data taken from [102]

In middle 60's, the first natural gas hydrate deposits were identified, which triggered the interest on the kinetics of clathrate hydrates. Clathrate hydrates have been found to occur naturally in large quantities. Around 6.4 trillion (6.4 × 10^{12}) tonnes of methane are trapped in deposits of methane clathrate on the deep ocean floor. Such deposits can be found on the Norwegian continental shelf in the northern headwall flank of the Storage Slide. Clathrates can also exist as permafrost, as at the Mallik gas hydrate site in the Mackenzie Delta of northwestern Canadian Arctic. These natural gas hydrates are seen as a potentially vast energy resource, but an economical extraction method has so far not been identified. (https://en.wikipedia.org/wiki/Clathrate hydrate)

Hydrate slurries recently have been found to be good candidates for secondary refrigerants in air conditioning systems to operate as cold storage medium and distribution. Thermal properties of hydrates are important factors for the application of hydrates slurry on cold energy storage. The thermal conductivity of solid hydrate is mostly in the range of 0.5-0.8 W m $^{-1}$ K^{-1}, which more closely resembles that of liquid water (0.605 W m $^{-1}$ K^{-1}). Other properties, like latent heat, are quite different from the guest molecules that are trapped inside the cage of hydrate.

Hydrate formation is a stochastic phase change considered a crystallization process, which requires a supersaturated environment to take place [111]. Usually the crystallization can be divided into two consecutive processes: nucleation and growth. In the nucleation process, small clusters of water and gas or other guest molecules, which are known as hydrate nuclei, emerge and grow until they reach a critical size (around 25-170 Å). The formation of hydrate nuclei usually occurs at the interface of fluid-solid, gas-liquid or liquid-liquid, not only due to the higher concentration of water and guest molecules but also because the interface lowers the Gibbs' free energy of nucleation. The main driving force of hydrate nucleation is the chemical potential difference (converted to the temperature difference in this thesis) between the initial phase and the new phase. The magnitude of the driving force depends on the temperature, pressure and concentration difference between the operating and equilibrium conditions [111]. For the second process of hydrate growth, the stable hydrate nuclei grow to solid hydrates. During this period a significant amount of hydrate forms by incorporating large amounts of gas or other guest molecules, therefore, mass and heat transfer play a great role in this process.

1.4. GENERATION METHODS OF SLURRY

Generation of slurry has been widely investigated because it represents an essential part for the application of slurries as secondary cooling fluids. Tube exchangers are the most general generators for hydrate slurry as they are easy to build and the investment is low. However, the production of hydrate slurry in tube exchangers is difficult to control and the blockage of tubes may occur, restricting the use of this economical generator. Fig. 1.5 gives a representation of supersaturation of hydrate formation in generators without agitation. It shows that if a fluid is cooled down slowly without agitation it is possible to supersaturate the solution. In Fig. 1.5 the solid line stands for the solubility curve, while the dashed line is the metastable limit of solubility. On point 'a', the solution is under saturated and all the crystals will dissolve. On point 'b', there is an equilibrium between hydrates and solution. On point 'c', the solution is supersaturated. On point 'd', where there is a metastable limit, spontaneous nucleation can occur. The difference in temperature between point 'd' and 'f' is the supersaturation temperature difference.

Apart from tube generators, there are mainly three kinds of hydrate generators which have been discussed, for instance, by Pronk (2006) [84], including: 1) Scraped surface generator - the scraper inside the tube promotes the heat transfer performance of the exchanger, while the tight contact of the plastic scraper blade on the tube wall causes strong friction [129]. After a certain time interval of utilization the blades need to be replaced. The initial investment and the energy consumption are high. 2) Orbital rod generator: it's proven that the overall heat transfer coefficient of the orbital rod ice slurry generator is higher. The whip rod is metallic and has no direct contact with the tube, therefore it survives longer time than that of the plastic scraper blade [129]. However, the drive mechanism of whip rods is complicated and there are many associated problems [129]. 3) Fluidized bed generator -The research of the application of fluidized bed heat exchangers dates back to the early 1970s. It was first proposed for slurry pro-

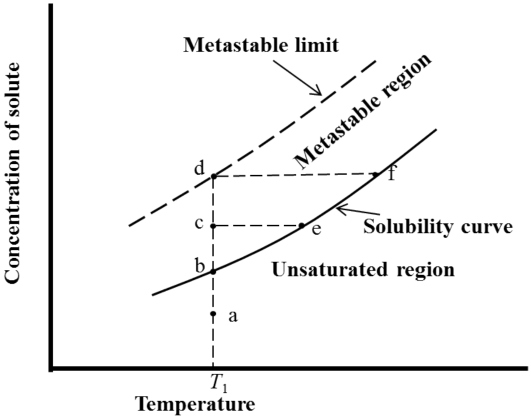

Figure 1.5: Graphical representation of supersaturation (Adapted from [94]).

duction in the early 1990s (Klaren and van der Meer, 1991 [53]). The principle of stationary fluidized bed heat exchangers is based on the movement of inert particles inside a tube which remove away the deposits from the walls. This disturbs the thermal boundary layer and therefore increases the heat and mass transfer coefficients. In addition, periodical cleanings are not necessary for this type of heat exchangers. According to these advantages, fluidized bed heat exchangers have been used in several fields. Ramon et al. (2013) [86] used a fluidized bed to produce research catalysts and found that the stability of the catalysts was higher than when conventional generation methods would be used. This because the fluidized bed reactor behaved better in removing deposits from their surface. Raj et al. (2013) [85] optimized the process parameters of a fluidized bed reactor which was used to transform waste tyres to liquid and gaseous fuel. Klaren and van der Meer (1991) [53] applied a fluidized bed as a chiller to make slush ice. Pronk (2006) [84] generated ice slurry using fluidized bed heat exchangers and proved that fluidized bed heat exchangers can prevent crystal fouling under certain operating conditions. The fluidized bed heat exchanger is expected to reduce investment costs considerably while increasing the heat transfer performance. Also stable operation over longer periods is expected, as well as benefits from large scale operations.

Plate heat exchangers (PHE) have also proved to be suitable for the production of some kinds of hydrate slurry. The operational conditions are limited to 20 bar and 150 °C [2], indicating no limitation for the application investigated in this study. The main advantages of PHE includes excellent heat transfer characteristics, large surface area in a small volume and can be modified for different requirements simply by increasing or decreasing the number of plates needed. For instance, Ma and Zhang (2011) [64] have produced TBAB hydrate slurry making use of a plate heat exchanger.

1.5. RESEARCH OBJECTIVES

The use of small primary refrigerant loops in combination with secondary loop distribution of cold is considered a solution to overcome the problems associated with the use of toxic, flammable and even high global warming potential refrigerants. Applying secondary-loop distribution systems, environmental-friendly working fluids can be employed to store low temperature energy and to distribute it to the different application sites. In this way the amount of primary refrigerant charged to the system is significantly reduced in comparison to the conventional distributed direct expansion systems resulting in much smaller leakage risk. Also the primary refrigerant can be maintained in restricted spaces, again limiting the risk to the environment. Low temperature energy storage can be easily included in secondary-loop refrigeration and air-conditioning systems and is an effective method to shift peak electric load to off-peak time as part of the strategy for energy management in buildings. It also contributes to a reduction of installed power and allows for night time operation when lower heat rejection temperatures are available for the primary refrigeration cycle. Hydrate slurry has been reported to be a good candidate secondary fluid due to its high latent heat and high phase change temperature.

The main objective of this work is to confirm the advantages of applying hydrate slurry as secondary fluid in air-conditioning systems. Due to the high latent heat and high phase change temperatures of hydrate slurries, the evaporation temperature can be increased. The condensing temperature can be lowered when the generation of hydrate slurry is moved to the night. In this case, the energy efficiency of space cooling can be substantially improved, as illustrated in Fig. 1.6. It indicates that if the evaporating temperature increases from 2 °C to 5 °C, the COP increases 11.2%; if the condensing temperature is then decreased from 40 °C to 35 °C, the COP increases significantly from 6.54 to 7.89.

A second objective of this thesis is to compare the performance of two different types of hydrate slurry: TBAB hydrate slurry and CO_2 hydrate slurry, when applied in air-conditioning systems. The production of TBAB hydrate slurry and CO_2 hydrate slurry are both investigated experimentally and numerically. New correlations are developed for further understanding of the heat transfer characteristics of hydrate slurry and the hydrate growth process.

A third objective of this research is to study the thermodynamic and kinetic influence of a hydrate formation limiter in order to produce hydrate slurry continuously while keeping the investment low. The inhibitor introduced in this work has been reported to be more efficient than other inhibitors and is envi-

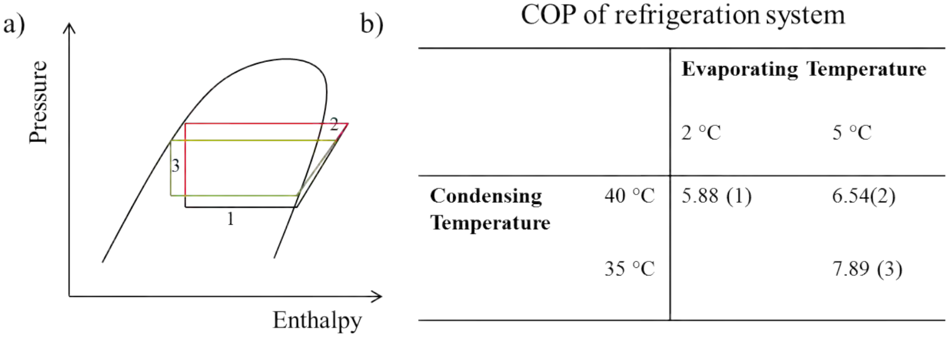

COP of refrigeration system

		Evaporating Temperature	
		2 °C	5 °C
Condensing Temperature	40 °C	5.88 (1)	6.54(2)
	35 °C		7.89 (3)

Figure 1.6: Impacts of operating conditions: evaporation and condensing temperature, on the performance of coefficient (COP) in refrigeration systems. a) refrigeration cycles in $P-h$ diagram; b) COP of refrigeration system under different conditions.

ronmental friendly. The growth mechanisms of CO_2 hydrate with the addition of the hydrate formation limiter have been investigated.

1.6. SCOPE AND OUTLINE OF THE THESIS

The overall aim of this thesis is to identify the advantages of applying hydrate slurries in air-conditioning systems. The flow behavior and production of hydrate slurries are both investigated experimentally and numerically. The hydrate growth models are developed for two kinds of hydrate slurries which are produced in different hydrate generators. The application of hydrate slurries has been investigated in a real slurry air conditioning system installation.

Chapter 2 studies the formation of TBAB hydrate slurries in a coil heat exchanger. In this chapter, the flow behavior of TBAB CHS has been investigated with solid concentrations up to 40 wt%. This concentration corresponds to a large latent heat of the slurry and so gives advantages when applied in air conditioning systems. The formation of a crystal layer on the tube wall is discussed in this chapter, as it has great influence on the pressure drop and heat transfer performance between slurries and refrigerant. A heat transfer correlation is developed to predict the heat transfer characteristics during the crystallization process of hydrates.

Chapter 3 studies the application of TBAB hydrate slurries for the air conditioning system of a small space. A plate heat exchanger is utilized for the production of TBAB hydrate slurries in order to meet the heat transfer area requirement. TBAB hydrate slurry behaves as a secondary-loop fluid which stores and distributes cold energy. The performance of this system is compared with the performance of a conventional air-conditioning system in which water is applied as the cooling medium.

Chapter 4 studies the production of CO_2 hydrate slurries in a Fluidized Bed heat exchanger as this type of generator is reported to be suitable for continuous production of (ice) slurries. A crystal growth model is developed to describe the CO_2 hydrate growth rate on the wall of the fluidized bed heat exchanger. The combination of this hydrate generator with a latent heat thermal storage system applied to an air-conditioning system for a specific office building is introduced to quantify the improvement of energy efficiency.

The fluidized bed heat exchanger used in Chapter 4 requires a large investment, in order to use the simpler generator mentioned in Chapters 2 and 3, the utilization of a hydrate formation limiter to slow down the CO_2 hydrate formation rate in the coil heat exchanger is investigated in Chapter 5. A general crystal growth equation is applied to identify the influence of the additive on CO_2 hydrate formation.

Finally, Chapter 6 summarizes the conclusions from the different chapters and some recommendations are present.

II

TBAB HYDRATE SLURRY

2

TBAB HYDRATE SLURRY PRODUCTION IN A COIL HEAT EXCHANGER

The selection of PCMs is extremely important for the application as secondary coolant as discussed in Chapter 1. TBAB hydrate slurry is discussed in this chapter. A coil generator is utilized for the production of TBAB hydrate slurry. The flow and heat transfer performance of TBAB hydrate slurry are investigated for the purpose of further application in refrigeration and air-conditioning systems.

Parts of this chapter have been published in the International Journal of Refrigeration, **64**, 130-142 (2016) [135].

2.1. INTRODUCTION

Air conditioning systems are generally operated making use of chilled water that is heated from 7 to 12 °C with evaporation temperature just above zero °C. The evaporation temperature can be increased as discussed in Chapter 1. Hydrate slurries have been discussed in Chapter 1 to be good candidates phase change materials (PCM) for air-conditioning systems. An aqueous solution of 36.5% tetra-n-butyl ammonium bromide (TBAB) undergoes a liquid/solid phase change at 12 °C. In this way aqueous TBAB hydrate slurries, which allow for evaporating temperatures of +5 °C or even higher, are very promising secondary-loop working fluids. They allow for latent low temperature heat storage at temperatures close to the application temperature (and so for reduced energy consumption), can operate at atmospheric pressure and require reduced storage and distribution line sizes.

TBAB is a quaternary salt that crystallizes in small solid particles, called hydrates, at operating conditions suitable for air conditioning applications (atmospheric pressure and temperatures in the range of 0-12 °C). TBAB hydrate slurry is a phase change material which is pumpable and can be used for cold storage purposes. The utilization of TBAB hydrate slurry as cold storage medium can save energy and significantly reduce the peak electricity demand of air conditioning systems in the day time especially during summer time. TBAB can form two types of hydrates with different hydration numbers. Type A has a columnar shape (Shimada et al., 2005 [100]) and a latent heat of 193 kJ kg^{-1}, while type B has an irregular form of thin crystals and has a latent heat of 200 kJ kg^{-1} (Oyama et al., 2005 [81]). The phase diagram for aqueous TBAB solutions presented by Ma et al. (2010) [67] is reproduced in Fig. 2.1. It shows that, at 36.5 wt% initial aqueous solution concentration, the phase change temperature of type A TBAB hydrate is 12.5 °C. Notice that type B hydrate forms only at a 3-4 °C lower temperature. In this study an initial aqueous solution concentration of 36.5 wt% has been selected so that type A TBAB hydrate crystals start forming at around 12.5 °C. As already mentioned above, this temperature is closer to the application temperature so that higher energetic efficiency can be attained in the primary refrigerant loop.

The fluid flow and heat transfer characteristics of aqueous TBAB hydrate slurries in pipe and heat exchangers are required in order to make its wide use possible. In the past years the Institute of Refrigeration and Cryogenics of the Shanghai Jiao Tong University has intensively studied several aspects related to the utilization of aqueous TBAB hydrate slurries. One of the advantages of aqueous TBAB hydrate slurry systems is that the crystals can be generated continuously in heat exchangers of common design and so this heat exchanger does not significantly increase the costs of the secondary-loop system. Shi and Zhang (2013)

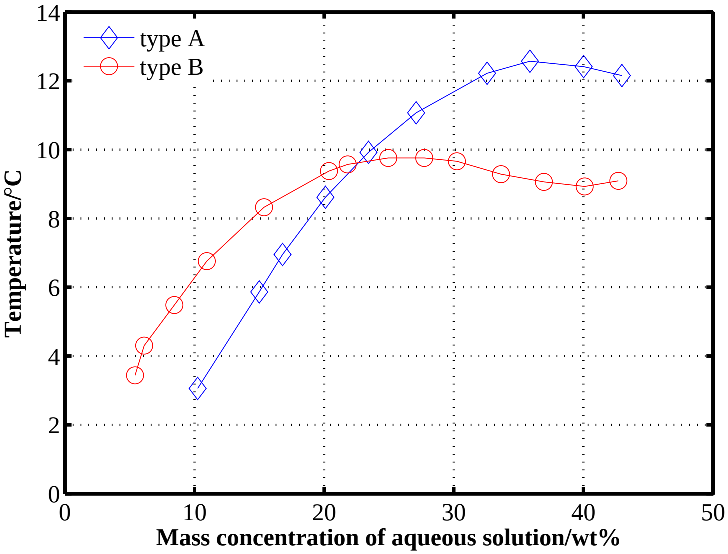

Figure 2.1: T-w diagram of the liquid-solid phase equilibrium of the two types of TBAB hydrate (Data taken from [67]).

[98] have studied four hydrate slurry generation methods and have concluded that continuous cooling causes adhesion of crystals to the surface of the heat exchanger. In their set-up the surface temperature of the heat exchanger was very low (ca.4 °C). The adhered crystal layer formed a thermal resistance layer which increased with time and significantly deteriorated the heat transfer between refrigerant and TBAB. They reversed discontinuously the primary refrigeration cycle to allow for melting of the crystals so that longer operating times were possible. Shi and Zhang (2014) [99] compared experimentally the overall heat transfer coefficients before crystallization and during crystallization. They found that more hydrate crystals adhere to the wall at larger degree of supercooling and higher mass concentration of TBAB in the aqueous solution, deteriorating the heat transfer significantly. In the present study the wall temperature and so the driving force for the formation of crystals is controlled by submerging the heat exchanger in a thermostatic bath and accurately controlling its temperature. Also the concentration of crystals in the solution can be maintained by adjusting the system load making use of a second thermostatic bath. This paper presents data collected under such a setting and the results are compared to previous studies. Ma and Zhang (2013a,b) [65] [66] have experimentally investigated the flow and heat transfer characteristics of TBAB hydrate slurry during its generation in a double-tube heat exchanger and have determined the crys-

tal layer growth on the wall as a function of time. The crystal layer caused the enlargement of pressure drop and the drastic reduction of heat transfer performance due to the narrowing flow passage and large thermal resistance, respectively. Ma et al. (2010) [67] also proposed empirical heat transfer correlations for TBAB hydrate slurries. Ma and Zhang (2011)[64] proposed flow friction factor and heat transfer correlations for TBAB hydrate slurries flowing through plate heat exchangers. Kumano et al. (2011a) [55] investigated the heat transfer characteristics of a TBAB hydrate slurry where the Reynolds number, tube diameters and solid fraction were varied as experimental parameters. For laminar flow, it was found that the ratio of Nusselt numbers increased with solid fraction. An approximation of Nusselt number could be derived using the Graetz number on the basis of the apparent Reynolds number (Re_M), the solid fraction and the ratio of the average diameter of the hydrate particles to the test tube diameter. For turbulent flow conditions, the ratio of Nusselt numbers had a value of one for each condition at low solid fractions. The ratio of Nusselt numbers increased with solid fraction in the high solid fraction region. Moreover, the apparent Reynolds number, which can be derived by treating the hydrate slurry as a pseudoplastic fluid, can be used to determine the condition under which hydrate slurry heat transfer characteristics vary under turbulent flow. Zhang and Ye (2014)[132] developed heat transfer correlations for flow melting of TBAB hydrate slurries in mini-tubes with diameters of 2.0 mm and 4.5 mm on the basis of the experimental data.

Kumano et al. (2012) [54] have concluded that, for the high solid fraction region, a laminarization phenomenon occurs and the flow and heat transfer characteristics can be estimated from the laminar flow of the hydrate slurry. The laminarization point depending on the solid fraction could be predicted using the modified Reynolds number, Re_M. Kumano et al. (2011b)[56] proposed that the flow characteristics of the hydrate slurry can be treated as those of a pseudoplastic fluid and clarified this by using the modified Reynolds number. Song et al. (2009a)[104] studied the heat transfer characteristics of TBAB slurry in a horizontal stainless steel tube using different solid mass fractions and flow velocities with constant heat flux. These authors considered the slurry to behave as a Bingham fluid and derived a heat transfer correlation for laminar and turbulent flows in the form of a power function. Ma et al. (2010) [67] studied the forced flow and convective melting heat transfer characteristics of TBAB hydrate slurry flowing through straight circular tubes and found that an empirical correlation, based on the modified Reynolds number, could be used to predict the flow friction factor of TBAB. In the present study all experiments are conducted under laminar flow conditions.

Helical coil heat exchangers are used in many applications including refrigeration industry and HVAC applications. This type of heat exchangers has a higher heat transfer rate than straight tubes, allowing for a more compact structure. The flow regime is different due to the centrifugal forces that are involved. The heat transfer enhancement of helical coils has been reported by Akiyama and Cheng (1971) [5], Futagami and Aoyama (1988) [36], Janssen and Hoogendoorn (1978) [46] and Kalb and Seader (1972) [49]. Several numerical studies of helically coiled heat exchangers have been presented indicating similar advantages (Ferng et al. 2012 [33]; Jayakumara et al., 2008 [47]).

Most of the studies on heat transfer and flow characteristics of TBAB hydrate slurry in heat exchangers deal with single tube experiments (Song et al., 2009b [105]; Ma et al., 2010[67]; Kumano et al., 2011a-b[55] [56]). Knowledge on the flow and heat transfer characteristics of TBAB hydrate slurry in a helical coil heat exchanger is of significant importance and necessary for practical applications. The fluid flow and heat transfer characteristics of TBAB hydrate slurry are complex due to the non-Newtonian behaviour at high slurry concentrations and the phase change process. The formation of TBAB hydrate crystals in helical heat exchangers needs further investigation.

The objective of this chapter is to investigate the pressure drop and heat transfer characteristics of a coil heat exchanger during the formation of TBAB hydrate crystals. Experiments were carried out using a coil heat exchanger with 114 mm coil inner diameter, a total length of 4.5 m and 5.6 mm internal tube diameter. Pressure drop and heat transfer coefficients were obtained for water, TBAB aqueous solution and TBAB hydrate slurry with different solid mass fractions. Where possible these data are compared to previously published experimental data and correlations for TBAB solution.

2.2. EXPERIMENTAL METHOD

2.2.1. SYSTEM DESCRIPTION

TBAB solution (CAS No. 1643-19-2) in water with 50% concentration was purchased from Sigma - Aldrich and it has been used to prepare a TBAB solution with 36.5 wt% concentration. For this concentration only TBAB hydrate type A forms at equilibrium temperature of ca. 12.5 °C.

After the system has been brought to vacuum, the solution has been filled in the experimental system. The experimental set-up represents a secondary cooling loop which has the role of production, storage and transport of hydrate slurries.

Fig. 2.2 shows the schematic diagram of the experimental set-up. The PID digram is reproduced in Appendix A. The system consists of two thermostatic baths and two coil heat exchangers, a gear pump and two buffer vessels (not shown). In each thermostatic bath, the coil heat exchanger consists of two small coils connected in series which have been designed to fit in the thermostatic baths.

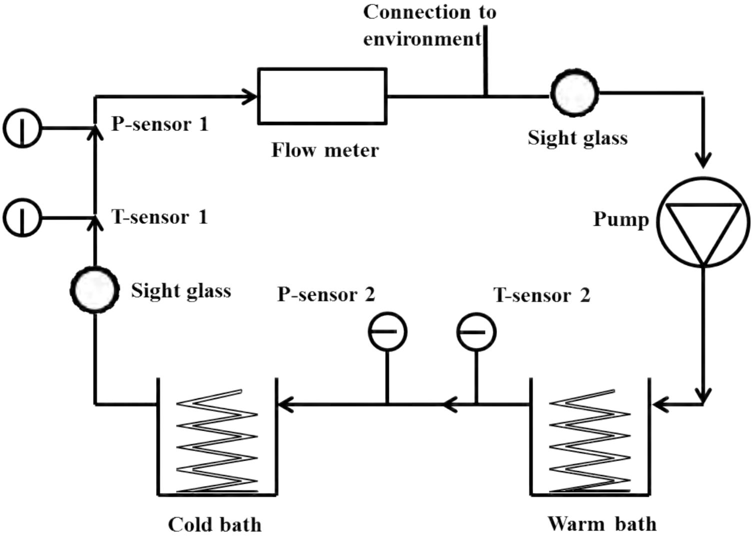

Figure 2.2: Schematic diagram of the experimental set –up including two thermostatic baths, two pressure sensors, two temperature sensors, a gear pump, a flowmeter, two sight glasses and two storage vessels (not shown).

The solution is cooled in the coil heat exchangers using thermostatic baths filled with water. The effective cooling capacity of each bath is 0.3 kW. Sight glasses in stainless steel are used to visualize the flow. The flow is circulated with a Gather gear pump (0.37 kW) with adjustable speed. Using an inverter, the flow rate is varied between 50 and 110 kg h^{-1} by controlling the frequency applied to the gear pump. The warm thermostatic bath is kept at slightly higher temperature (0.5 -1.0 K) than the cold one allowing for partial melting. In this way the condition of the inlet of the cold heat exchanger can be maintained for a long time. Temperature of the fluids is measured at the inlet and outlet of the coil heat exchanger located in the cold bath by PT100 temperature sensors (accuracy ± 0.03 K). Two pressure sensors (Siemens Sitrans P DS III, accuracy ± 2 kPa) are located before and after the coil heat exchanger in the cold thermostatic bath to measure the pressure drop. The density is measured with a Coriolis mass flow meter (Endress+Hauser ProlinePromass 80A, accuracy ± 0.5 kg m^{-3} and ± 0.15% of the measured flow). Temperatures, pressures and density are stored every 5 seconds by a data logger (ATAL, ATM –06D).

Fig. 2.3 shows the schematic of the helical coil heat exchanger that is immersed in a thermostatic bath. The TBAB solution flows within the tube and is cooled by the chilled water within the thermostatic bath. The pipe has an inner diameter of 5.6 mm. The coil has a diameter of 120 mm (measured between the centers of the pipes). The distance between two adjacent turns, called pitch, is 8 mm. Ratio of pipe diameter to coil diameter is called the curvature ratio. The coiled tube has 12 turns in total. The curvature of the coil governs the centrifugal force while the pitch influences the torsion force.

The overall heat transfer coefficient is calculated based on the measured temperatures and flow rates as shown in Eq. 2.1.

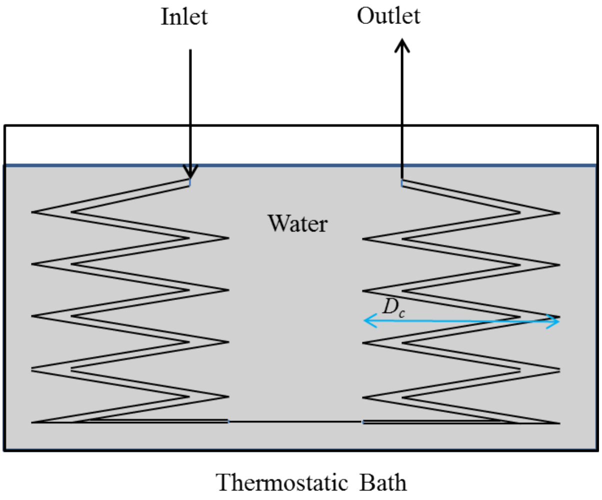

Figure 2.3: Configuration of the helical coils in the thermostatic baths which are filled with water. The coil diameter, D_c, is 120 mm with an internal tube diameter of 5.6 mm. The pitch, which is the distance between two adjacent turns, is 8 mm. There are 12 turns giving a total length of the coil 4.74 m.

$$U = \frac{\dot{m}\Delta h - \dot{m}\frac{\Delta P}{\rho_s} - \dot{Q}_{\text{loss}}}{A_i \Delta T_{\text{log}}} \tag{2.1}$$

where ΔT_{log} is defined by the following expression Eq. (2.2)

$$\Delta T_{\text{log}} = \frac{(T_{\text{in}} - T_{\text{bath}}) - (T_{\text{out}} - T_{\text{bath}})}{\ln \frac{T_{\text{in}} - T_{\text{bath}}}{T_{\text{out}} - T_{\text{bath}}}} \tag{2.2}$$

The enthalpy change of the TBAB hydrate slurry is given by Eq. (2.3)

$$\Delta h = c_{ps}(T_{\text{out}} - T_{\text{in}}) + h_{\text{lat}}(w_{\text{out}} - w_{\text{in}}) \tag{2.3}$$

The energy loss $\dot{Q}_{\text{loss}}$ in Eq. (2.1) has been estimated to be equal to 3 W by taking the length of the tube and its insulation thickness into account. The second term in Eq. (2.1) relates to the heat released by friction losses.

The outside heat transfer coefficient α_o is determined from the experimental data and calculated as given in Eq. (2.4).

$$\frac{1}{\alpha_o} = \frac{1}{U} - \frac{d_i \ln \frac{d_o}{d_i}}{2\lambda_w} - \frac{d_i}{\alpha_i d_o} \tag{2.4}$$

The thermal conductivity of the wall is 13 W m^{-1} K^{-1} for stainless steel.

2.2.2. TBAB HYDRATE GENERATION

TBAB hydrate slurry has been generated by super-cooling the solution, followed by nucleation and then growth of the crystals. A mixture of 36.5 wt% TBAB and water is cooled at temperatures from 20 °C to 11 °C in steps of 0.5 K per 10 minutes until the driving force is large enough and hydrates become visible in the sight glasses of the set-up. The temperatures at the inlet and outlet of the coil heat exchanger rise when hydrates appear. Fig. 2.4 presents a sample variation of the temperatures of the thermostatic baths and at the inlet and outlet of the coil heat exchanger during hydrate formation. The formation of hydrates is highlighted by the rise of temperature that is due to the exothermic phase change process. The formation starts at the temperature of 13 °C after around 5000 seconds. Immediately after the formation the temperatures of the thermostatic bath have been increased with 0.5 K per 15 minutes in order to control the quantity of solids. A steady operation of the system has been obtained for the thermostatic baths temperatures of 10 °C and 9.2 °C respectively, which gives an equilibrium temperature of slurry 14.2 °C.

Fig. 2.5 shows the pressure drop across the cold bath heat exchanger during the tests shown in Fig. 2.4. The pressure drop increases significantly when hydrate formation starts and reduces when stable operating conditions are attained. The pressure drop of the slurry flow (1.5 bar) is significantly larger than the pressure drop of the solution flow (0.5 bar).

2.2.3. EXPERIMENTAL ACCURACIES

The experimental uncertainties of slurry tests are summarized in Table 2.1. The uncertainties of the derived parameters depend on the solid fraction of TBAB hydrate slurry. The uncertainties are larger for low concentrations and smaller for high concentrations.

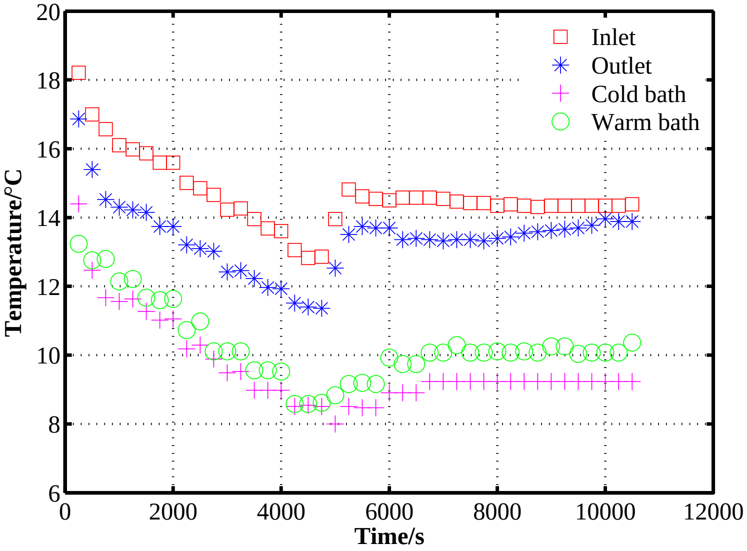

Figure 2.4: Temperature change of the two thermostatic baths and of the inlet and outlet of the solution during hydrate formation experiment.

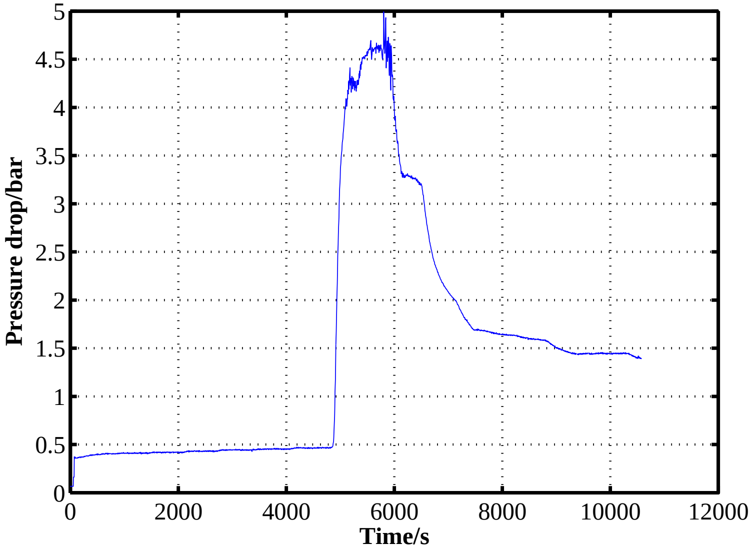

Figure 2.5: Typical example of the pressure drop variation across the hydrate slurry generator during TBAB hydrate formation experiment before a stable pressure drop is attained.

Table 2.1: Summary of experimental uncertainties.

Parameters	Uncertainty
Measured Parameters	
Temperature K	± 0.03
Pressure kPa	± 1
Density kg m^{-3}	± 0.5
Mass flow rate %	± 0.15
Derived parameters	High/low Concentration
Solid fraction w%	3.12-10.9
Reynolds Re%	± 0.15
Pressure drop ΔP%	± 0.8-2.8
Friction factor f%	0.9-2.7
Overall heat transfer coefficient U%	7.3-8.8

2.3. PROPERTIES OF TBAB HYDRATE SLURRY

The density of TBAB solution has been measured and the results are shown in Fig. 2.6. As expected, the density increased as the temperature of the solution decreased. The experimental values are compared with data presented by Ogoshi and Takao (2004) [78] and Zhang et al. (2012) [131]. The line marked by ◊ represents the values obtained by interpolating between the density of 30 wt% TBAB solution and the density of 40 wt% TBAB solution values presented by Ogoshi and Takao (2004)[78] . The solid line is predicted with the equation of Zhang et al. (2012) [131]. The measured density is slightly higher than both the data of Ogoshi and Takao (2004) [78] and Zhang et al. (2012) [131] by approximately 2.5 kg m^{-3}.

Solid mass fraction has been calculated based on the density measurements of hydrate slurry by Eq. (2.5).

$$w_H = \frac{1-\frac{\rho_s}{\rho_L}}{\frac{\rho_s}{\rho_H - \frac{\rho_s}{\rho_L}}} \tag{2.5}$$

in which, ρ_H is the density of hydrate type A. According to Ogoshi and Takao (2004) [78] ρ_H=1080 kg m^{-3} and ρ_L is the solution density measured at the operating temperature, for instance, ρ_L=1039.5 kg m^{-3}.

The thermal conductivity of TBAB hydrate slurry has been calculated with Maxwell's equation (Zhang et al., 2010 [130]), while the thermal conductivity of TBAB solution is derived from Ma et al. (2010) [67]. Table 2.2 summarizes the properties of TBAB hydrate crystals.

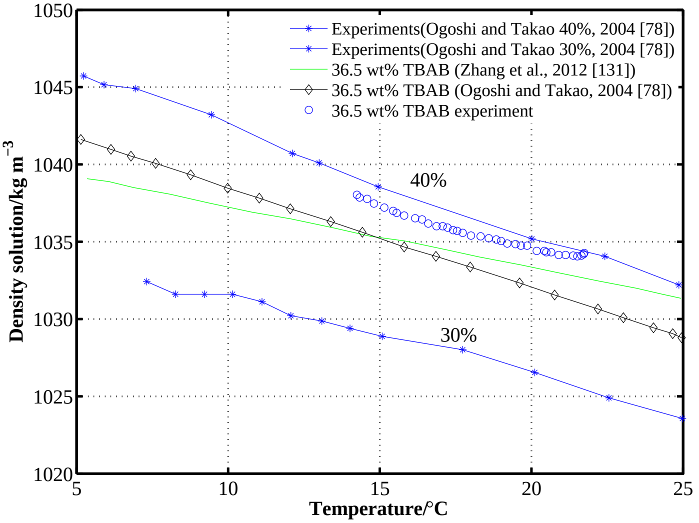

Figure 2.6: Comparison of the experimental density data of the TBAB solution with the data derived from literature sources.

The dynamic viscosity of 36.5 wt% TBAB solution at equilibrium condition (14.2 °C) is derived to be 0.00635 Pa· s from Kumano et al. (2011a) [55]. Viscosity is predicted with Eq. (2.6) which matches the equilibrium condition.

$$\mu_{\text{TBAB}} = exp(-0.684 \ln T - 3.242) \tag{2.6}$$

In which T is expressed in °C. The dynamic viscosity of hydrate slurry is calculated with the Thomas equation (Christensen and Kauffeld, 1997 [14]). The specific heat of slurry is obtained as Eq. (2.7).

$$c_{ps} = w c_{pH} + (1 - w) c_{pL} \tag{2.7}$$

in which c_{pH} is the specific heat of hydrate type A according to Ogoshi and Takao (2004) [78], and $c_{pL}$is the specific heat of the solution, which is taken from Asaoka et al. (2013) [9].

For water, the density, dynamic viscosity, specific heat and thermal conductivity have been calculated as a function of the average temperature and pressure between inlet and outlet of the heat exchanger using REFPROP (Lemmon et al., 2013 [59]).

Table 2.2: Thermophysical properties of TBAB hydrate crystals.

	Structure [55]	Hydration number	Melting temperature °C	Density [78] kg m^{-3}	Latent heat [81] kJ kg^{-1}	Specific heat kJ kg^{-1} K^{-1}	Thermal conductivity W m^{-1} K^{-1}
Type A	Needle like	26[78] [81]	11.8[78] / 12.0[81]	1080	193.18 ± 8.52	2.22[78]	0.42 [43]
Type B	complex	36[78]/38 [81]	9.9 [81]	1030	199.59 ±5.28	2.00-2.54 [81]	

2.4. RESULTS

2.4.1. FLOW CHARACTERISTICS

The flow phenomena in helically coiled tubes are more complex than in straight tubes due to centrifugal force effects. The transition from laminar to turbulent flow is shifted to higher Reynolds numbers (Gnielinski, 2010 [38]) as shown in Eq. (2.8).

$$\mathrm{Re}_{\mathrm{crit}} = 2300\left[1+8.6\left(\frac{d_i}{D_c}\right)^{0.45}\right] \tag{2.8}$$

For the experimental conditions, $\mathrm{Re}_{\mathrm{crit}} = 7280$, for all tests the flow is laminar. The flow in a helical coil pipe is characterized by the Dean number as Eq. (2.9).

$$\mathrm{De} = \mathrm{Re}\sqrt{\frac{d_i}{D_c}} \tag{2.9}$$

The Dean number for water is in the range 610 to 1400. For TBAB solution, the Dean number is between 110 and 240. The Dean number for TBAB hydrate slurry is between 20 and 200.

The pressure drop is calculated based on Darcy–Weisbach equation as Eq. (2.10).

$$\triangle P = \left(f_{\mathrm{str}}\frac{L_{\mathrm{str}}}{d_i} + f_c\frac{L_c}{d_i} + K\right)\frac{\rho u^2}{2} \tag{2.10}$$

In which, the friction factor is obtained with the Poiseuille relation (Eq. (2.11)) for laminar flow.

$$f_{\mathrm{str}} = \frac{64}{\mathrm{Re}} \tag{2.11}$$

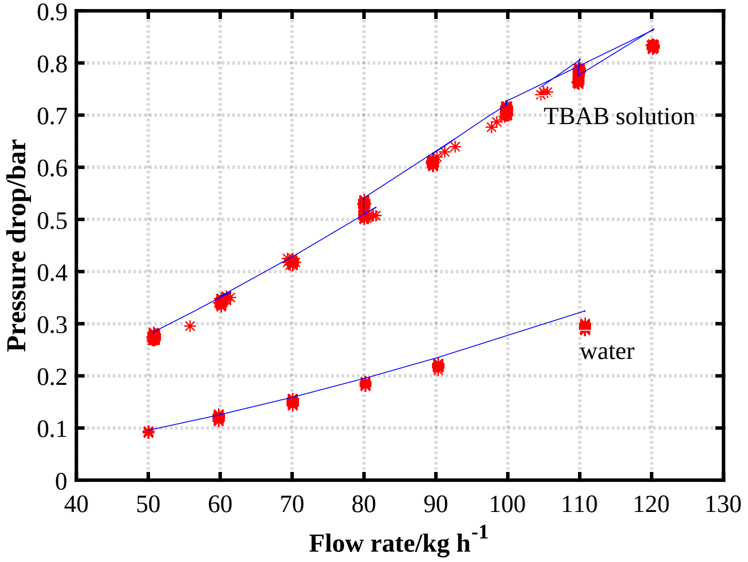

Figure 2.7: Experimental and predicted pressure drop of water and TBAB solution as a function of the flow rate.

Frictional factor for curved tubes in relation to the friction factor for straight tubes is obtained from Naphon and Wongwises (2006) [75] as Eq. (2.12).

$$\frac{f_c}{f_{\mathrm{str}}} = 1 + 0.015\mathrm{Re}^{0.75}\left(\frac{d_i}{D_c}\right)^{0.4} \tag{2.12}$$

K in Eq. (2.10) stands for the loss caused by the sharp corners in the tubes. It was taken to be 0.9 from Gnielinski (2010) [38] for one turn. There are totally 5 sharp corners in the test section.

Fig. 2.7 shows a comparison between predicted and experimental pressure drop of water and 36.5 wt% TBAB solution as a function of flow rate. The pressure drop of both water and TBAB solution can be predicted well with existing equations. The pressure drop of TBAB solution is about 2.6 –3.0 times larger than that of chilled water.

Fig. 2.8 shows the relationship between the friction factor and the Reynolds numbers for water, TBAB solution and TBAB hydrate slurry. The friction factor decreases with the increase of Reynolds number. Fig. 2.9 shows that pressure drop for slurry concentration higher than 40% can not be predicted by Eq. (2.10) when the general definition of Reynolds, *Re*, is applied. The figure illustrates that the assumption of Newtonian fluid for TBAB hydrate slurry can be applied up to solid concentrations of 40%. It also shows that the flow has a non-Newtonian

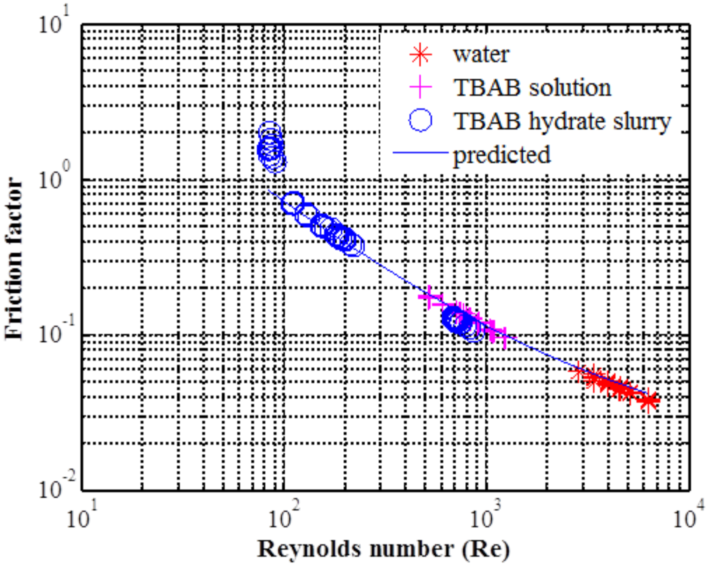

Figure 2.8: Comparison of the experimental and predicted friction factor of water, TBAB solution and TBAB hydrate slurry as a function of Reynolds number.

behavior for concentrations higher than 40%.

Fig. 2.10 presents a comparison between the predicted and experimental pressure drop of the hydrate slurry as a function of solid mass fraction for different flow velocities. The pressure drop increases with the solid fraction and flow velocity. In a previous study, the pressure drop of 15 wt% TBAB hydrate slurry melting in a double-tube heat exchanger has been estimated to be 1-1.4 times higher than that of the aqueous solution for the same flow velocity (Ma and Zhang, 2013a. [65]). In the present experiments the ratio is in the range of 1.15 –1.8, which is quite comparable but slightly higher. Fig. 2.10 also shows that for high concentration slurries, the fluid is non-Newtonian, and the pressure drop cannot be predicted by Eq. (2.10).

2.4.2. HEAT TRANSFER

Correlations proposed for coil heat exchangers are firstly reviewed. Dravid et al. (1971) [23] studied the laminar flow heat transfer in helically coiled tubes and proposed the following correlation as Eq. (2.13)

$$\mathrm{Nu} = (0.65\sqrt{\mathrm{De}} + 0.76)\mathrm{Pr}^{0.175} \tag{2.13}$$

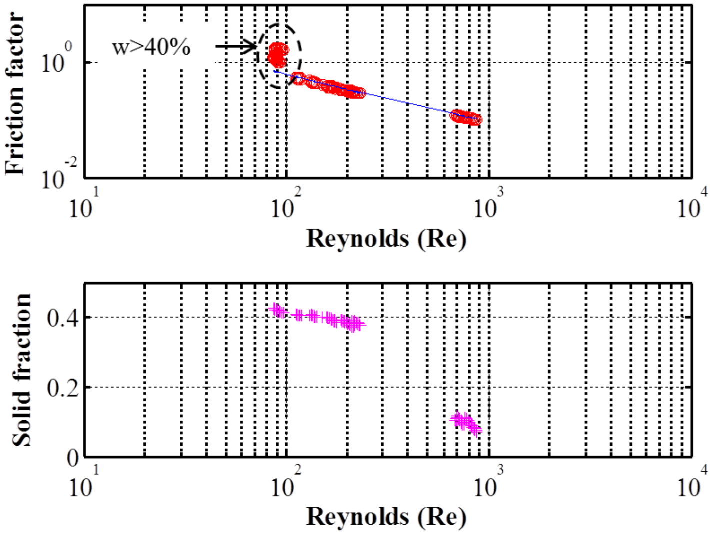

Figure 2.9: Comparison of the experimental friction factor change with solid fraction as a function of the Reynolds number.

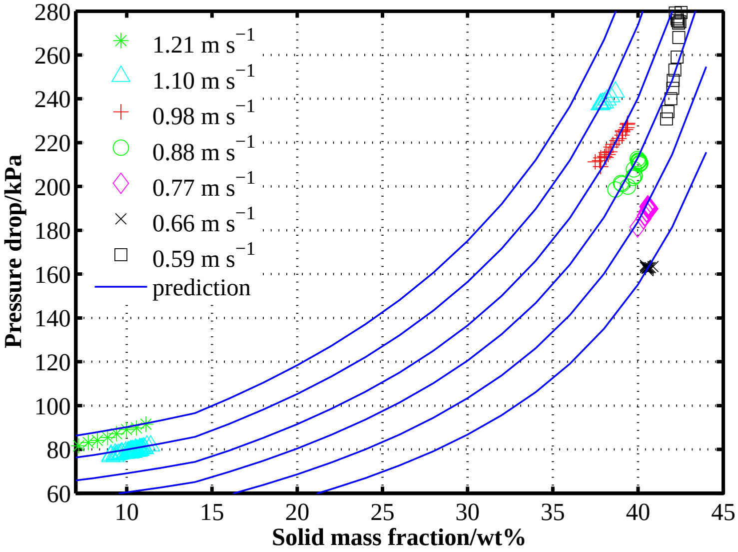

Figure 2.10: Comparison of the experimental and predicted pressure drop of TBAB hydrate slurry as a function of solid mass fraction at different flow velocities.

For $50 < \mathrm{De} < 200$ and $5 < \mathrm{Pr} < 175$. Xin and Ebadian (1997) [119] proposed the following equation for flow in helical pipes:

$$\mathrm{Nu} = (2.153 + 0.318\mathrm{De}^{0.643})\mathrm{Pr}^{0.177} \tag{2.14}$$

For $20 < \mathrm{De} < 2000$, $0.7 < \mathrm{Pr} < 175$, and $0.0267 < \dfrac{d}{D_c} < 0.0884$. Ma and Zhang (2013a) [65] proposed a correlation for single phase flow in a co-axial double tube heat exchanger:

$$\mathrm{Nu} = 0.12\mathrm{Re}^{0.75}\mathrm{Pr}^{1/3} \tag{2.15}$$

The Nusselt numbers proposed for coil heat exchangers were also compared with the prediction of the equation of Gnielinski (1976) [37] as Eq. (2.16). This equation predicts the single phase heat transfer coefficient in the Reynolds number range between 2300 to 10^4 under uniform heat flux conditions in tubes

$$\mathrm{Nu} = \frac{\frac{f}{8}(\mathrm{Re} - 8000)\mathrm{Pr}}{1 + 12.7\frac{f}{8}^{0.5}(\mathrm{Pr}^{2/3} - 1)} \tag{2.16}$$

where $f = (1.82\log_{10}\mathrm{Re} - 1.64)^{-2}$.

Heat transfer by natural convection outside of tubes is also investigated to allow for a comparison.

Ali (1994) [6] studied the convection from vertical coiled tubes and proposed a correlation for natural convection around these coils

$$\mathrm{Nu} = 0.016 \times \mathrm{Ra}_H^{0.433} \tag{2.17}$$

for $\frac{D_c}{d_o} = 19.957$ and $2 \times 10^8 \leq \mathrm{Ra}_H \leq 5 \times 10^{10}$.

Churchill and Chu(1974) [15] proposed a correlation for natural convection outside of a horizontal cylinder

$$\mathrm{Nu} = 0.36 + \frac{0.518 \times \mathrm{Ra}_H^{1/4}}{(1 + (0.559/\mathrm{Pr})^{9/16})^{4/9}} \tag{2.18}$$

Fig. 2.11 shows the comparison of the experimental α_o derived from Eqs. (2.13) to (2.16) for the experiments with water, with the predictions of Eqs. (2.17) and (2.18). It indicates that the correlations from Ali and Churchill and Chu under predict the experimental heat transfer coefficient in the thermostatic bath side compared with the data derived from Eqs. (2.13) to (2.16). Eq. (2.13) gives the highest heat flux dependency of α_o, however, the Dean number application range is out of the range of experimental data. Therefore, Xin and Ebadian's equation was selected to derive a heat transfer correlation for the thermostatic

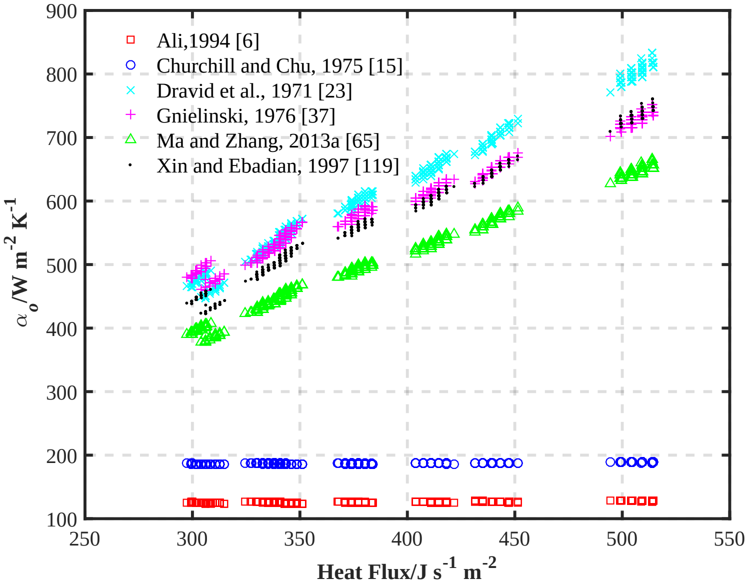

Figure 2.11: Comparison of the external heat transfer coefficient derived from literature with the experimentally derived value as a function of heat flux applied to the coil.

bath side as Eq. (2.19) as it shows the most similar result as what Dravid's equation gives. Eq. (2.15) shows the same trend as the prediction from Eqs. (2.13) and (2.14), but gives lower value. Eq. (2.16) does not take the coil curvature into account, nevertheless Gnielinski's equation gives similar results for lower heat flux.

$$\alpha_o = 1.4\dot{q} + 30.697 \tag{2.19}$$

Fig. 2.12 shows a comparison between experimental and calculated overall heat transfer coefficient for the TBAB solution experiments. It indicates a good prediction of the proposed heat transfer prediction approach. The obtained values of the overall heat transfer coefficient are higher than the values reported by Shi and Zhang (2014) [99].

2.4.3. HEAT TRANSFER DURING HYDRATE GENERATION AND MELTING

Ma et al. (2010) [67] derived a heat transfer correlation from their experiments with convective melting of TBAB hydrate slurry in a heated straight tube. Ma and Zhang (2013b) [66] applied this correlation also for the TBAB hydrate slurry generation process. This correlation is the only validated correlation for the pre-

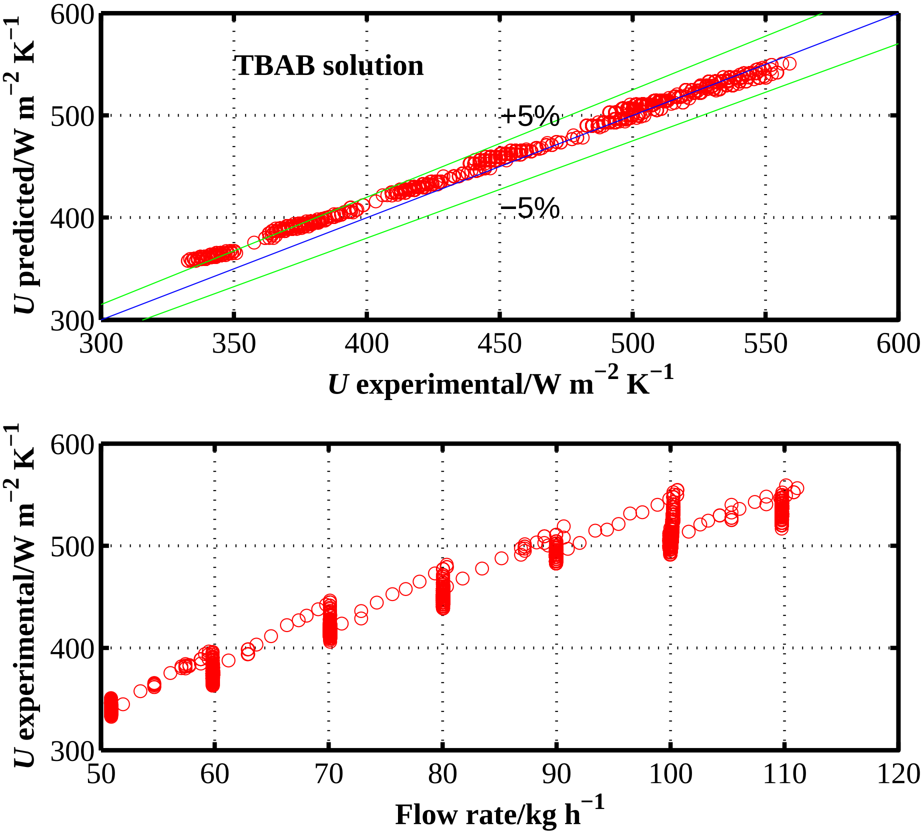

Figure 2.12: a) Comparison of experimental and predicted overall heat transfer coefficient for TBAB solution tests; b) The experimental overall heat transfer coefficient of TBAB solution as a function of flow rate.

diction of heat transfer during TBAB hydrate slurry generation. Ma et al. (2010) [67] consider two regions : Laminar flow, $700 < \mathrm{Re}_M < 1500$

$$\mathrm{Nu} = 0.2368(\mathrm{Re}_M\mathrm{Pr})^{0.5873}\mathrm{Ste}^{-0.0795}\left(\frac{d_i}{L_c}\right)^{0.2645}\left(\frac{d_p}{d_i}\right)^{-0.0182} \tag{2.20}$$

Transitional and turbulent flow, $1500 < \mathrm{Re}_M < 3500$

$$\mathrm{Nu} = 0.0219(\mathrm{Re}_M\mathrm{Pr})^{0.7093}\mathrm{Ste}^{-0.0498}\left(\frac{d_i}{L_c}\right)^{-0.2009}\left(\frac{d_p}{d_i}\right)^{-0.2441} \tag{2.21}$$

In these equations Re_M is the modified Reynolds number proposed by Metzner and Reed (1955) [72] as

$$\mathrm{Re}_M = \frac{\rho_S u^{2-n} d_i^n}{8^{n-1}K'} \tag{2.22}$$

with n and K' the flow behaviour index and fluid consistency coefficient, respectively. These coefficients have been quantified by Kumano et al. (2011a) [55]. These authors propose a value of 0.41 mm for d_p, the crystals average size in the TBAB hydrate slurry, for type A TBAB hydrate.

Additionally Ma and Zhang (2013a) [65] have proposed a correlation for the prediction of heat transfer during the hydrate melting process:

$$\mathrm{Nu} = 0.0598\mathrm{Re}_M^{0.711}\mathrm{Pr}^{1/3}\left(1 + \frac{\Delta w \Delta h}{c_p \Delta T}\right)^{0.457} \tag{2.23}$$

with Δw the solid concentration change in the control volume considered.

Also Kumano et al. (2011b) [56] have proposed a correlation for the prediction of heat transfer during the melting of TBAB hydrates:

$$\mathrm{Nu} = 3.33\left(\mathrm{Re}_M\mathrm{Pr}\frac{d_i}{L_c}\right)^{0.18} w^{0.42}\left(\frac{d_i}{d_p}\right)^{0.55} \tag{2.24}$$

Notice that this relation only applies when $0.03 \leqslant w \leqslant 0.18$.

Edwards et al. (1979) [27] proposed a correlation for the Nusselt number when Reynolds number is lower than 2300 in straight tubes

$$\mathrm{Nu}_{\mathrm{str}} = 3.66 + \frac{0.065\frac{d_i}{L_c}\mathrm{RePr}}{1 + 0.04(\frac{d_i}{L_c}RePr)^{2/3}} \tag{2.25}$$

Eq. (2.25) was rewritten into Eq. (2.26) which, similarly to Eq. (2.12) takes curvature into account.

$$\mathrm{Nu}_c = \left(3.66 + \frac{0.065\frac{d_i}{L_c}\mathrm{RePr}}{1+0.04(\frac{d_i}{L_c}\mathrm{RePr})^{2/3}}\right)\left(1+0.015\mathrm{Re}^{0.75}(\frac{d_i}{D_c})^{0.4}\right) \tag{2.26}$$

Fig. 2.13 shows a comparison of the measured and predicted overall heat transfer coefficient during the generation of TBAB hydrate slurry when Eq. (2.19) and Eqs. (2.20)- (2.26) are used. The dashed frame in this figure shows the overall heat transfer coefficient for solid fraction lower than 15%. It should be stressed that Eqs. (2.20)-(2.24) have been derived from melting experiments and that it can be expected that the formation of hydrates encounters larger mass transfer resistances than melting when the solid concentration is lower than 15%. Fig. 2.13 shows that the experimental data can be predicted by Ma et al. (2010) [67], when the solid fraction is lower than 15 wt% and the flow rate is higher than 100 kg h^{-1} the flow is in the transition region between laminar and turbulent. It also shows that when the solid concentration is quite high (40%), the crystals will decrease the heat transfer of the flow. This can be caused by the adhesion of solids on the tube wall as shown in Fig. 2.13e. The heat transfer will be enhanced due to the curvature in coils as shown in Fig. 2.13a.

Most of the correlations for TBAB hydrate slurry focus on the melting process, while in this research, the generation process was investigated. Fig. 2.14 shows a comparison of the overall heat transfer coefficient of water, TBAB solution and TBAB hydrate slurry. It indicates that the heat transfer of water is higher than that of TBAB solution and TBAB slurry. This because the water is less viscous than the other two fluids. For slurry, when there are crystals formed on the wall of the tube it will increase the thermal resistance of the wall, thereby decreasing the overall heat transfer coefficient.

For slurry, when the flow rate is extremely high (flow velocity 1.2 m s^{-1}) with low solid fraction, the overall heat transfer coefficient is correspondingly high, which is comparable to that of TBAB solution, as shown in Fig. 2.14.

2.4.4. THICKNESS OF CRYSTAL LAYER

Hydrates are expected to form firstly on the wall of the coils forming a crystal layer as shown in Fig. 2.15. During the generation process of hydrate slurry, the adherence of crystals on the tube wall narrows the flow passage resulting in an increase of flow velocity. The enlarged velocity removes away the crystals formed on the wall. When there is a balance between the formation and removal of the hydrate crystals, the crystal layer will not increase anymore. The pressure drop of the TBAB hydrate slurry during generation in the coil heat exchanger increases in comparison with the situation before crystals start forming due to the gradually

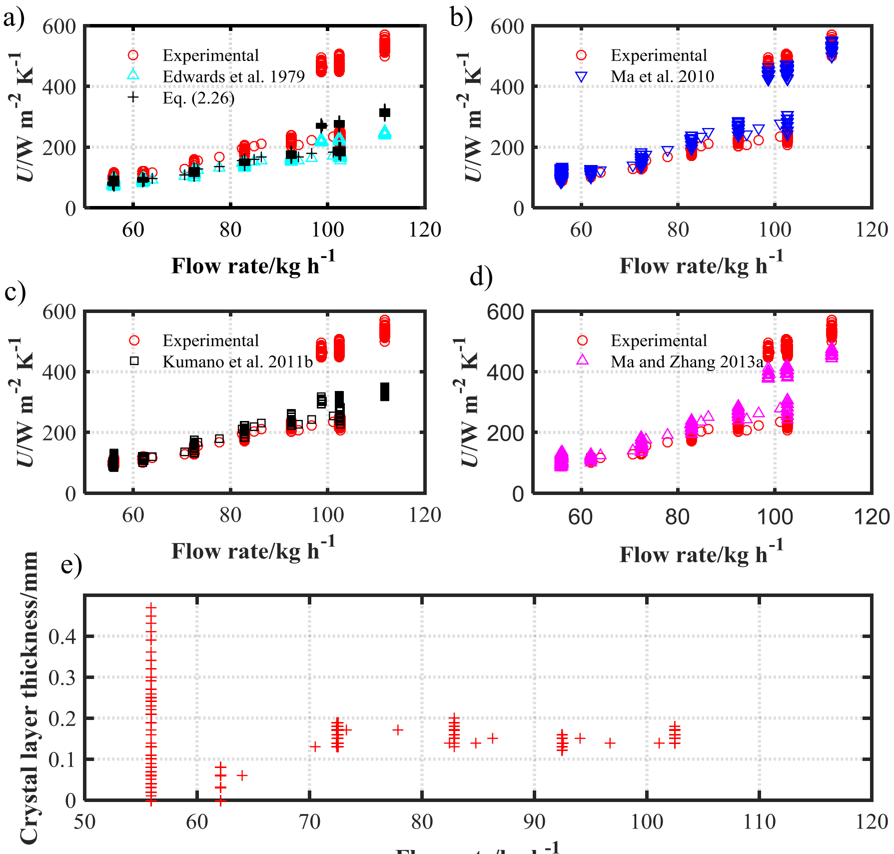

Figure 2.13: a) - d) Comparison of the experimental and predicted overall heat transfer coefficient during the generation of TBAB hydrate slurry Different resources have been used for comparison; e) Crystal layer thickness as a function of flow rate.

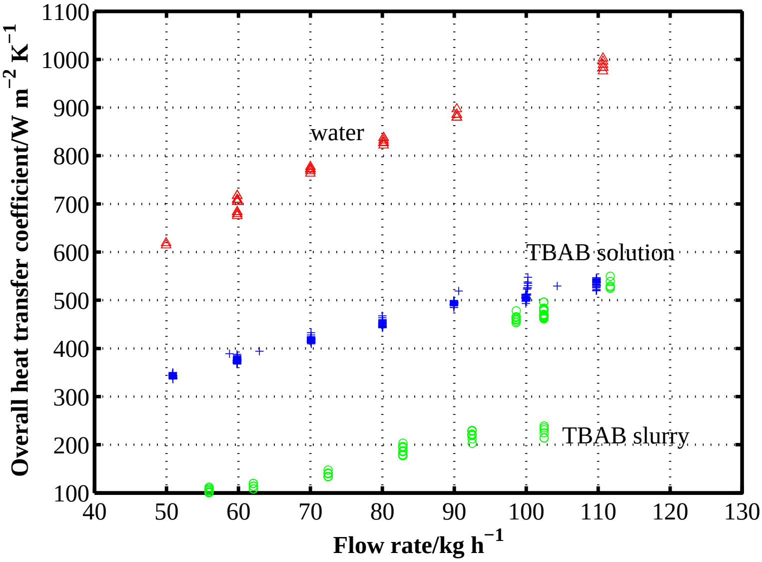

Figure 2.14: Comparison of the experimental overall heat transfer coefficient of water, TBAB solution and TBAB hydrate slurry as a function of flow rate.

thicker crystal layer on the tube wall and the reduced flow passage diameter, as shown in Fig. 2.15.

The thickness of the crystal layer δ can be derived from the iteration of the experimental overall heat transfer coefficient and the overall heat transfer coefficient obtained making use of Eqs. (2.1) and (2.27) taking the crystal layer thickness into account as

$$\frac{1}{U_{\text{after}}} = \frac{d_i}{d_H \times \alpha_i} + \frac{d_i \ln \frac{d_i}{d_H}}{2\lambda_H} + \frac{d_i \ln \frac{d_o}{d_i}}{2\lambda_w} + \frac{d_i}{d_o}\frac{1}{\alpha_o} \tag{2.27}$$

In which the thermal conductivity of hydrate is taken from Table 2.2 : 0.42 W m^{-1} K^{-1}.

The equilibrium crystal layer thickness which results for different operating conditions is shown in Fig. 2.13 as a function of flow rate. It indicates that the thickening of the crystal layer can seriously deteriorate the heat transfer performance of the slurry, the heat transfer coefficient decreasing from 500 W m^{-2} K^{-1} to 100 W m^{-2} K^{-1} when the crystal layer increases from zero to 0.15 mm.

2.5. CONCLUSIONS

The heat transfer characteristics and pressure drop during the formation of type A TBAB hydrate slurry in a coil heat exchanger have been investigated experi-

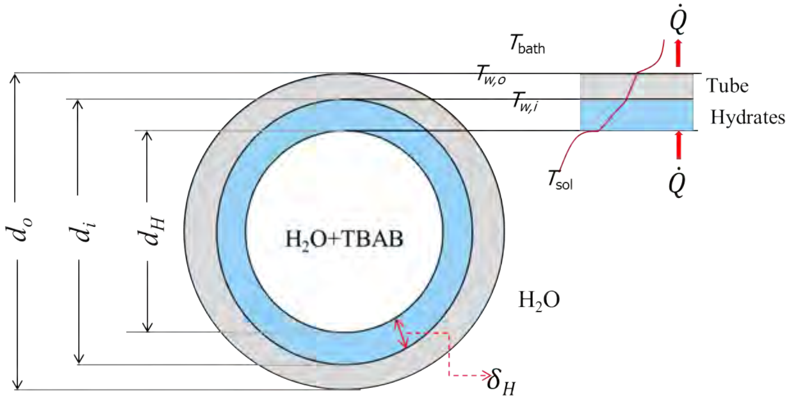

Figure 2.15: Schematic diagram of the coils with a layer of crystals formed on the wall, while the generation heat is removed by the external fluid.

mentally. Solid mass fraction and flow rate have been varied as experimental parameters.

Pressure drop of TBAB solution was about 2.6 –3.0 times that of the chilled water. For 30 wt% to 45 wt% TBAB hydrate slurry the pressure drop was in a range of 1.5 to 2.6 bar for the flow rates between 50 kg h^{-1} and 110 kg h^{-1}. Higher pressure drops are observed during crystal nucleation and growth. The pressure drop can be well predicted with existing correlations which take the curvature of the coil into account.

The experimental heat transfer data can be predicted with existing correlations. The heat transfer performance during hydrate formation is lower than that during hydrate melting. With high solid concentrations, the heat transfer of slurry is lower than that of TBAB solution and water under the same flow rate. With solid concentration $< 15\%$, the heat transfer coefficient of the slurry is comparable to the heat transfer coefficient of TBAB solution.

The formation of a layer of crystals in combination with increased viscosity increases the pressure drop during hydrate formation process, e.g., the pressure drop increases from 80 kPa to 240 kPa. The crystal layer also contributes to the determination of the overall heat transfer performance in the heat exchanger. The overall heat transfer coefficient can decrease from 500 W m^{-2} K^{-1} to 100 W m^{-2} K^{-1}.

3

TBAB HYDRATE SLURRY APPLICATION FOR A SMALL BUILDING

This chapter relates to the application of the topics introduced in Chapter 2. In this chapter, the TBAB hydrate slurry discussed in Chapter 2 is utilized in an air-conditioning system as a cold storage and distribution fluid. The air conditioning system is combined with a latent heat thermal storage (LHTS) system. The performance of this air conditioning system is compared with that of the conventional air conditioning system. The advantages of applying TBAB hydrate slurry as cold storage medium and distribution fluid are quantified.

Parts of this chapter have been published in the proceedings of the 11^{th} IIR Conference on Phase Change Materials and Slurries for Refrigeration and Air Conditioning, Karlsruhe, 2016

3.1. INTRODUCTION

Heating and cooling accounts for 37-49% of a building's energy consumption according to a study by the Energy Conservation Center, Japan (ECCJ) [42]. Energy use reduction in air conditioning is obviously vital to reduce the total energy consumption. The peak load for air conditioning power consumption is between 2 pm - 5 pm during the day as shown in Fig. 3.1. Air-conditioning systems are built to deal with this peak period. If the peak could be removed, the capacity of these facilities could be reduced and the operating efficiency could be increased. Leveling out this load fluctuation is called load leveling. The main purpose of thermal energy storage air conditioning systems making use of hydrate slurry is to contribute to load leveling. Fig. 3.1 shows the working principle of an air conditioning system which makes use of clathrate hydrate slurry (CHS) during a day. It indicates that the CHS is produced during the time between 22 pm - 8 am. During that period, the ambient temperature is low compared to daytime, therefore, the condensation temperature of the condenser could be reduced. In this way, the energy consumption of the primary refrigeration cycle can be reduced.

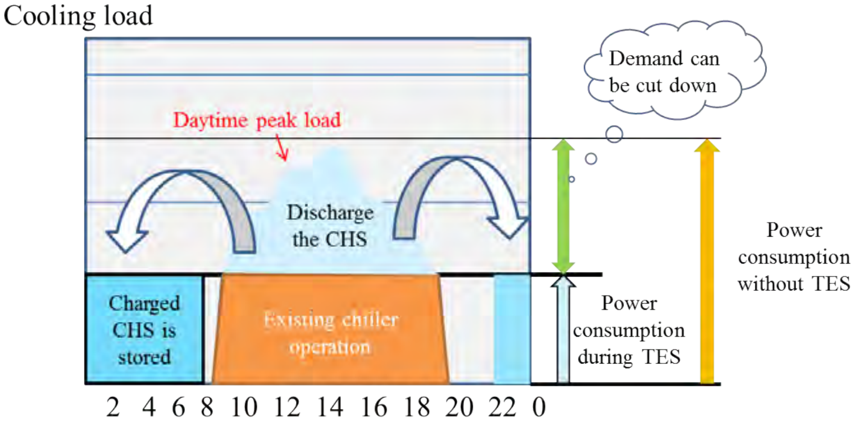

Figure 3.1: Working principle of CHS thermal energy storage air conditioning systems, adapted from [42]. It shows that the CHS is produced and stored during the night (2:00-8:00) and utilized during the day (9:00-20:00). In this way, the power consumption as illustrated can be cut down.

Fig. 3.1 also shows that with thermal energy storage (TES) system, the peak power consumption (marked in orange area) can be cut down. In this study, the thermal energy storage systems make use of aqueous TBAB slurry in the air conditioning system. The slurry is cooled and stored with night time power, and then cold air is generated during the day from the stored slurry. When energy consumption is dictated by the afternoon peak, peak power consumption is large to match that peak. However, when energy is stored at night, all that needs to be done at night is the storage task, so the primary refrigeration cycle can be operated steadily and very efficiently, energy consumption could be reduced as a result. An additional merit is being able to make effective use of cheaper night-time power and to operate the primary refrigerant cycle under more favorable operating conditions (lower condensation temperature).

The fundamental investigation of TBAB hydrate slurry including physical properties and mass and heat transfer characteristics has been reported in Chapter 2, which illustrated the possibility of applying TBAB hydrate slurry in air conditioning systems. In this chapter, an air conditioning system is discussed which makes use of TBAB hydrate slurry as cold storage and a cold delivery medium combined with a latent heat thermal storage (LHTS) system for a 144 m^2 space.

The thermo-physical properties and the related flow and heat transfer characteristics of TBAB hydrate slurry have been reviewed by Zhou et al. (2016) [135]. These authors concluded that TBAB hydrate slurry is suitable for the air conditioning applications due to its phase transition temperature which is close to the operation temperature of the conventional air-conditioning system, and its large cold storage density which is up to 5 times that of chilled water. The fluidity of TBAB hydrate slurry is maintained up to 40 wt% solid concentration. In this chapter, TBAB hydrate slurry is utilized as a secondary-loop refrigerant which is chilled down by the primary refrigerant. The produced hydrate slurry is distributed to an air-conditioning system of a specific building. The system is combined with a latent heat thermal storage system in order to shift the energy demand and therefore improve the energy efficiency. Both experimental and numerical methods are applied to investigate the performance of the system compared with that of conventional systems.

3.2. SYSTEM DESCRIPTION

3.2.1. EXPERIMENTAL SYSTEM

Fig. 3.2 shows the schematic diagram of the secondary refrigerant system which makes use of TBAB hydrate slurry. The system includes three loops: TBAB hydrate slurry generation, storage and application loop from right to left. TBAB hydrate slurries are produced in the plate heat exchanger (PHE) due to the heat removal by the refrigerant. The produced hydrate slurry is stored in the storage vessel (SV), and delivered to the air-cooler when there is cooling requirement. The installation of the system is shown in Appendix B. The peak cooling load of the system is 3 kW taking the Dutch climate (the five hottest days during the year of 1965) for estimation.

A plate heat exchanger (PHE) which is purchased from Alfal Laval (AC-70x-

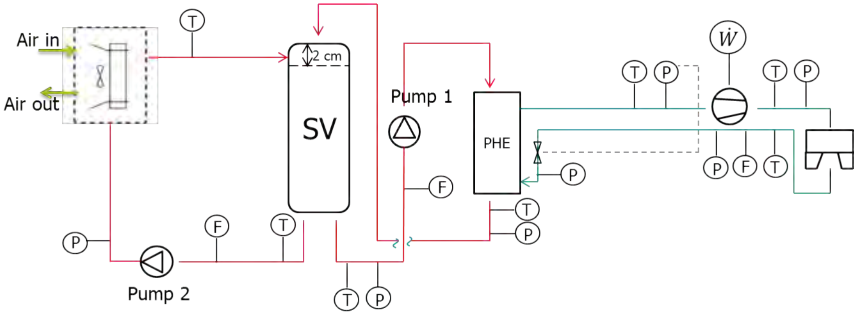

Figure 3.2: Schematic diagram of the refrigeration system making use of TBAB hydrate slurry as secondary fluid.

30m) with dimension of 111 mm × 526 mm × 104 mm (with 12.5 mm from the center of top tube port to the top of the plate Fig. 3.3d), consists of thin corrugated stainless steel plates vacuum brazed together using copper as the brazing material as shown in Fig. 3.3a. Fig. 3.3b shows the basic flow principle of a plate heat exchanger, the two fluids flow normally counter currently to achieve the most efficient heat transfer process. The heat exchanger used in this research is composed of 30 plates, getting a heat transfer area of about 2.0 m^2 taking the plate surface enhancement of corrugations into account. The installation of the PHE in this research is shown as Fig. 3.3c. The effective length of each plate is 0.501 m.

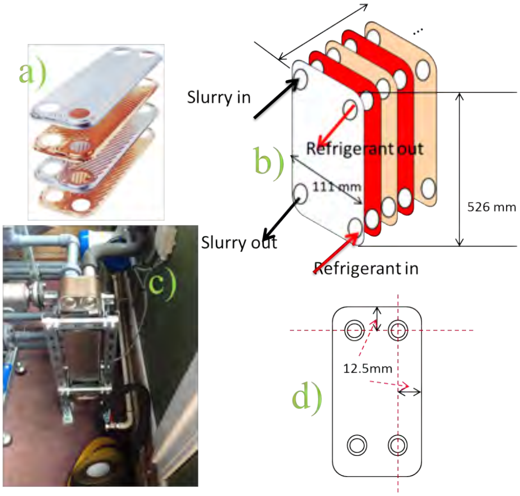

Figure 3.3: a) Plates of brazed plate heat exchanger b) Schematic diagram of the plate heat exchanger utilized in this research c) Plate heat exchanger installed in this research with the same size represent in b); d) Structure of a plate.

The storage vessel (SV as shown in Fig. 3.2) which is used to store the hydrate slurry produced from the generation loop, is maintained at atmospheric pressure. The storage vessel is made of a polymeric material and has a volume of 0.3 m^3 with a height of 1 m. Fig. 3.4 illustrates its installation.

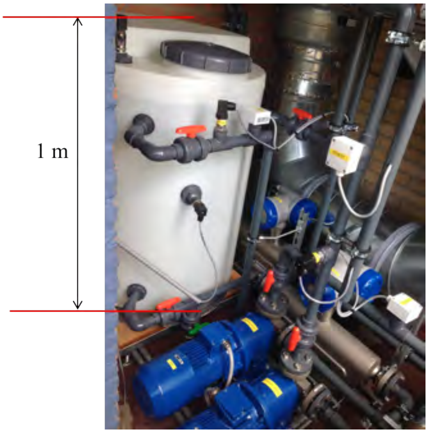

Figure 3.4: Storage vessel installed in the system with a volume of 0.3 m^3 and height of 1 m.

The hydrate slurry stored in the storage vessel is delivered to the application loop making use of an air cooler. The function of the air-cooler is to cool the air flow that is delivered to the conditioned space to a certain temperature level by heat exchange with the TBAB hydrate slurry. In this study, TBAB hydrate slurry is utilized as the cooling medium and distribution fluid instead of water which is commonly used in conventional air-conditioning systems. The air cooler used in this research is a tube-fin exchanger as shown in Fig. 3.5 as example. The external (air side) surface of this exchanger is enhanced with continuous fins to compensate for the low heat transfer coefficient in the air side.

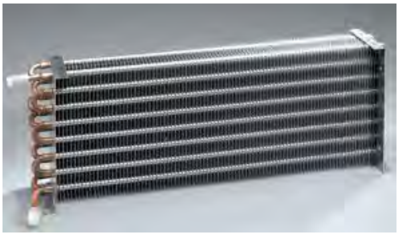

Figure 3.5: Example of a tube-fin air cooler with plate fins. The cooler used in this experimental set-up has a finned length of 600 mm and 375 mm width and it has 6 tube rows in the air flow direction.

The installation of the tube-fin air cooler in this research is shown as Fig.

3.6. The connection and the distribution of the tubes is shown as Fig. 3.7a. Water/TBAB hydrate slurry flows into the header and is distributed to 15 circuits as shown in Fig. 3.7a. There are two columns in each circuit, each column contains 6 tubes. The length of one tube, L_t, as shown in Fig. 3.7b is 0.6 m. The diameter of the tube is 9.52/10 (d_i/d_o) mm, which gives an internal heat transfer area of 3.2 m^2 in total. The tube pitch (p_t) and row pitch (p_r) are identical and equal to 25 mm. The fin height, H_{fin}, is an important design parameter of the fin tube air cooler, which can be derived from Schmidt (1950 [92]). The fin thickness (W_{fin}) and fin spacing (s_{fin}) are two design parameters that are important for the performance of the air cooler. The fin pitch (p_{fin}) is 4.2 mm, and the thickness of each fin is 0.2 mm for the air cooler used in this research.

Figure 3.6: The installation of the tube-fin air cooler surrounded by a red circle. The two horizontal headers used to distribute the flow of hydrate slurry into 15 parallel circuits is clearly visible. Each vertical row of tubes is a different circuit.

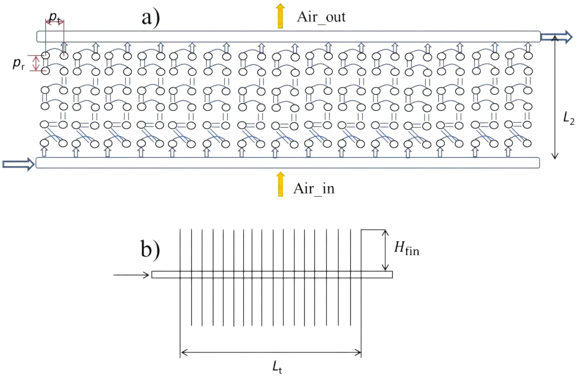

Figure 3.7: a) Side view of the geometry of air-cooler; The length in the air flow direction, L_2, is 150 mm; The tube pitch, p_t, and row pitch, p_r, are both 25 mm. b) front view of one of the tubes showing how the fins are attached to the tubes. The length of each tube, L_t, is 0.6 m.

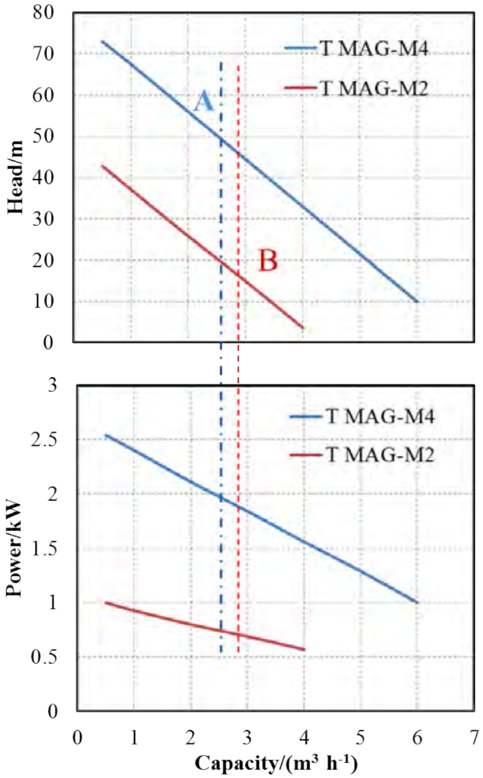

Figure 3.8: Characteristics of the two magnetically driven pumps shown in Fig. 3.2. T MAG-M4 is Pump 1 and T MAG-M2 is Pump2.

There are two pumps used as shown in Fig. 3.2 which are magnetically driven peripheral pumps. Both pumps are speed controlled. The flow rate of pump 1 (T MAG-M4) is 2.5 m^3 h^{-1} with maximum pressure drop of 5.0 bar. Pump 2 (T MAG-M2) delivers the hydrate slurry stored in the storage vessel to the application site. The flow rate of pump 2 is 2.9 m^3 h^{-1} with maximum pressure drop of 1.8 bar. The pressure drop over the two pumps is continuously measured. The solid fraction is also measured making use of density measurements with Coriolis mass flow meters. This allows for the determination of the relation between solution pressure drop and its corresponding solid fraction. In the future, the pressure drop could be used as an indication of the solid fraction if a relation can be identified between these two parameters. The performance diagrams of the pumps are shown as Fig. 3.8. The blue line indicates that when there is a blockage under the designed flow rate, by regulating the flow rate, pump 1 can deliver up to 6 bar pressure drop which is supposed to be enough according to the pressure drop behavior in relation to a blockage illustrated in Chapter 2.

The efficiency of the two pumps can be derived by the definition as $\eta = \frac{\dot{V}\Delta P}{W_{\text{pump}}}$. For pump 1 the efficiency is derived to be 17%. For pump 2 the efficiency is 21%.

SIZE OF THE CONNECTING TUBES

The external diameter of the tubes between the storage vessel and the plate heat exchanger is 25 mm. The refrigerant inlet tube to the plate heat exchanger is 16 mm while the outlet tube is 28 mm. The diameter of the tube which connects the storage vessel with the air-cooler is also 25 mm external.

DATA ACQUISITION

The data acquisition system is comprised of a data logger which measures the data every 10 seconds. The data logged is obtained with several transducers namely: temperature sensors, pressure sensors and flow meters. Temperatures are measured using Pt100 thermal resistance sensors. The resulting accuracy of the thermal resistance when measuring temperature relative to each other is ±0.03 K. The pressure transducers used to measure the pressure in different locations are calibrated to ± 1 kPa. The flow meters are calibrated to be ± 0.15 for flow measurement and ± 0.5 kg m^{-3} for density measurement and have been obtained from Krohne Ltd. Table 3.1 summarizes the accuracy of all sensors.

Table 3.1: Summary of instrumentation accuracies.

Parameters	Accuracy
Temperature, K	± 0.03
Pressure, kPa	± 1
Density, kg m^{-3}	± 0.5
Flow rate % of full scale	± 0.15

3.2.2. EXPERIMENTAL METHODOLOGY

The operation of the system which is controlled by a computer program is shown in Fig. 3.9. Before the system is started, distilled water has been used to rinse the internal area of the system.

As shown in Fig. 3.9, the experiments will be run in two modes: day-time and night-time which is determined by a time controller. During daytime, when there is cooling requirement, the slurry stored in the vessel will be firstly used until the density of the slurry in the storage vessel is low (density corresponding to 5 wt%) then the hydrate slurry production will start. This control process is shown as the two branches in Fig. 3.9. For the night mode, the production of hydrate slurry is processed until the density corresponding to 40 wt% is reached. In addition, the density is measured by a Coriolis flow meter and indicates the

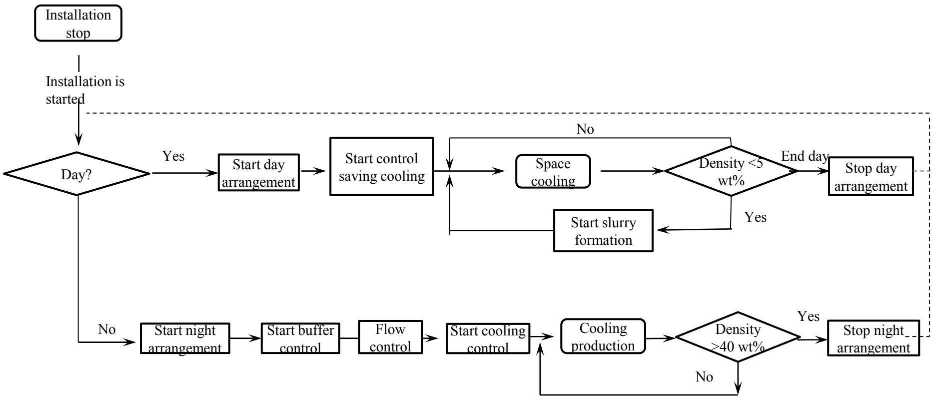

Figure 3.9: Installation operation of TBAB hydrate slurry air conditioning system.

corresponding concentration of solids. The set point for the maximum concentration of solids is 40 wt% in the storage tank. The lowest concentration allowed during the day mode is 5 wt%. The hydrate concentration application range is 5 wt% - 40 wt%, since the investigation of the flow characteristics discussed in Chapter 2 indicates that above 40 wt%, the pressure drop of the slurry rises significantly and the melting of all crystals requires a large supercooling to re-initiate the formation of crystals.

3.3. MODEL DEVELOPMENT

A mathematical model has been developed to calculate the performance of the hydrate slurry air conditioning system. The model consists of several components. Fig. 3.10 illustrates that the general inputs of the model are the cooling demand and ambient temperature. From the program, the corresponding value of the power consumption which is one of the outputs of the system is calculated.

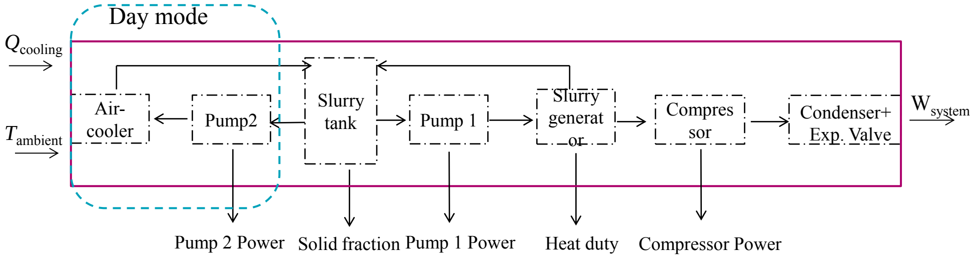

Figure 3.10: General model description of the TBAB hydrate slurry air conditioning system.

Fig. 3.10 also shows that the program runs the sub-models in the following order:

if the system is running in the day time mode:

- Air cooler: slurry mass flow in the application site is firstly calculated as a function of cooling demand and ambient temperature.
- Pump 2: Calculates pump power from air cooler pressure loss.

if the solid fraction in the storage tank is lower than 5 wt%, then the generation is started.

- Slurry generator: the heat capacity of the slurry generator is calculated based on the overall heat transfer coefficient of TBAB hydrate slurry as $\dot{Q} = UA\Delta T$. A mass flow of slurry is firstly assumed. The U value can then be derived. ΔT is based on the evaporation temperature which is fixed as 2/7.5 °C. The slurry mass flow in the generator site can then be derived from $\dot{m}_s = \dot{Q}/\Delta h_s$. The iteration runs until it converges.
- Pump 1: Calculates pump power from slurry generator pressure loss.
- Compressor: Calculates condensation temperature from refrigerant mass flow, inlet temperature, air mass flow and ambient temperature.
- Expansion valve: Calculates outlet enthalpy from inlet enthalpy.
- Slurry tank: Calculates slurry solid fraction from in and outlet mass flows and solid fraction.

if the system is running in the night-time mode, the solid fraction in the storage tank is firstly judged, if it is lower than 40 wt%, then the generation will start. The steps will follow as below until the concentration of solids is up to 40 wt% then the system will shut down.

- Slurry generator: Slurry mass flow is calculated using the same method as for day mode.
- Pump 1: Calculates pump power from slurry generator pressure loss.
- Compressor: Calculates condensation temperature from refrigerant mass flow, inlet temperature, air mass flow and ambient temperature.
- Expansion valve: Calculates outlet enthalpy from inlet enthalpy.
- Slurry tank: Calculates slurry solid fraction from in and outlet mass flows and solid fraction.

3.3.1. HEAT TRANSFER AND PRESSURE DROP IN TUBE-FIN AIR COOLER

Slurry mass flow through air-cooler is firstly calculated from

$$\dot{m} = \frac{\dot{Q}}{\Delta h_s} \tag{3.1}$$

In which, Δh_s is the enthalpy change of the slurry, composed of solid and solution as $\Delta h_s = \Delta w \Delta h_H + \Delta h_{\mathrm{sol}}$. Δw is the solid concentration change of the slurry as it flows through the air cooler. Δh_H is the latent heat of type A TBAB hydrate, which is 193 kJ kg^{-1}. $\dot{Q}$ is the cooling demand.

HEAT TRANSFER PERFORMANCE

The heat transfer performance of the air cooler is analyzed for both air side and slurry side.

For slurry flow side, Song et al. (2009) [103] proposed a correlation for the prediction of the Nusselt number of forced convective heat transfer of melting TBAB hydrate slurry

$$\mathrm{Nu} = A^{'}\mathrm{Re}_M^{a^{'}}\mathrm{Pr}^{b^{'}} \tag{3.2}$$

In which, Re_M is the modified Reynolds number, which has been defined in Chapter 2.

The values for the parameters are listed in Table 3.2. The heat transfer coefficient of the slurry side can then be derived from $\alpha_{s_{\mathrm{cooler}}} = \frac{\lambda_s \mathrm{Nu}}{d_i}$. In which, the slurry thermal conductivity is composed of solution and solids and d_i is the internal diameter of the tube.

Table 3.2: Parameters of heat transfer correlation in Eq. (3.2).

Flow Regime	$A^{'}$	$a^{'}$	$b^{'}$	Range (Re_M)
Laminar	1.231×10^{-5}	1.6606	0.7073	$\leqslant 17500$
Turbulent	5.254×10^{-4}	0.9097	1.1202	$\geqslant 17500$

A correlation proposed by Infante Ferreira [45] for air coolers with in-line arrangement has been adopted as Eq. (3.3) for the calculation of heat transfer for the present air-cooler as shown in Fig. 3.7.

$$\mathrm{Nu}_{\mathrm{air}} = 0.265\mathrm{Re}^{0.78}\mathrm{Pr}^{1/3}\left(\frac{L}{d_h}\right)^{-0.7} \tag{3.3}$$

Where, d_h is the hydraulic diameter of external tube-fin. It is derived by Eq. (3.4) to be 6.3 mm.

$$d_h = \frac{4(p_t - d_o)(p_{\text{fin}} - W_{\text{fin}})}{2(p_{\text{fin}} - W_{\text{fin}}) + 2(p_t - d_o)} \tag{3.4}$$

L in Eq. (3.3) is the air flow path, which is L_2 as shown in Fig. 3.7 and is equal to 0.15 m. Re in Eq. (3.3) is defined as

$$\text{Re} = \frac{\dot{G}_{\text{air}} d_h}{\mu_{\text{air}}} \tag{3.5}$$

In which, $\dot{G}_{\text{air}}$ is the air mass flux across fins which is obtained from

$$\dot{G}_{\text{air}} = \frac{\dot{m}_{\text{air}}}{(p_t - d_o)(p_{\text{fin}} - W_{\text{fin}}) N_t \frac{L_t}{p_{\text{fin}}}} \tag{3.6}$$

N_t is the number of tube rows perpendicular to the air flow direction. The heat transfer coefficient for the air side is derived from $\alpha_{\text{air}} = \frac{\lambda_{\text{air}} Nu_{\text{air}}}{d_h}$.

The overall heat transfer coefficient of the tube fin air cooler is then derived as Eq.(3.7) making use of Eqs. (3.2) and (3.3).

$$\frac{1}{U_{\text{air}}} = \frac{1}{\alpha_{s_{\text{cooler}}}} + \frac{d_i}{2\lambda_{\text{t}}} \ln\frac{d_o}{d_i} + \frac{d_o}{2\lambda_{\text{fin}}} \ln\frac{d_{o_{\text{fin}}}}{d_o} + \frac{1}{\alpha_{\text{air}}} \frac{1}{\left(\frac{A_{\text{fin}}}{A_i}\eta_{\text{fin}} + \frac{A_{\text{t}}}{A_i}\right)} \tag{3.7}$$

Where $A_i = \pi d_i L_t N_t N_r = 3.228\ \text{m}^2$. N_t, N_r are the tube rows perpendicular to the air flow direction and in air flow direction, which are 30 and 6 respectively. The exposed tube area, A_{t} can be calculated as $A_{\text{t}} = \pi d_{o_{\text{fin}}} (L_t - \frac{L_t}{p_{\text{fin}}} W_{\text{fin}}) N_t N_r$, which is $3.231\ \text{m}^2$. For square pitch tube bank, the fin area is obtained from Eq. (3.8), which is $28.1\ \text{m}^2$ for the present heat exchanger.

$$A_{\text{fin}} = N_t N_r \frac{L_t}{p_{\text{fin}}} 2[p_t p_r - \frac{\pi d_{o_{\text{fin}}}^2}{4}] \tag{3.8}$$

Fin efficiency in Eq. (3.7) is calculated from

$$\eta_{\text{fin}} = \frac{\tanh(pH_{\text{fin}})}{pH_{\text{fin}}} \tag{3.9}$$

Where p is a fin efficiency parameter. It's defined as

$$p = \sqrt{\frac{2\alpha_{\text{air}}}{\lambda_{\text{fin}} W_{\text{fin}}}} \tag{3.10}$$

H_{fin} is the height of the fin, which is derived to be 12.4 mm from Schmidt (1950) [92].

$$H_{\text{fin}} = 0.5(2\sqrt{\frac{p_t p_r}{\pi}} - d_o)[1 + 0.35\ln(2\frac{\sqrt{\frac{p_t p_r}{\pi}}}{d_o})] \tag{3.11}$$

The material of the fins is aluminum.The thermal conductivity, λ_{fin} is 205 W m^{-1} K^{-1} at ambient temperature. The tube is made of copper, the thermal conductivity of tube wall, λ_w, is then 400 W m^{-1} K^{-1}.

The correlation from Schmidt (2010) [90] for heat transfer in finned tubes is used for comparison purposes.

$$\text{Nu}_{\text{air}} = 0.22Re^{0.6}\left(\frac{A_{\text{tot}}}{A_{\text{t}}}\right)^{-0.15} Pr^{1/3} \tag{3.12}$$

PRESSURE DROP

The tube side pressure drop of the air cooler was predicted using the same equation (Eq. (2.10)) as shown in Chapter 2 for single phase flow in straight tubes. For air side pressure drop, the correlation from [45] is taken for the calculation.

$$\Delta P_{\text{air}} = \frac{1}{2} f \frac{(G_{\text{air}})^2}{\rho_{\text{air}}} \tag{3.13}$$

Where, f is the fanning factor. For different Reynolds numbers, f is derived as below.
For Re < 1500

$$f = 100\text{Re}^{-0.82}\left(\frac{L_2}{d_h}\right)^{0.7} \tag{3.14}$$

For Re > 1500

$$f = 0.7\text{Re}^{-0.14}\left(\frac{L_2}{d_h}\right)^{0.7} \tag{3.15}$$

3.3.2. PUMP POWER CALCULATION

The power consumption of the pump is calculated based on the pressure loss in the heat exchanger. For pump 2, the power consumption can be derived from

$$W_{\text{pump}} = \frac{\dot{m}_s \Delta P_{\text{t}}}{\eta_{\text{pump}} \rho_s} \tag{3.16}$$

while for pump 1, the pressure loss in the slurry generator would be taken.

3.3.3. Slurry generator

For day mode, the slurry stored in the storage tank is enough to supply the cooling demand, so there is no slurry flow through the generator during the day-time. For night mode, the cooling capacity for the generator has been discussed above, thereby, the mass flow of the refrigerant is then derived as

$$\dot{m}_{\mathrm{ref}} = \frac{\dot{Q}}{\Delta h_{\mathrm{ref}}} \tag{3.17}$$

Hydrate growth model in PHE

TBAB hydrate slurry has been generated by super-cooling a TBAB solution with a concentration of 36.5 wt%, followed by nucleation and then growth of the hydrate crystals. The hydrate formed during the process is calculated from a hydrate growth model, the heat released by hydrate formation can then be derived, which will be compared with the heat removed by the refrigerant. In this way, the growth model can be validated.

Crystals are expected to form on the wall of the plate heat exchanger firstly as shown in Fig. 3.11 since the temperature of the wall is lower than the temperature of the solution. The crystal layer thickness keeps increasing and thus the slurry velocity also increases according to the conservation of mass until the friction between the slurry and the crystal layer is high enough causing detachment of crystals from the layer into the slurry. At this point, the mass of crystals that are formed in the layer equals to the mass of crystals that are transported to the slurry and the crystal layer thickness remains constant since then.

A modified model of Pronk [84] is used, in this study, to describe the crystal growth mechanism.

$$G = k\rho_s A(w_{\mathrm{sol}} - w_{\mathrm{int}}) \tag{3.18}$$

Where k is the mass transfer coefficient, and can be derived from

$$k = \frac{\mathrm{Sh}D}{d_h - 2\delta_H} \tag{3.19}$$

In which the Sherwood number is predicted making use of the analogy with heat transfer and using the correlation from Warnakulasuriya and Worek (2008) [115] for viscous flows in plate heat exchangers.

$$\mathrm{Sh} = 0.292 Re^{0.705} Sc^{0.35} {\frac{\mu}{\mu_w}}^{0.14} \tag{3.20}$$

This equation has been adopted since it is similar to the equation experimentally validated by Gudjonsdottir (2015) [39] and it includes the impact of the high viscosity of the slurry.

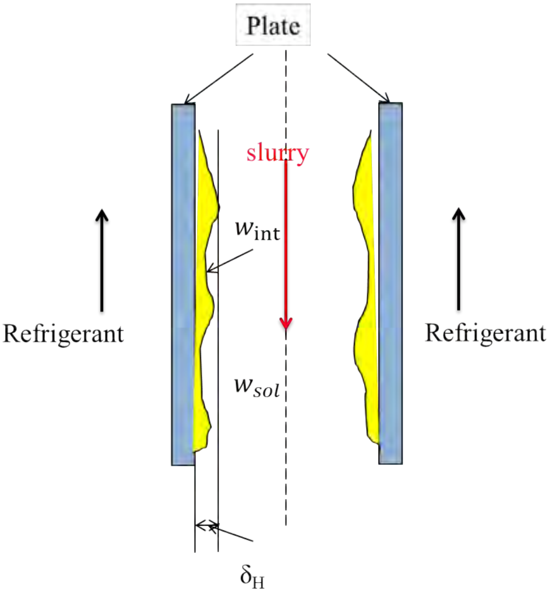

Figure 3.11: TBAB hydrate (marked with yellow) growth on the plate surface of the plate heat exchanger. The TBAB solution and the refrigerant flow counter-currently on the two sides of the plate. The driving force for the formation is the concentration difference between solution (w_{sol}) and the interface (w_{int}). A crystal layer thickness, δ_H, must first be attained before continous production can be achieved.

d_h is the hydraulic diameter of the PHE. The crystal layer, δ_H, shown in Fig. 3.11, is estimated to be 0.15 mm according to Zhou et al. (2016)[135]. The authors derived the thickness of crystal layer during TBAB hydrate slurry production in a tube heat exchanger. They concluded that when the flow velocity is above a certain value, there is a constant layer of crystals on the tube wall when there is a continuous production of hydrates.

This model has been validated with experiments of TBAB hydrate slurry generation in a coil heat exchanger, from which the diffusion coefficient, D, of TBAB in aqueous solutions has been derived to be 1.52×10^{-7} m^2 s^{-1} (Zak, 2014[128]).

HEAT TRANSFER IN PHE

The correlation from Warnakulasuriya and Worek (2008)[115] has been used for the heat transfer calculation in the slurry side of the PHE. Their correlation has been derived for the heat transfer in plate heat exchangers for high viscous solutions.

$$\mathrm{Nu} = 0.292\mathrm{Re}^{0.705}\mathrm{Pr}^{0.35}\,{\frac{\mu}{\mu_w}}^{0.14} \tag{3.21}$$

Ma and Zhang (2011) [64] have investigated the heat transfer performance of TBAB hydrate slurry in a plate heat exchanger with solid fractions in the range from 0 - 17.5%. They obtained a correlation for the heat transfer coefficient based on their experimental data taking the influence of solid fraction into consideration. Therefore, their correlation is also considered for comparison purposes.

$$\mathrm{Nu}_{MaZhang} = 0.338\mathrm{Re}_M^{0.667}\mathrm{Pr}^{1/3}\left(1+\frac{\Delta w \Delta h}{c_p \Delta T}\right)^{0.037} \tag{3.22}$$

Recently Gudjonsdottir (2015)[39] has reviewed heat transfer and pressure drop studies in plate heat exchangers with single phase flow and refrigerant evaporation. By comparing several proposed correlations with experimental data collected with ammonia as the refrigerant and water as the single phase fluid she concluded that, for single phase flow, the correlation which reproduces best her experimental data is the correlation by Donowski and Kandlikar (2000) [22]. If the solid fraction change is small, the slurry could be treated to be a single phase flow to some extent, therefore, Eq. (3.23) is also used for comparison purposes.

$$\mathrm{Nu}_{\mathrm{sp}} = 0.2875\mathrm{Re}_{\mathrm{sp}}^{0.78}\mathrm{Pr}_{\mathrm{sp}}^{1/3} \tag{3.23}$$

Which applies for $\mathrm{Re}_{\mathrm{sp}} > 200$.

For evaporation the correlation by Yan and Lin (1999) [120] approached best the experimental data:

$$\mathrm{Nu}_{\mathrm{evap}} = 19.26\mathrm{Re}_{\mathrm{eq}}\mathrm{Re}_L^{-0.5}\mathrm{Pr}_L^{1/3}\mathrm{Bo}_{\mathrm{eq}}^{0.3} \tag{3.24}$$

In this equation the subscript eq indicates the equivalent dimensionless number which takes the local vapor fraction into account.

Cooper's equation which has been validated by Longo and Gasparella (2007) [62] in a small brazed plate heat exchanger for R134a vaporisation is also used for comparison purposes.

$$\alpha_{ref_{\mathrm{Cooper}}} = 55\left(\frac{P}{P_{\mathrm{crit}}}\right)^{0.12-0.2log_{10}(R_p)}\left(-\log_{10}(\frac{P}{P_{\mathrm{crit}}})\right)^{-0.55}\dot{q}^{0.67}M^{-0.5} \tag{3.25}$$

3.3.4. PRESSURE DROP IN PHE

The pressure drop prediction method proposed by Kast and Nirschl (2010)[50] (Eq.(3.26)) has been used to predict the single phase flow pressure drop.

$$\Delta P = f\frac{L_{\mathrm{phe}}}{d_h}\frac{\rho u^2}{2} \tag{3.26}$$

In which, d_h is the hydraulic diameter of the plate heat exchanger, which is 5.6 mm. f is the friction factor that depends on Reynolds number.
For laminar flow

$$f = \frac{64}{\mathrm{Re}} \tag{3.27}$$

For turbulent flow, according to Blasius, Eq. (3.28) is applied for 3000 < Re < 100000.

$$f = \frac{0.3164}{\mathrm{Re}^{0.25}} \tag{3.28}$$

For higher range from $2 \times 10^4 < \mathrm{Re} < 2 \times 10^6$, Hermann's equation [50] is applied

$$f = 0.00540 + \frac{0.3964}{\mathrm{Re}^{0.3}} \tag{3.29}$$

While the pressure drop during evaporation was predicted with the correlation by Han et al. (2003)[41].

$$\Delta P = f\frac{L_{\mathrm{phe}} N_{cp}}{d_h}\frac{\dot{G}_{\mathrm{eq}}^2}{\rho_L} \tag{3.30}$$

In which N_{cp} is the number of passes which is one for the present set-up. $\dot{G}_{\mathrm{eq}}$ is the equivalent mass flux, which can be calculated by

$$\dot{G}_{eq} = \dot{G}[(1 - q_v) + q_v(\frac{\rho_L}{\rho_v})] \tag{3.31}$$

q_v is the vapor quality.

The overall heat transfer coefficient for the plate heat exchanger utilized in this study can then be derived from Eq. (3.32) making use of Eqs. (3.24) and (3.21)

$$\frac{1}{U} = \frac{1}{\alpha_{s_{\mathrm{phe}}}} + \frac{1}{R_w} + \frac{1}{\alpha_{\mathrm{evap}}} + \frac{\delta_H}{\lambda_H} \tag{3.32}$$

The plate heat exchanger is made of stainless steel, therefore, the thermal conductivity of the wall is 15 W m^{-1} K^{-1}, the resistance of the wall is derived as $R_w = \frac{\lambda_w}{\delta_w}$. The thermal conductivity of TBAB hydrate, λ_H, is 0.42 W m^{-1} K^{-1} according to Table 2.2.

3.3.5. MATHEMATICAL MODEL OF THE COLD STORAGE OF TBAB HYDRATE SLURRY

Fig. 3.12 shows a schematic diagram of the storage vessel (SV) of TBAB hydrate slurry. It is both connected to the plate heat exchanger where crystals are produced and to the melting heat exchanger in which part of the flow is molten. Fig.

3.12 also shows that a cooling load $\dot{Q}$ is applied to the slurry flow as it passes the melting heat exchanger. The heat exchanger is installed in the air feed channel to the conditioned space. The storage vessel is well insulated and the temperature between environment and storage is quite small so that it can be assumed that the energy input from the environment through the insulation material is negligible. The storage vessel is considered to be well-mixed so that a single control volume can represent the conditions encountered in practice. The enthalpy at the outlet of the melting heat exchanger is given by Eq. (3.33)

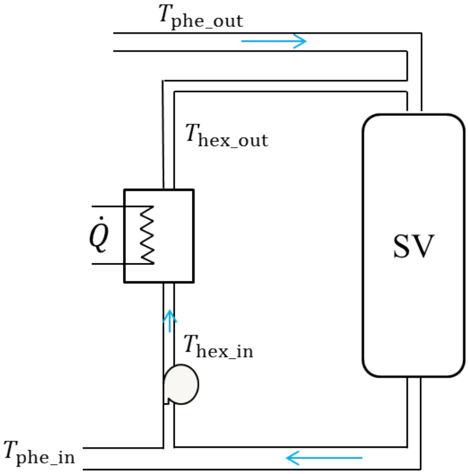

Figure 3.12: Storage vessel (SV) and melting heat exchanger (HEX). The arrows denote the flow direction. Partially molten slurry and slurry from the plate heat exchanger (PHE) mix and flow into the storage vessel (SV).

$$h_{hex_{\text{out}}} = h_{hex_{\text{in}}} + \frac{\dot{Q}}{\dot{m}_{\text{hex}}} \tag{3.33}$$

The enthalpy of the slurry at the inlet of the storage vessel is given by

$$h_{sv_{\text{in}}} = \frac{\dot{m}_{\text{hex}} h_{hex_{\text{out}}} + \dot{m}_{\text{phe}} h_{phe_{\text{out}}}}{\dot{m}_{\text{hex}} + \dot{m}_{\text{phe}}} \tag{3.34}$$

The energy input from the pump is negligible so that $T_{\text{sv}_{\text{out}}} = T_{\text{hex}_{\text{in}}} = T_{\text{phe}_{\text{in}}}$ and the enthalpy at the outlet of the storage vessel can be derived from the temperature and solid fraction as Eq.(3.35)

$$h_{\text{sv}_{\text{out}}} = f(T_{\text{sv}_{\text{out}}}, w_{\text{in}_{\text{sv}}}) \tag{3.35}$$

The mass concentration at the outlet of the melting heat exchanger, $w_{\mathrm{hex}_{\mathrm{out}}}$, follows from the melting enthalpy of the crystals as given

$$w_{\mathrm{hex}_{\mathrm{out}}} = w_{\mathrm{sv}_{\mathrm{out}}} - \frac{\dot{Q}_{\mathrm{hex}}}{\dot{m}_{\mathrm{hex}} \Delta h_H} \tag{3.36}$$

The solid concentration from the plate heat exchanger, $w_{\mathrm{phe}_{\mathrm{out}}}$, can be derived in a similar way as for Eq. 3.36

$$w_{\mathrm{phe}_{\mathrm{out}}} = w_{\mathrm{sv}_{\mathrm{out}}} + \frac{\dot{Q}_{\mathrm{phe}}}{\dot{m}_{\mathrm{phe}} \Delta h_H} \tag{3.37}$$

So that the hydrate mass concentration at the inlet of the storage vessel, $w_{H_{\mathrm{sv}_{\mathrm{in}}}}$, can be obtained from

$$w_{H_{\mathrm{sv}_{\mathrm{in}}}} = \frac{\dot{m}_{\mathrm{hex}} w_{\mathrm{hex}_{\mathrm{out}}} + \dot{m}_{\mathrm{phe}} w_{\mathrm{phe}_{\mathrm{out}}}}{\dot{m}_{\mathrm{hex}} + \dot{m}_{\mathrm{phe}}} \tag{3.38}$$

The hydrate mass concentration in the storage vessel, $w_{H_{\mathrm{sv}}}$, as a function of time can finally be obtained from

$$w_{H_{\mathrm{sv}}} = \int \frac{(\dot{m}_{\mathrm{hex}} + \dot{m}_{\mathrm{phe}}) w_{H_{\mathrm{sv}_{in}}} - (\dot{m}_{\mathrm{hex}} + \dot{m}_{\mathrm{phe}}) w_{H_{\mathrm{sv}}}^{t-1}}{\rho_{\mathrm{sv}} V_{\mathrm{sv}}} dt \tag{3.39}$$

Where the superscript $t-1$ indicates the value for the previous time step.

3.3.6. COMPRESSOR POWER CONSUMPTION

A Bitzer LH44E/2FES-3Y condensing unit is used in this study, including a 2FES-3Y-40S compressor. The compressor has 2 cylinders, with 46 mm bore and 33 mm stroke.

The power consumption of the compressor is obtained from the volumetric and isentropic efficiencies. Both are a function of the pressure ratio and the inlet temperature. The isentropic and volumetric efficiency of the compressor are obtained from a calculation model by the manufacturer (Bitzer). The result is shown in Fig. 3.13 indicating that the isentropic and volumetric efficiency are only a function of the pressure ratio. The influence of the temperature at the inlet of the compressor is neglected since it remains partially unchanged for the considered operating conditions. The pressure ratio does vary over time since it depends on the ambient temperature.

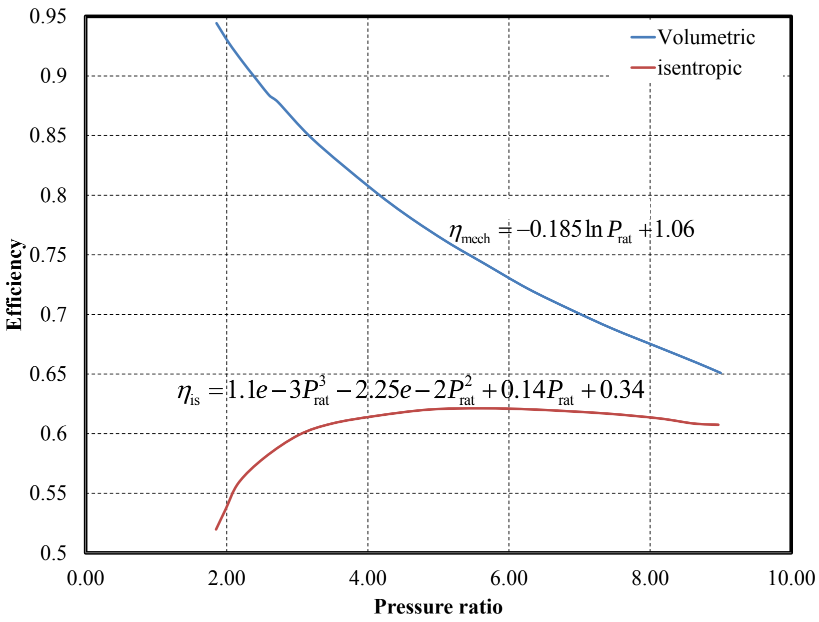

Figure 3.13: Isentropic (η_{is}) and volumetric (η_{vol}) efficiencies of the compressor as functions of pressure ratio (P_{rat}). The fitting correlations of both efficiencies are also shown in the figure.

The enthalpy at the outlet of the compressor can be calculated using the isentropic efficiency (η_{is}):

$$h_{\text{out}} = \frac{h_{\text{out,is}} - h_{\text{in}}}{\eta_{\text{is}}} + h_{\text{in}} \tag{3.40}$$

The electric power consumption can then be derived from the mechanical efficiency of the compressor:

$$W_{\text{elec}} = \frac{\dot{m}_{\text{ref}}(h_{\text{out}} - h_{\text{in}})}{\eta_{\text{mech}}} \tag{3.41}$$

The mechanical efficiency, η_{mech} is assumed to be 0.9670.

3.4. REFERENCE BUILDING

The slurry produced in the system is used to cool down the room temperature of a space with about 144 m^2 as shown in Fig. 3.14.

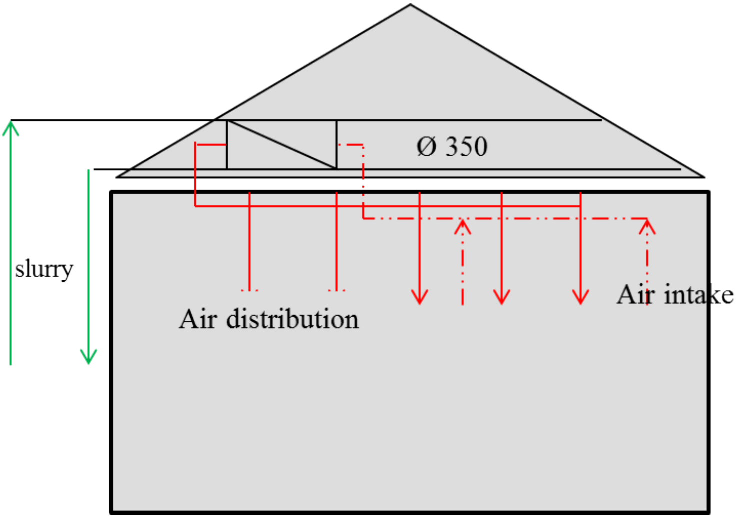

Figure 3.14: Installation diagram showing the reference building which makes use of TBAB hydrate slurry as a distribution medium for the air conditioning system. The air cooler is located in the air-duct with a diameter of 350 mm. It also illustrates how the air is circulated in the room and through the air duct.

The air cooler is installed in the air feed duct to the conditioned space. The diameter of the duct is 0.35 m. The high temperature room air is forced to flow into the duct by a fan and exchanges heat with the slurry flow which circulates through the air cooler. The low temperature air is circulated back to the duct and distributed into the room. In this way, the room is cooled.The hydrate slurry, which has been produced during the night and stored in the storage vessel, is circulated to the air cooler making use of pump 2 (see Fig. 3.2). In the cooler, the slurry partially melts after which the slurry returns to the storage vessel.

3.5. RESULTS

3.5.1. WATER EXPERIMENT

Water experiments are firstly done for testing and comparison purposes. Results are obtained for one day in October 2016 from 00:00:00 to 23:59:50.

AIR-COOLER SIDE

The pump 2 status indicates whether the air-cooler is working or not. Fig. 3.15 shows the speed of pump 2 along with the mass flow in the tubes of the air cooler. It indicates that the air cooler only started operating at around 17:00. The mass flow of water is then in the range of 0.4 - 0.85 kg s^{-1}.

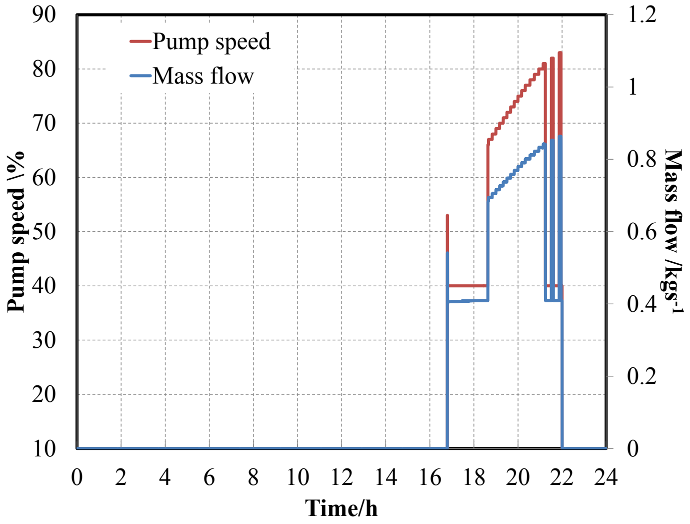

Figure 3.15: Speed of Pump 2 along with the change of water flow in the air cooler. The figure makes clear that the air cooler only operates between 17:00 and 22:00 during this specific day.

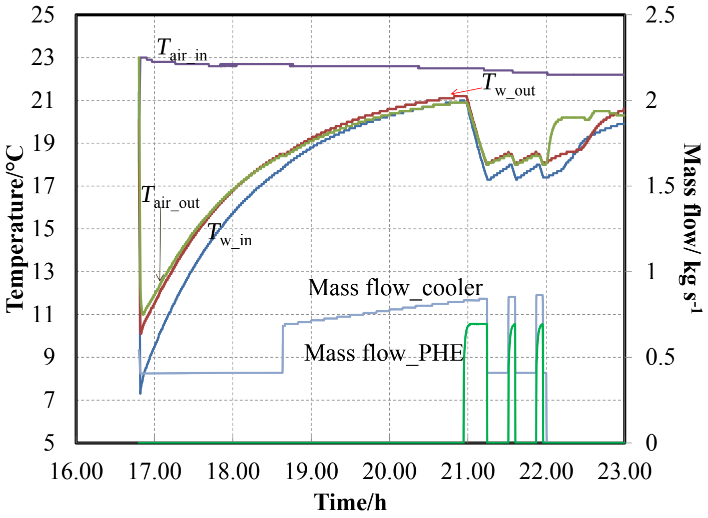

Figure 3.16: Profile of inlet and outlet temperature of air cooler for both water and air side. The water mass flow rate in the air cooler and plate heat exchanger (PHE) are also shown in the figure. The figure makes clear that the PHE (the slurry generator) only starts to operate at around 21:00 in this specific day.

The energy load for the air cooler is obtained from $\dot{Q}_{\text{load}} = \dot{m}_{\text{water}} c_{p\text{water}} (T_{\text{in}} - T_{\text{out}})_{\text{water}}$. The temperature in and out of water as well as the air in and out are measured by temperature sensors shown in the Appendix B. Fig. 3.16 illustrates the temperatures change and the flow rate of water in the cooler and generator during this period. It indicates that when the air-cooler starts working (17:00), the temperature difference of the water passing the air-cooler is about 2.0 K. The temperature before the cooler starts working is not meaningful as the water is stationary in the cooler. It also indicates that the generator pump didn't start working until 21:00 (indicated by the green line). All the heat load is removed only making use of the storage tank, which supplies the cold energy in the first 4 hours before the generator starts working.

Since the air cooler is installed with co-current flow, the logarithmic mean temperature of the air cooler, $\Delta T_{\text{log}_{\text{cooler}}}$, can be derived as

$$\Delta T_{\text{log}_{\text{cooler}}} = \frac{(T_{\text{air}_{\text{in}}} - T_{\text{water}_{\text{in}}}) - (T_{\text{air}_{\text{out}}} - T_{\text{water}_{\text{out}}})}{\log(\frac{T_{\text{air}_{\text{in}}} - T_{\text{water}_{\text{in}}}}{T_{\text{air}_{\text{out}}} - T_{\text{water}_{\text{out}}}})} \tag{3.42}$$

However, the water outlet temperature is higher than the air outlet temperature in some points shown in Fig. 3.16, indicating the co-current installation of the air cooler limits its operation. The arithmetic mean temperature difference ($\Delta T = (T_{\text{air}_{\text{in}}} + T_{\text{air}_{\text{out}}})/2 - (T_{\text{water}_{\text{in}}} + T_{\text{water}_{\text{out}}})/2$) is used instead of the logarithm mean temperature for these points.

The air flow rate can then be derived from the energy balance as: $\dot{Q}_{\text{load}} = \dot{m}_{\text{water}} c_{p_{\text{water}}} dT_{\text{water}} = \dot{m}_{\text{air}} \Delta h_{\text{air}}$. According to the Mollier diagram, initially some water vapor of the humid air will condense on the external surface of the air cooler. Fig. 3.17 shows the cooling load of the air cooler and the derived air flow. The average cooling capacity in this period is 1.61 kW. The air flow is in the range of 700 - 2250 $\text{m}^3\ \text{h}^{-1}$, and changes with the temperature difference of air, dT_{air} (the air fan is speed controlled).

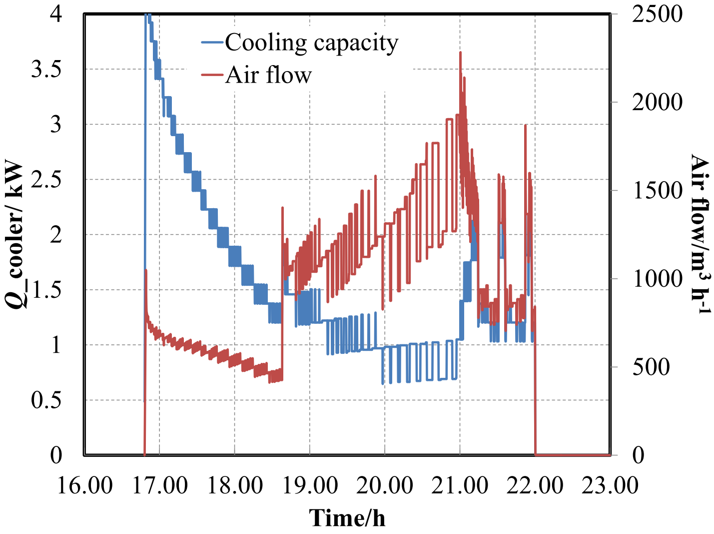

Figure 3.17: Cooling demand and the mass flow rate of air. These data have been derived from the energy balance of the water flow through the air cooler.

For water test, the heat transfer coefficient in the water side is derived making use of the correlation of Gnielinski (1976) [37] for turbulent flow (Re>10^4) and Edwards et al. (1979) [27] for laminar flow (Re<2300). Fig. 3.18 shows the heat transfer coefficient of the air cooler for both water and air side. The Reynolds number of water is in the range of 2600 - 5500, which is in the transition region. It indicates that when the air cooler starts working, the heat transfer coefficient in the water side is in the range of 0.45-0.6 kW m^{-2} K^{-1}. The heat transfer coefficient of the air side is about 0.015 kW m^{-2} K^{-1} from [45]. The air side heat transfer coefficient derived from Schmidt (2010) [90] is also shown for comparison purposes, which gives a higher value (0.025 kW m^{-2} K^{-1}) than that from [45].

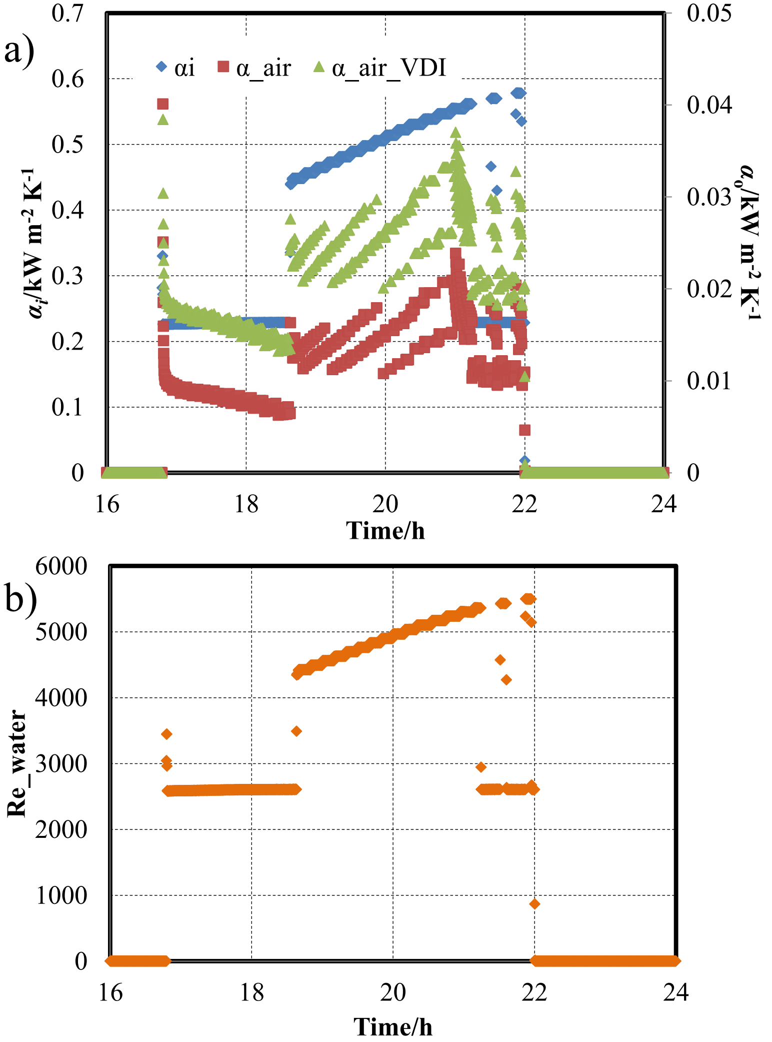

Figure 3.18: a) Heat transfer coefficient of the air cooler for both water and air side; Prediction making use of the methods discussed in the text. b) Experimental Reynolds number of water flow in the air cooler.

The experimental overall heat transfer coefficients are compared with the predicted values derived from Eq. 3.7. Fig. 3.19 indicates that the model from the VDI [90] predicts better than that from [45]. However, both of them under predict the experimental values. It also indicates that the overall heat transfer coefficient of the air cooler increases when the flow velocity increases. However, as the logarithmic mean temperature, $\Delta T_{\log}$, changes along the co-current flow, the experimental overall heat transfer coefficient is not constant.

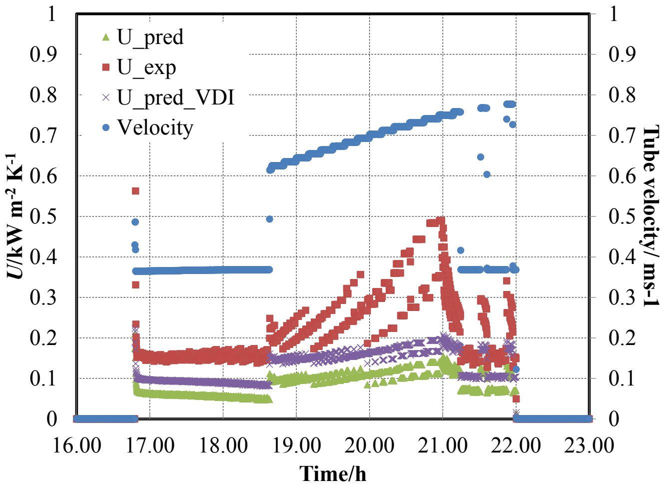

Figure 3.19: Comparison of the experimental and predicted overall heat transfer coefficient for the tube-fin air cooler. The velocity of the water flow in the tubes is also shown.

GENERATION SIDE

The speed of pump 1 (see Fig. 3.2) and the mass flow of water in the generator loop are measured and shown in Fig. 3.20. It indicates that the generator works in the period of 00:00-09:00 and 21:00-24:00. The total energy consumption of the pump can then be derived as $Q_{\text{pump1}} = \int W dt$.

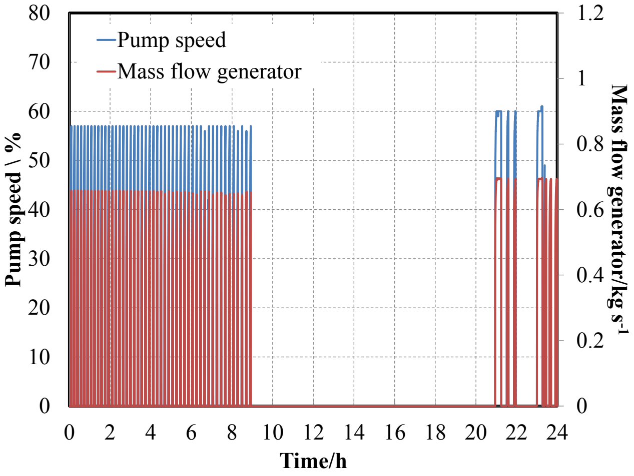

Figure 3.20: Speed of Pump 1 and water mass flow rate in the generator for a period of 24 hours, indicating that working periods for the generator are 00:00-9:00 and 21:00-24:00.

The period from 21:00-24:00 is firstly discussed since Fig. 3.16 indicates that in the first hour of this period there is cooling requirement. Fig. 3.21 shows the inlet and outlet temperatures of the generator for both water and refrigerant side. It shows that the mass flow of water in the generator is about 0.7 kg s^{-1}, while the mass flow of refrigerant is relatively small (0.04 kg s^{-1}). It also indicates that there is always a super-heating of the refrigerant.

The logarithmic mean temperature, $\Delta T_{\log}$, can be derived from the method proposed by Longo and Gasparella (2007) [62] to be about 6 K in the period from 21:00-24:00 when the generator is working.

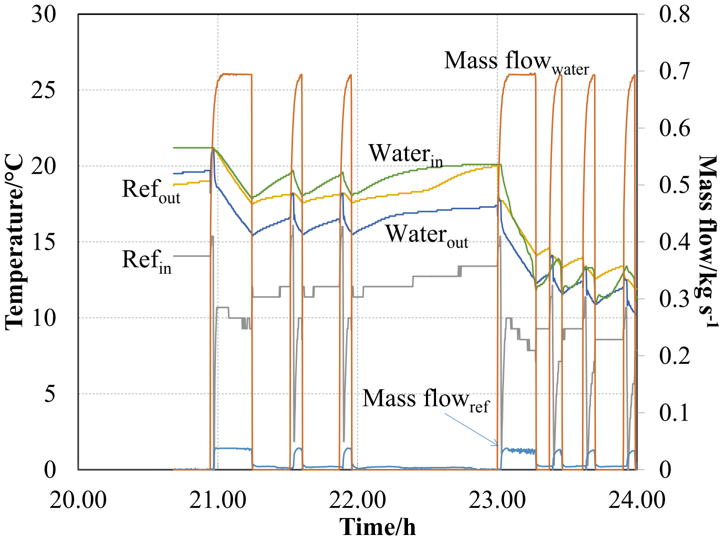

Figure 3.21: Temperature change of water and refrigerant through the generator in the working period 21:00-24:00. The mass flow rates of water and refrigerant are also shown in the figure.

Fig. 3.22 shows the temperature change of water and refrigerant for the generator in the time period of 0:00-1:00. It indicates that in this period, the generator works frequently but only for an extremely short time. This is because there is some refrigerant left in the generator, when the temperature of the storage tank is higher than 12 °C in the night, the generator will start working to lower down the temperature of water in the storage tank. It can also be proved by the extremely low mass flow rate of refrigerant as shown in Fig. 3.22 (0.022 kg s^{-1}). The mass flow of water during this period is about 0.65 kg s^{-1}. This kind of operation only takes place from 0:00-9:00 according to Fig. 3.20, and within 1 hour it repeats 6 times and each time only several minutes.

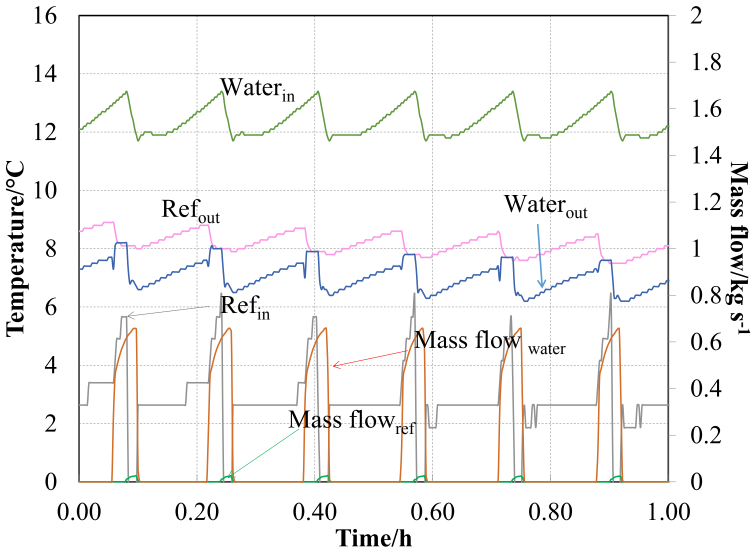

Figure 3.22: Temperature change of water and refrigerant in the generator in the working period 00:00-1:00. The mass flow rate of water and refrigerant are also shown in the figure.

The energy flow in the plate heat exchanger from the water side can be derived from $\dot{Q}_{\mathrm{PHE}} = \dot{m}_{\mathrm{PHE}} c_{p_{\mathrm{water}}} dT_{\mathrm{water}}$. The energy flow obtained from the enthalpy change of refrigerant can be derived as $\dot{Q}_{\mathrm{ref}} = \dot{m}_{\mathrm{ref}} \Delta h_{\mathrm{ref}}$. Fig. 3.23 shows the comparison of the energy flow derived from the slurry side, $\dot{Q}_{\mathrm{PHE}}$, and from the refrigeration side, $\dot{Q}_{\mathrm{ref}}$. Also the superheating at the evaporator outlet is shown. It indicates that there is always a super-heating for the refrigerant. The results indicate that only for the period 21:00 - 24:00, the energy flows match well.

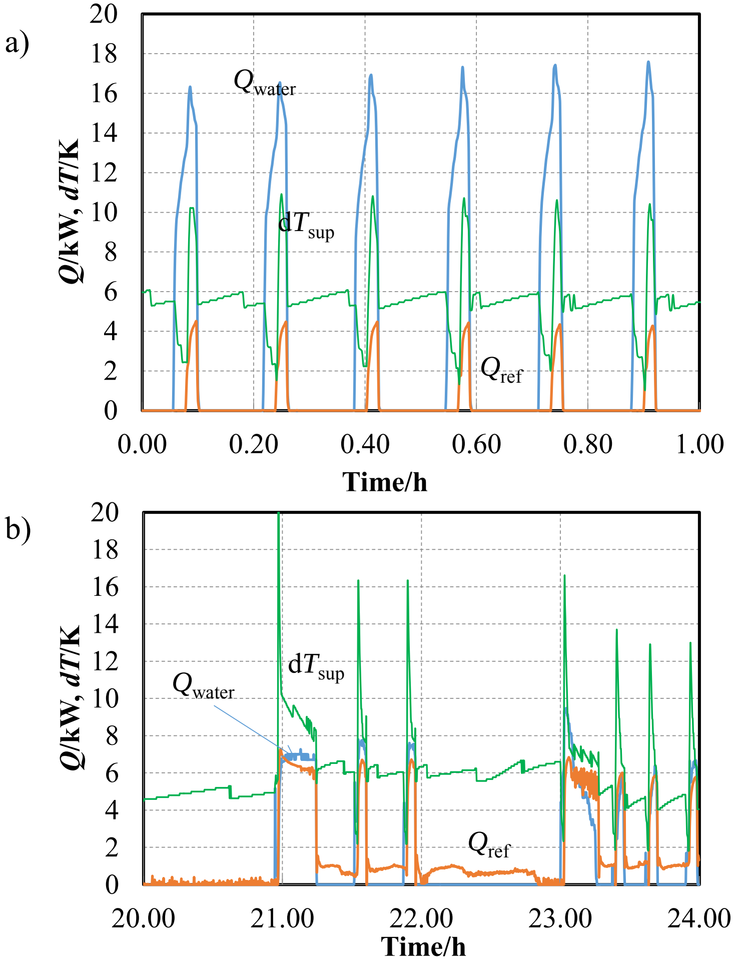

Figure 3.23: Energy flow comparison of generator from both water and refrigeration side a) during period of 00:00-01:00; b) during period of 20:00-24:00. The superheating degree of the refrigerant is also shown in the two periods, indicating that a superheating is always needed in the refrigeration side.

The heat transfer coefficients in the water side and refrigerant side are shown in Fig. 3.24 as well as the Reynolds number of water and refrigerant. It shows that the Reynolds number of water is about 600, while that of refrigerant is about 250. The heat transfer coefficient predicted by Yan and Lin (1999) [120] for the refrigerant side is about 220 W m^{-2} K^{-1}. The value predicted by Cooper (1984)[62] is about 520 W m^{-2} K^{-1}. The water side heat transfer coefficient is about 8500 W m^{-2} K^{-1} according to Eq. (3.23) for water test.

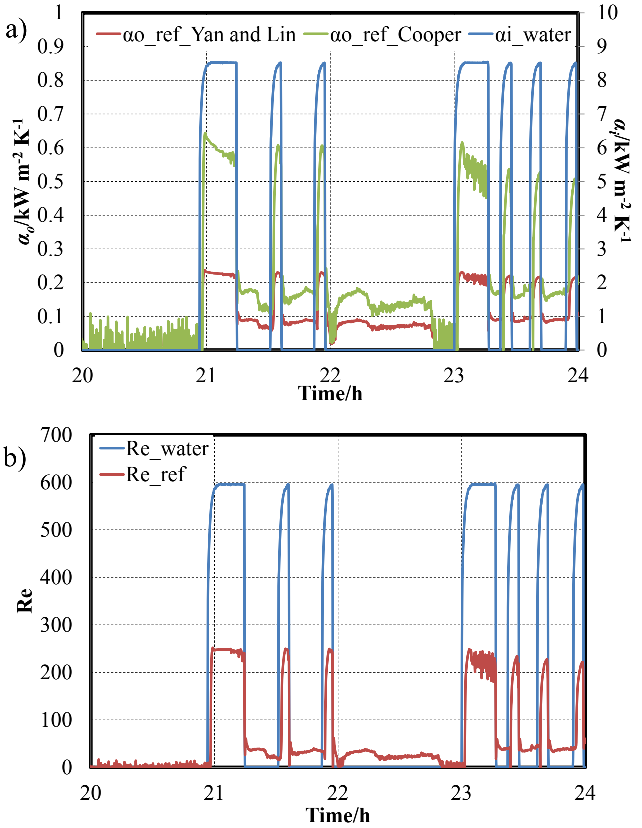

Figure 3.24: a) Heat transfer coefficient of plate heat exchanger for both water and refrigerant side; b) Reynolds number for both water and refrigerant side.

The overall heat transfer coefficient of the plate heat exchanger can be derived as $U_{\mathrm{PHE}_{\mathrm{exp}}} = \dot{Q}_{\mathrm{exp}}/(A\Delta T_{\mathrm{log}})$. Fig. 3.25 shows the comparison of the $U_{\mathrm{PHE}_{\mathrm{exp}}}$ with that calculated from Eq. (3.32) without the addition of crystal layer resistance. It shows that the experimental overall heat transfer coefficient of the generator is about 500 W m^{-2} K^{-1}, with some jumps due to the sudden change of flow. The overall heat transfer coefficient predicted by Yan and Lin (1999) [120] is about 200 W m^{-2} K^{-1}, which under predicts the experimental values. The overall heat transfer coefficient predicted by Cooper (1984) which has been validated by [62] matches better with the experimental values.

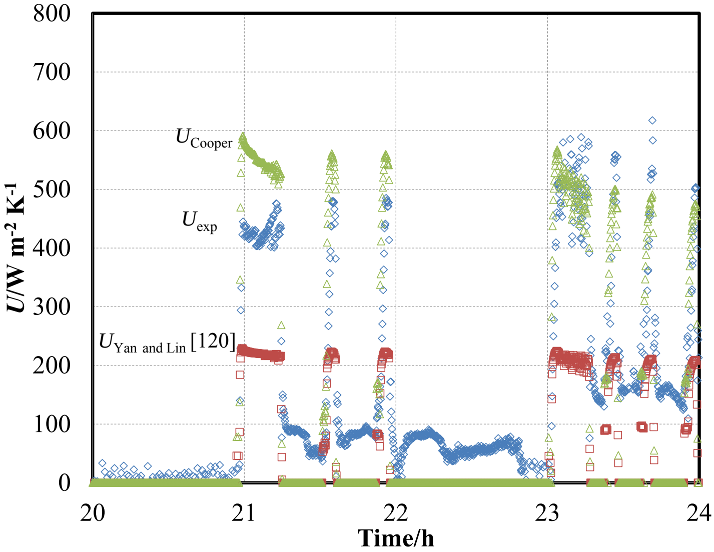

Figure 3.25: Comparison of experimental and predicted overall heat transfer coefficient of the generator. It indicates that the correlation from Cooper predicts better with the experimental value than the other one.

REFRIGERATION SIDE

The power consumption in the refrigeration side is mainly from the compressor, which can be derived from $W_{\text{comp}} = \dot{m}_{\text{comp}} \Delta h_{\text{ref}}$. The temperature and pressure of the refrigerant vapor before and after compressor are measured by sensors. The mass flow is measured by a flow meter. The measured data are shown in Fig. 3.26.

Fig. 3.26a shows that in the period of 0:00-1:00, the compressor works 6 times and each time only for about 2 minutes. Fig. 3.26b indicates that the refrigerant is compressed from 20 °C to 45 °C in the period of 21:00-24:00, with a mass flow of 0.03 kg s^{-1}.

COP OF WATER TEST

COP of the experiment with water as cooling medium can be derived finally as $COP_{\text{exp}} = \frac{\dot{Q}_{\text{load}}}{W_{\text{pump1}} + W_{\text{pump2}} + W_{\text{comp}}}$. The energy load in this specific day can be derived to be 6.25 kWh from Fig. 3.17. The power consumption of the two pumps is negligible. The power consumption of the compressor is derived from Fig. 3.26 as 0.73 kWh for the two working periods. COP is therefore obtained as 8.56 for this specific day.

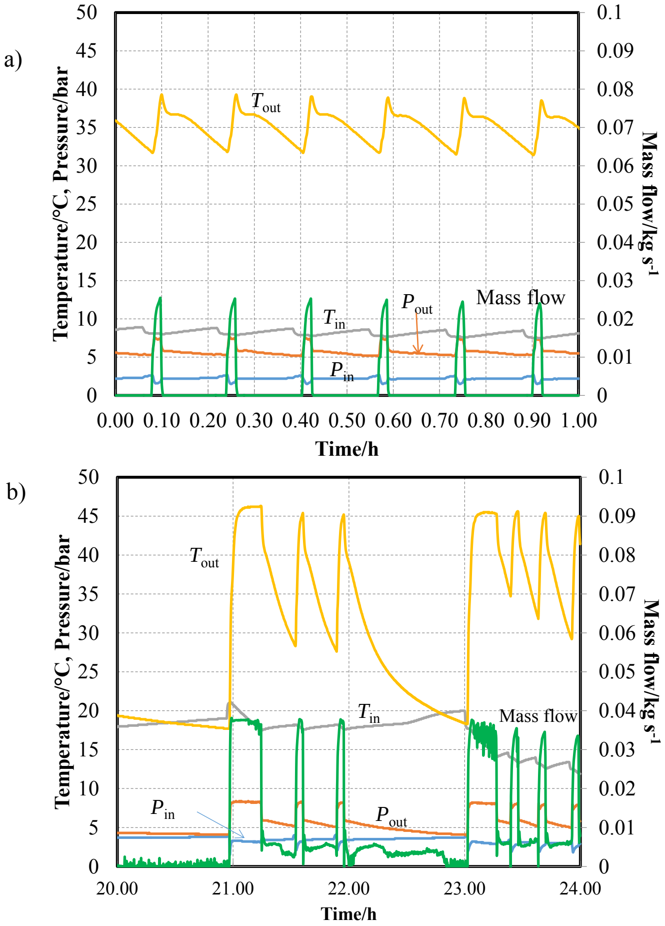

Figure 3.26: Profile of the inlet and outlet temperatures and pressures of compressor in two periods: 0:00-1:00 and 20:00-24:00. The mass flow of refrigerant is also shown in the figures.

3.5.2. HYDRATE GROWTH RATE - MODEL PREDICTION

As the experiments with TBAB hydrate slurry could not be finalized in due time, the hydrate generation discussion below is only based on model predictions.

The inlet air temperature (ambient temperature) and the cooling demand for the model are taken for characteristic data of Netherlands as shown in Fig. 3.27. It indicates that the peak cooling demand of the building during these specific days is about 3 kW. When the temperature is lower than 21 °C, there is no need for air-conditioning in practice. Therefore, the cooling demand is set to be zero when the ambient temperature is lower than 21 °C.

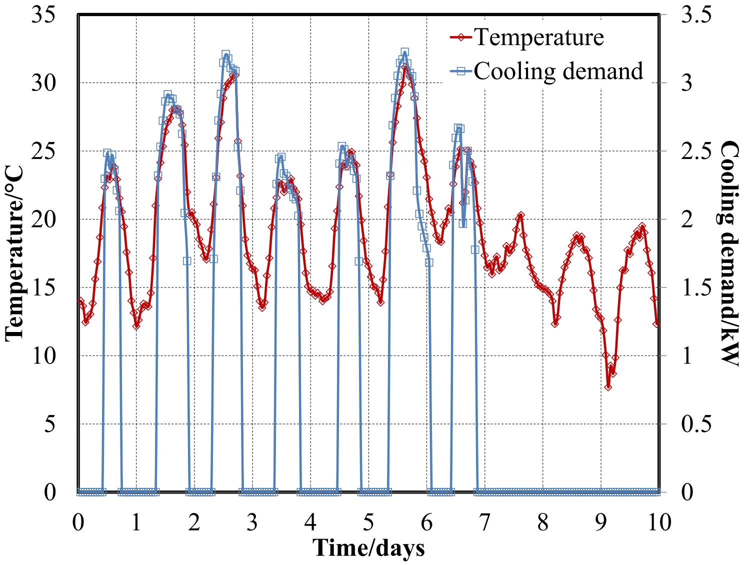

Figure 3.27: Ambient temperature variation with time shows the hot season in the Netherlands. A period of 10 days is shown. The figure also showns the cooling demand corresponds to the ambient temperature.

The flow rate of slurry in the plate heat exchanger is 0.7 kg s^{-1} according to the water test. The outlet temperature of air is set to be 18 °C, since the room temperature is higher, after distribution of the cold air into room, a temperature of 21 °C, which is comfortable for human beings, is expected to be achieved. The flow rate of slurry in the air cooler is also set to be 0.7 kg s^{-1} according to Fig. 3.15. The air flow is changing with the cooling demand as $\dot{m}_{\mathrm{air}} = \dot{Q}/\Delta h_{\mathrm{air}}$. The evaporation temperature of the refrigerant is chosen to be 7.5 °C, since the phase change temperature of TBAB hydrate is 12.5 °C under ambient pressure. The condensation temperature of vapor compressor cycle is set to be 15 K higher than the ambient temperature.

The solid fraction change in the storage tank is shown in Fig. 3.28 with an initial value of 35 wt% in the night mode. It indicates that hydrates are produced during night and consumed in day time (indicated by the decrease of the line).

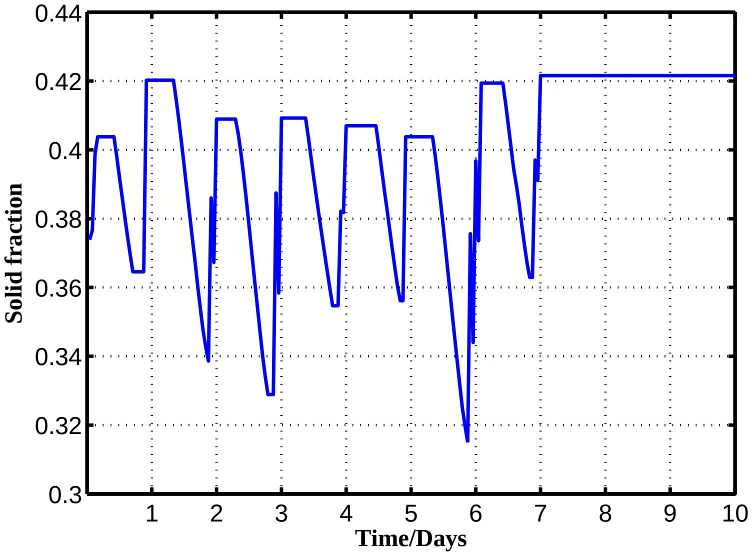

Figure 3.28: Solid fraction change during the period of night mode production.

3.5.3. PERFORMANCE OF TBAB SLURRY SYSTEM AND CONVENTIONAL REFRIGERATION SYSTEM

Coefficient Of the Performance (COP) of the system has been derived for the conventional refrigeration system. Fig. 3.29 shows the power consumption according to the change of cooling demand for the conventional refrigeration system. The water temperature changes from 12 °C to 7 °C. The evaporation temperature is 2 °C. The average COP for the operation time is 3.29 derived from Fig. 3.30.

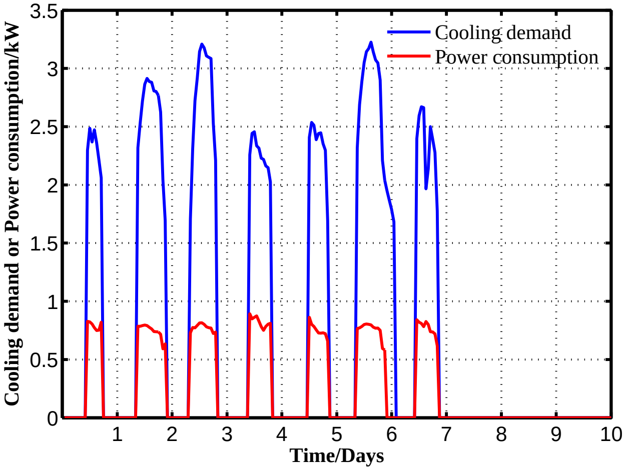

Figure 3.29: Cooling demand and power consumption of the conventional system making use of water as distribution fluid.

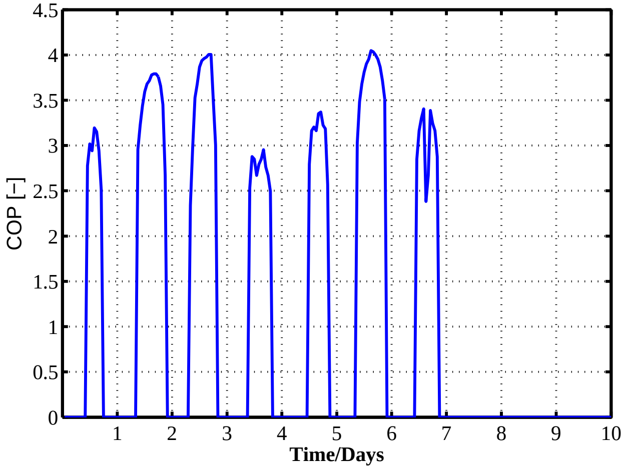

Figure 3.30: COP of the conventional system making use of water as distribution fluid.

The COP of the system which makes use of TBAB hydrate slurry as distribution fluid has been derived for both day and night production (day/night mode). In the day production mode, the hydrate slurry is produced in the day time according to the demand of the cooling. In this working mode, there is no precharge of the storage vessel. Figs. 3.31 and 3.33 show the power consumption change with cooling demand with evaporation temperature of 2 °C and 7.5 °C respectively. The corresponding COP of the system is shown in Figs. 3.32 and 3.34 . The average COP can be derived to be 3.32 with evaporation temperature of 2 °C and 3.97 with evaporation temperature of 7.5 °C.

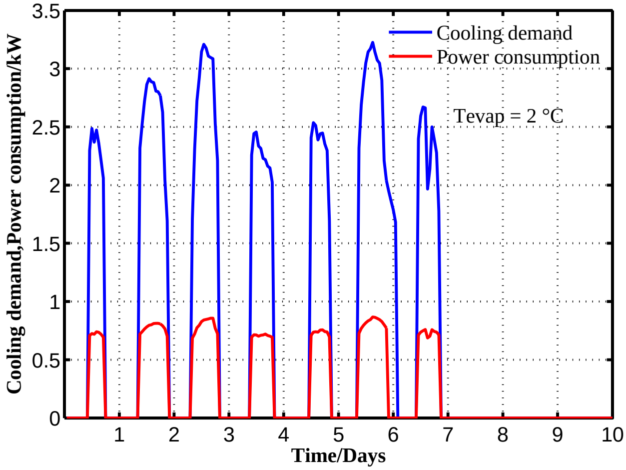

Figure 3.31: Cooling demand and power consumption of the system making use of TBAB slurry as distribution fluid in the day mode with evaporation temperature of 2 °C.

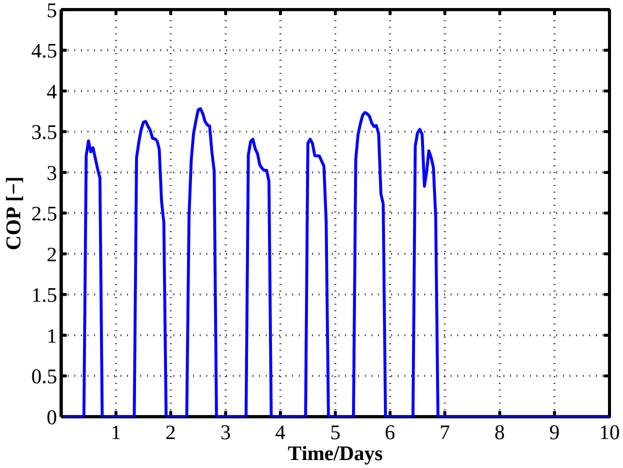

Figure 3.32: COP of the system making use of TBAB slurry as distribution fluid in the day mode with evaporation temperature of 2 °C.

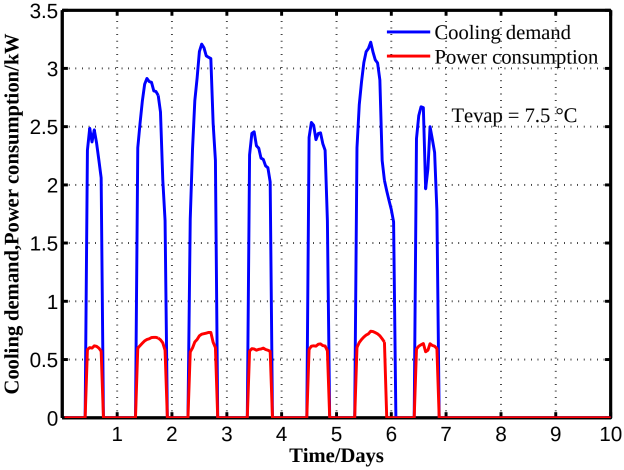

Figure 3.33: Cooling demand and power consumption of the system making use of TBAB slurry as distribution fluid in the day mode with evaporation temperature of 7.5 °C.

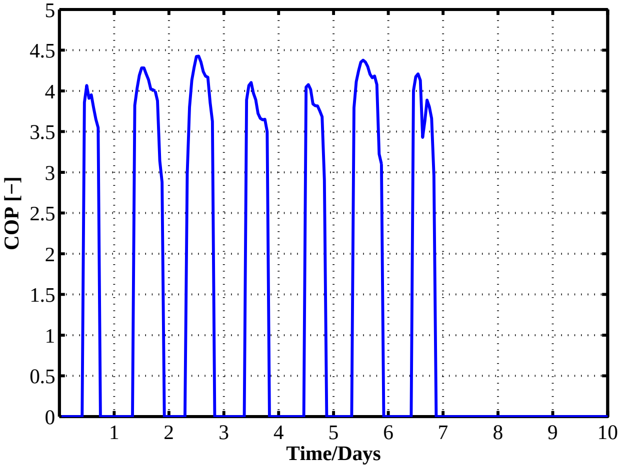

Figure 3.34: COP of the system making use of TBAB slurry as distribution fluid in the day mode with evaporation temperature of 7.5 °C.

The cooling demand and power consumption of the system working in the night mode are shown in Figs. 3.35 and 3.36. In night production mode of the system, the hydrate slurry is produced during the night to charge the storage tank, which is discharged during the day when there is cooling requirement.

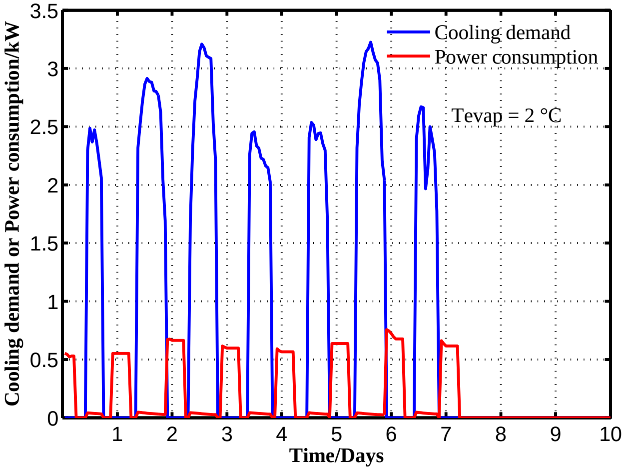

Figure 3.35: Cooling demand and power consumption of the system making use of TBAB slurry as distribution fluid in the night mode with evaporation temperature of 2 °C.

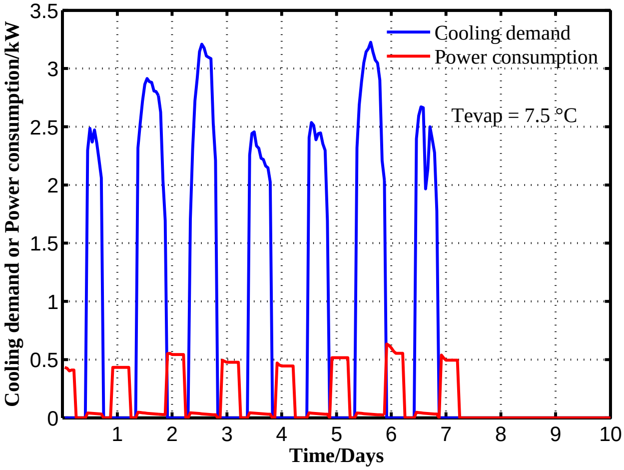

Figure 3.36: Cooling demand and power consumption of the system making use of TBAB slurry as distribution fluid in the night mode with evaporation temperature of 7.5 °C.

Fig. 3.35 shows the change of cooling demand and power consumption with evaporation temperature of 2 °C. Fig. 3.36 shows the change of cooling demand and power consumption with evaporation temperature of 7.5 °C. The average COP of the system for these two cases are 4.66 and 5.71 respectively. It indicates that the efficiency of the system is significantly improved when TBAB hydrate slurry is utilized as cooling medium and especially when the system is combined with a latent heat storage system (41.6% with T_{evap} = 2 °C; 73.5% with T_{evap} = 7.5 °C). The improvement of COP is due to the lower ambient temperature in the night time, which makes lower condensation temperature possible, hence, the energy consumption of the compressor, which is the main power consumption in the primary cycle, is reduced.

The total cooling requirement for these specific 10 days could be obtained as 194.55 kWh. For the conventional system, the power consumption derived from Fig. 3.29 is 59.13 kWh, while that for the TBAB system with storage is 34.07 kWh, which means 25.06 kWh energy is saved totally by using this slurry system. For Europe, the CO_2 emission due to the consumption of fuel for electricity was, in 2013, in average 558 g kWh^{-1}. The CO_2 emission is proportional to the energy consumption. Therefore, by using TBAB hydrate slurry system in air conditioning systems, 73.5% CO_2 emission could be saved.

3.6. CONCLUSIONS

A plate heat exchanger is used to produce TBAB hydrate slurry. The TBAB slurry is utilized as distribution fluid for an air conditioning system of a 144 m^2 space. With a cold storage tank of 300 L, a cooling capacity of 3 kW can be obtained when slurry is produced during the night time.

The COP of the system with TBAB hydrate slurry is significantly improved (up to 73.5%) especially when a latent heat thermal storage system is used. Due to the application of TBAB hydrate slurry, a similar percentage of CO_2 emissions can be prevented.

III

CO_2 HYDRATE SLURRY

4

CO_2 HYDRATE SLURRY PRODUCTION IN A FLUIDIZED BED HEAT EXCHANGER

Parts of this chapter have been published in Applied Energy **158**, 433-445 (2015) [133].

4.1. INTRODUCTION

In this chapter, CO_2 hydrate slurry investigation will be introduced. Compared with TBAB hydrate, CO_2 hydrate has a higher latent heat (387 kJ kg^{-1}), and the phase change temperature of CO_2 hydrate is in the room temperature range (ca. 7 °C). In addition, CO_2 hydrate is non-toxic in comparison with TBAB hydrate, which means that it can be used for direct contact cooling processes.

Compared with sensible heat storage materials, for example water, CO_2 hydrate slurry has a higher energy storage density. According to de Sera et al. (2014) [17] the storage volume for a capacity of 10^6 J are 16 m^3 for water and 0.6 m^3 for CO_2 hydrate slurry with 30% solids concentration. Therefore, it is possible to store the same amount of energy with a much smaller volume which could result in lower investment costs. The cost reduction will be limited by the requirement of operating the storage vessel at higher pressure level. Moreover, isothermal heat storage and heat recovery minimize the energy losses (Tamme et al., 2008 [108]). A respectful number of cold storage applications are reported in literature with the application temperature below 10°C and above 0 °C (Oró et al., 2012 [80]).

Criteria to select a suitable latent heat storage material for a particular application are (Agyenim et al., 2010 [4]; Sharma et al., 2009 [96]): a suitable phase change temperature in the desired operation range, a high latent heat value, a high thermal conductivity value, good cycling stability and small supercooling during solidification. Farid et al. (2004) [31] reviewed several TES with phase change materials (PCMs) and their applications. These authors highlighted the problems of supercooling, phase separation and thermal instability. The use of a fluidized bed heat exchanger reduces the required supercooling for phase change practically to 0 K. Meewisse (2003) [71] and Pronk (2006) [84] have developed a mathematical model of fluidized bed slurry generators. They derived the crystal growth rate and from it the solids concentration increase as the flow passes the heat exchanger. They further concluded that the temperature gradients are very low within the fluidized bed.

The main objective of this chapter is to predict and experimentally validate the transient performance of a fluidized bed LHTS system, combined with a CO_2 hydrate slurry storage system for cooling purposes. Continuous charging and discharging operation of the LHTS system can take place independently from each other. Further objectives are: the evaluation of CO_2 hydrate slurry as candidate PCM in the proposed application range (0 to 10 °C), the integration of the LHTS system with the fluctuation of the cooling demand, and investigation of the impact of operating conditions on system performance.

4.2. CO2 HYDRATE SLURRY AS CANDIDATE PCM

CO_2 hydrate slurry is considered to be one of the most promising PCMs for cold storage in space cooling systems. It has a melting enthalpy which is even larger than the melting enthalpy of ice and the phase change takes place at temperatures above 0 °C, mostly in the range 7-8 °C, which matches the operating temperatures in space cooling applications. The system further only uses CO_2 and H_2O, natural fluids with limited environmental impact.

The properties of CO_2 hydrate slurry have been reviewed by de Sera et al. (2014) [17]. The most relevant properties are summarized here.

4.2.1. PHASE EQUILIBRIUM OF CO2+H2O AROUND HYDRATE FORMATION CONDITIONS

Phase equilibrium data of carbon dioxide hydrate have been reported by many researchers : Vlahakis et al. (1972) [113], Adisasmito et al. (1991) [3], Ohgaki et al. (1993) [79], Ng and Robinson (1985) [76], Wendland et al. (1999) [117], Yang et al. (2000) [123], Mooijer van den Heuvel et al. (2001) [74], Yokozeki (2004) [124], Sabil (2009) [87] and Lirio and Pessoa (2013) [60]. These researchers show that the CO_2 hydrate formation temperature at 30 bar is approximately 7 °C. In the present study, Sabil (2009)'s results have been adopted since their data reproduces the present experimental data most accurately. Eq. (4.1) gives the equilibrium temperature line as derived from Sabil's data.

$$T_{\mathrm{eq}} = -6.80048 + 0.70379P - 0.00745P^2 \tag{4.1}$$

with the saturation temperature, T_{eq}, expressed in °C and the pressure, P, expressed in bar.

4.2.2. DENSITY OF CO2 HYDRATE SLURRY

The density of a hydrate suspension in a solution can be calculated as given in Eq. (4.2).

$$\rho_s = \frac{\rho_{\mathrm{sol}}\rho_H}{\rho_{\mathrm{sol}} w_H + \rho_H(1 - w_H)} \tag{4.2}$$

The density of the CO_2 solution in water can be obtained with the relation proposed by Duan et al. (2008) [24] in Eq. (4.3).

$$\rho_{\mathrm{sol}} = \frac{x_{\mathrm{H_2}O} M_{\mathrm{H_2}O} + x_{\mathrm{CO_2}} M_{\mathrm{CO_2}}}{\frac{x_{\mathrm{H_2}O} M_{\mathrm{H_2}O}}{\rho_{\mathrm{H_2}O}} + x_{\mathrm{CO_2}}(1 + A_1 + A_2 P)} \tag{4.3}$$

P is expressed in MPa. A_1 and A_2 are constants listed in Table 4.1 and A_i with $i = 1,2$ is given by Eq. (4.4).

$$A_i = A_{i1}T^2 + A_{i2}T + A_{i3} + A_{i4}T^{-1} + A_{i5}T^{-2} \tag{4.4}$$

Table 4.1: Constants in Eq. (4.4).

j	A_{1j}	A_{2j}
1	$0.38384020 \times 10^{-3}$	$-0.57709332 \times 10^{-5}$
2	$-0.55953850 \times 10^{0}$	$0.82764653 \times 10^{-2}$
3	0.30429268×10^{3}	$-0.43813556 \times 10^{1}$
4	$-0.72044305 \times 10^{5}$	0.10144907×10^{4}
5	0.63003388×10^{7}	$-0.86777045 \times 10^{5}$

The hydrate density is related with the hydration number. Teng et al. (1996) [109] proposed an equation to calculate this density.

$$\rho_H = \frac{46 M_{CO_2}}{N_0 a^3} \left(0.409 + \frac{x^H_{CO_2}}{1 - x^H_{CO_2}} \right) \tag{4.5}$$

where M_{CO_2} is the molar mass of CO_2 in kg mol^{-1}, N_0 is the Avogadro constant in molecules/kmol ($6.02214129 \times 10^{26}$), and $a = 12 \times 10^{-10}$ is the lattice constant. CO_2 clathrate hydrates, or simply CO_2 hydrates are CO_2 guest molecules trapped inside “cages”, often referred to as cavities, of hydrogen bonded water molecules, resulting in crystalline solids which look a lot like ice. If the cages, or the cavities, in a hydrate structure are all filled with guest molecules, the hydrate is called stoichiometric. In practice however, this is not often the case. CO_2 forms type I hydrates which consist of 46 water molecules. The occupancy of CO_2 hydrate, which indicates how many cages are occupied with CO_2 molecules, does not often exceed 75% in case of hydrate structure Type I. The chemical formula for CO_2 hydrate is “$(x+y)CO_2 - 46H_2O$”, where $x (\leqq 2)$ and $y (\leqq 6)$ represent the numbers of the occupied 5^{12} (small) and $5^{12}6^2$ (large) cages, respectively. If all of the cages are occupied, then $x + y = 8$, leading to the common expression of “$8CO_2$–$46H_2O$” or “CO_2–$5.75H_2O$” for CO_2 hydrate. However, since the ratio between small and large cages is 2-6, the practical expression for CO_2 hydrate should be “$6CO_2$–$46H_2O$” of “CO_2–$7.67H_2O$”, i.e. CO_2 hydrate is a non-stoichiometric compound. The number of water molecules per CO_2 molecule, 5.75 in the stoichiometric case, is known as the “hydration number”. Lirio and Pessoa (2013) [60] have shown that, depending on the formation conditions, the hydration numbers can vary between 6.0 and 8.3. The density of CO_2 hydrate is strongly influenced by the CO_2 occupancy in the cavities of the hydrate crystals as shown in Eq. (4.5). In this study it is assumed that 70% of the hydrate cavities are occupied by CO_2 ($x^H_{CO_2} = 0.110$; $w^H_{CO_2} = 0.232$) resulting in a hydration number of 8.06 and a hydrate density of ρ_H=1036 kg m^{-3} when Eq. (4.5) is applied which is consistent with Sari et al. (2008) [89]. With different occupancy and thus hydration number, the density of the produced hydrates will also differ. This number is highly sensitive to the experimental conditions. For instance, Teng et al. (1996) [109] report ρ_H=1049 kg m^{-3} if only the large cavities are occupied (i.e. $x^H_{CO_2} = 0.115$; $w^H_{CO_2} = 0.241$).

4.2.3. VISCOSITY OF CO_2 HYDRATE SLURRY

The viscosity of CO_2 hydrate slurry is predicted from Eq. (4.6) which has been successfully applied by Kauffeld et al. (1999) [51] for the prediction of the viscosity of ice slurries, (Thomas, 1965 [110]).

$$\mu_s = \mu_{\text{sol}}(1 + 2.5\phi_H + 10.05\phi_H^2 + 0.00273\exp(16.6\phi_H)) \tag{4.6}$$

with ϕ_H the volume fraction of hydrates. The viscosity of the CO_2 water solution, μ_{sol} , depends both on pressure and temperature and has been obtained by assuming a linear dependence with the CO_2 concentration.

$$\mu_{\text{sol}} = \mu_{\text{H}_2\text{O}}(1 - w_{\text{CO}_2}) + \mu_{\text{CO}_2} w_{\text{CO}_2} \tag{4.7}$$

Where μ_{CO_2} is the viscosity of liquid CO_2 and pure fluid properties have been obtained from REFPROP (Lemmon et al., 2013 [59]).

4.2.4. ENTHALPY OF CO_2 HYDRATE SLURRY

Table 4.2 shows the melting enthalpy of CO_2 hydrate crystals reported by several authors. It is taken as 387.2 kJ kg^{-1} for n = 8.06. Previously, Fournaison et al. (2004) [34] have reported a melting enthalpy of 507 kJ kg^{-1} but the studies listed in Table 4.2 indicate a much lower value. The enthalpy of hydrate slurry is then derived considering it as a mixture of hydrates and solution.

$$h_s = w_H h_H + (1 - w_H) h_{\text{sol}} \tag{4.8}$$

The enthalpy of the solution has been based on the assumption of a linear dependency of the specific heat of the solution with the CO_2 concentration in the solution.

$$h_{\text{sol}} = [c_{p_{H_2O}}(1 - w_{\text{CO}_2}) + c_{p_{\text{CO}_2}} w_{\text{CO}_2}](T_{\text{sol}} - T_{\text{reference}}) \tag{4.9}$$

where $c_{p_{CO_2}}$ is the specific heat of liquid CO_2 and $T_{\text{reference}}$ is the reference temperature which has been taken as 279.15 K. Further, where w_H is the solid (hydrates) mass fraction in the slurry and can be obtained from Eq. (4.10) when the solution and slurry densities are known.

$$w_H = \frac{\rho_H(\rho_s - \rho_{\text{sol}})}{\rho_s(\rho_H - \rho_{\text{sol}})} \tag{4.10}$$

Table 4.2: Enthalpy of solid-liquid phase change of CO_2 hydrate in literature and the corresponding hydration number, n.

Source	T/°C	$\triangle h_H$ / kJ kg^{-1}	n
Udachin et al. (2001) [112]	2.85	398.5	6.2
Bozzo et al. (1975) [11]	0.05	336.3	7.3
Vlahakis et al. (1972) [113]	0.05	341.5	7.3
Yoon et al. (2003) [125]	0.05	370.1	6.21
Sabil (2009) [87]	0.45	386.7	8.25
Sabil (2009) [87]	8.25	389.5	5.98
Lirio and Pessoa (2013) [60]	2.15	380.2	7.9
Lirio and Pessoa (2013) [60]	4.05	384.9	7.4
Lirio and Pessoa (2013) [60]	6.05	387.6	6.9
Lirio and Pessoa (2013) [60]	6.75	387.6	6.9

4.2.5. DIFFUSION COEFFICIENT OF CO_2 IN WATER

The diffusion coefficient of CO_2 in water has been obtained with the relation proposed by Lu et al. (2013) [63], given in Eq. (4.11) , which reveals a temperature dependence.

$$D = \exp\left(-\left[\frac{716.748}{T-126.9}\right]-15.9\right) \tag{4.11}$$

The temperature in this equation is expressed in K.

4.2.6. OTHER CO_2 HYDRATE PROPERTIES

The specific heat of CO_2 hydrates has been taken from Youssef et al. (2014) [127] to be 2.1 kJ kg^{-1} K^{-1} for the relevant temperature range.

The thermal conductivity of a solid hydrate has been reported by Sloan and Koh (2008) [102] to be in the range 0.50-0.58 W m^{-1} K^{-1}, closer to the thermal conductivity of liquid water than of ice. The thermal conductivity of CO_2 hydrates has been taken as 0.54 W m^{-1}K^{-1} for the relevant temperature range.

4.3. EXPERIMENTAL APPARATUS AND PROCEDURE

4.3.1. SYSTEM DESCRIPTION

A simplified process flow diagram of the fluidized bed CO_2 hydrate slurry cold storage system is illustrated in Fig. 4.1. The PID of the set-up is reproduced in Appendix C. The main components are the fluidized bed slurry generator (FBHE), the LHTS system and an auxiliary refrigeration cycle which provides the cooling for the slurry generator using refrigerant R134a. Heat is removed from the pressurized CO_2-water solution by the refrigerant which flows as a falling film along the inner tube of the annular space around the fluidized bed tube. The concentration of hydrate crystals is increased by circulating the outlet of the fluidized bed to the cold storage vessel and recirculating the suspension to the inlet of the fluidized bed.

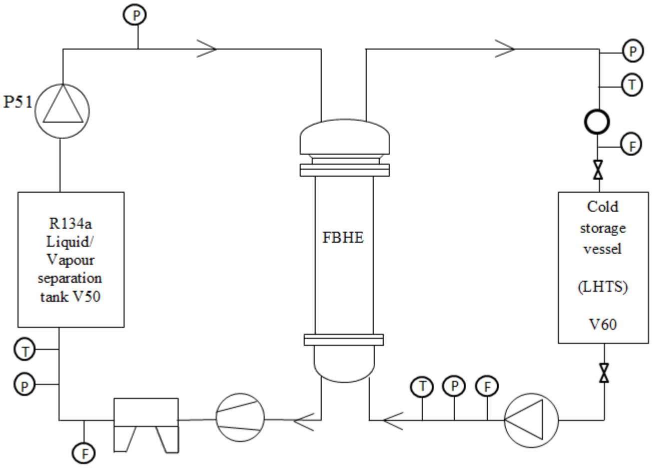

Figure 4.1: Process flow diagram of the system, containing a fluidized bed CO_2-hydrate generator and a CO_2-hydrate slurry cold storage vessel (V60).

The operation depends on the cooling demand and the circulation through the fluidized bed. Hence, the cooling demand and the range of hydrate concentrations in the storage vessel are inputs of the system. Furthermore, the efficiency of the refrigeration system, and the cooling of the condenser of the refrigeration system (air cooled) depend on the ambient temperature. Therefore, the ambient temperature is likewise an input of the system. The output of the system is the energy needed by the system as a function of LHTS system size.

4.3.2. FLUIDIZED BED BASED CO_2 HYDRATE SLURRY GENERATOR

A single tube-in-tube fluidized bed heat exchanger with an internal diameter of 0.0828 m and a total column/tube height of 1.9 m is used, see Fig. 4.2. The tubes are made of stainless steel, the inner tube (or fluidized column) has a wall thickness of 0.00305 m. The CO_2–water solution enters the column from the bottom. The R134a flows over the column from the top, forming a falling film on the outside of the tube. Here it evaporates, extracting heat from the column's surface. This results in the formation of CO_2 hydrate crystals on the inner wall of the fluidized bed tube/column. These crystals are removed continuously by the inert particles which are fluidized inside of the column by the solution flow.

The inert particles are made of stainless steel and have a cylindrical shape

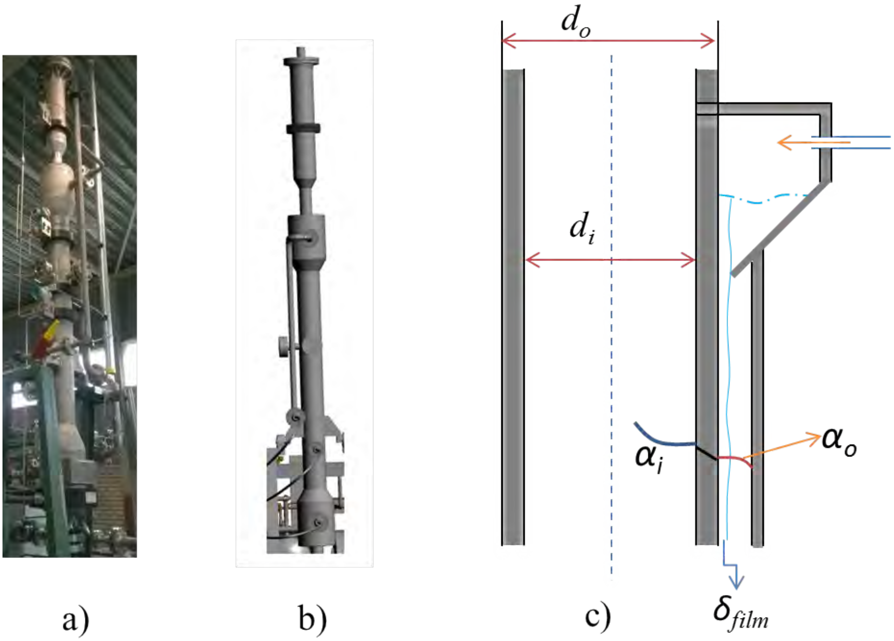

Figure 4.2: Fluidized bed heat exchanger as part of the system. a) a picture of the of the set-up showing the fluidized bed heat exchanger before it was insulated; b) a 3-D drawing of the heat exchanger; c) sketch illustrating the heat transfer resistances.

with an equal height and equivalent diameter of 0.002 m. The particles are not circulated but stay inside the column; the fluidized bed is thus stationary. The crystals are approximately 20 (2 mm vs 100 µm) times smaller than the steel particles of the fluidized bed and about 60000 times lighter than the steel particles. Separation can easily take place by gravity in the section above the fluidized bed heat exchanger. As also visible in Fig. 4.2, this section has a significantly larger cross section so that the velocity is significantly reduced. The resulting slurry leaves the column/inner tube from the top and is stored in the slurry storage vessel (V60 in Fig. 4.1), see Fig. 4.3.

A circulation pump is used to pump the slurry through the column and to fluidize the steel particles. A controller has been added to this pump to ensure no solid particles leave the column with the slurry at the top. Another pump (P51 in Fig. 4.1) is added to the primary refrigeration cycle and circulates the refrigerant between a low pressure separator (V50 in Fig. 4.1) and the top of the fluidized bed annulus. This is necessary because the liquid refrigerant needs to be delivered at the top of the heat exchanger (falling film evaporation). The circulation ratio of

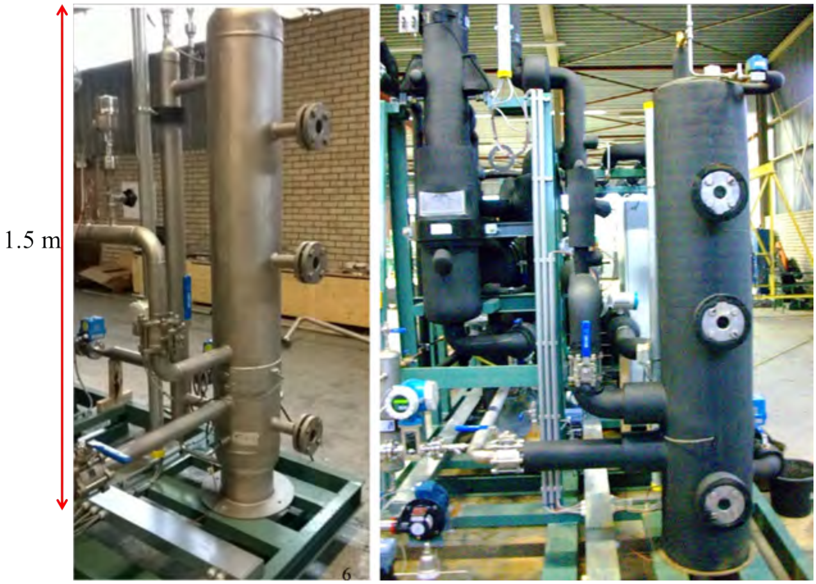

Figure 4.3: Picture of the cold storage vessel before (left) and after (right) being insulated showing the position of the three sight glasses.

this liquid overfeed system is extremely large (about 48) guaranteeing complete wetting of the fluidized bed heat exchanger wall.

4.3.3. LHTS SYSTEM

The CO_2 hydrate slurry cold storage system consists mainly of a vertically oriented cylindrical cold storage pressure vessel with a length of 1.5 m and a diameter of 0.273 m. The liquid level in the vessel can be adjusted, allowing for a volume of CO_2 gas above the slurry. Formation of hydrates consumes CO_2 while dissociation increases the volume of free CO_2 in the system. The total volume is 0.080 m^3 but the maximum slurry volume in the storage tank is 0.070 m^3. Three sight glasses allow visualization of the slurry inside the vessel. Fig. 4.3 indicates the position of the sight glasses along the height of the storage vessel. Fig. 4.3 also shows the inlet and outlet connections of the vessel. These lines are, through internal elbows, respectively connected to the top and the bottom of the vessel. The concentration of the slurry at inlet and outlet are determined from the density of the slurry which is measured by two Coriolis mass flow meters (Siemens Sitrans FCS400 flow meters, accuracy ± 5 kg m^{-3}) in both lines.

During the present experiments there was no melting heat exchanger connected to the vessel. For modelling purposes it is assumed that an additional pump circulates the slurry between storage and melting heat exchanger. The conditions at the pump inlet are assumed the same as the conditions at the outlet of the storage. The flow returning from the melting heat exchanger is assumed to be ideally mixed with the inlet flow of the storage tank before entering the tank.

4.3.4. EXPERIMENTAL PROCEDURE

The system is first brought to equilibrium conditions by adding CO_2 until the desired pressure inside the system (30 or 35 bar) is attained. When CO_2 gas is being added to the system (open system), the density measurement is disturbed by CO_2 gas bubbles which pass the flow meters, resulting in unreliable measurements. Therefore, for some of the experiments, no additional CO_2 is added after the desired system pressure has been achieved (closed system). More reliable data can then be collected for the solution / slurry density. In addition, to ensure a well mixed CO_2 water solution, a static mixer (Fig. 4.4) is installed directly after the CO_2 feeding point.

Figure 4.4: Static mixer tubes of pilot plant. The red cycle shows that there are four tubes connected in series. The static mixer is needed to ensure a well-mixed water-CO_2 solution.

The cooling temperature, *i.e.* the evaporation temperature, is controlled through the suction pressure of the compressor of the primary refrigeration cycle. This evaporation temperature is lowered in small steps and kept constant for a considerable amount of time, at least over one hour, until the density has stabilized and reached its maximum attainable value for that particular evaporation temperature. In this way the hydrate production rate as a function of the driving temperature difference (hydrate formation saturation temperature – evaporation temperature) can be measured.

4.4. MATHEMATICAL MODEL OF THE FLUIDIZED BED CO_2 SLURRY GENERATOR

The model of hydrate growth rate in the fluidized bed generator is based on a control volume method. The fluidized bed generator is subdivided into a large number of control volumes from bottom to top for each time step. Mass and energy conservation equations have been derived for each control volume. Since in and outlet conditions of the fluidized bed are at approximately the same temperature and are practically at equilibrium conditions, it is assumed that the vapour layer above the storage vessel remains at equilibrium conditions. Notice that when CO_2 is added it is added in the feed line to the fluidized bed heat exchanger and that this line includes a static mixer.

The mass of hydrates in a control volume is the sum of the entering hydrates and hydrates produced in the control volume as given in Eqs. (4.12) and (4.13).

$$\dot{m}_H^{j+1} + \dot{m}_{\mathrm{sol}}^{j+1} = \dot{m}_H^{j} + \dot{m}_{\mathrm{sol}}^{j} \tag{4.12}$$

with

$$\dot{m}_H^{j+1} = \dot{m}_H^{j} + G_{\mathrm{lin}}^{j} \rho_H \pi d_i dz \tag{4.13}$$

where G_{lin}^{j} is the hydrate linear growth rate in the corresponding control volume and dz is the axial length of the control volume.

The growth rate of crystals at the wall of the heat exchanger is determined by mass transfer. Englezos et al. (1987) [28] proposed a growth model for gas hydrate formation which considers the hydrate formation process to have two consecutive steps: diffusion of the dissolved gas from the bulk of the solution to the crystal-liquid interface, followed by gas adsorption of the gas molecules into the cavities that are formed by water molecules. Since there is no accumulation in the diffusion layer around the particles, the authors consider diffusion rate and adsorption rate to be equal. Skovborg and Rasmussen (1994) [101] have concluded that all resistance to mass transfer during hydrate formation lays in the diffusion of the dissolved gas. For this reason, the driving force for this mass transfer is the concentration difference between the bulk CO_2-water solution and the equilibrium concentration at wall temperature. To determine the crystal growth rate, G_{lin}, the growth model of Pronk (2006) [84] is used, Eq. (4.14).

$$G_{\mathrm{lin}} = \frac{k}{x_{CO_2}} \frac{\rho_{\mathrm{sol}}}{\rho_H} \frac{M_{H_2O}}{M_{\mathrm{sol}}} \frac{dx^*}{dT} \left(T_w - T^*(x_{CO_2})\right) \tag{4.14}$$

where x_{CO_2} is the molar concentration of CO_2 in the bulk solution which has been obtained from Diamond and Akinfiev (2003) [18] as Eq. (4.15).

$$\begin{aligned} x_{CO_2} = 1.570415 + 7.887505 \times 10^{-2} T + 4.734722 \times 10^{-3} T^2 + \\ 4.56477 \times 10^{-4} T^3 - 3.79608 \times 10^{-4} T^4 \end{aligned} \tag{4.15}$$

with T the temperature in °C and the solubility of CO_2 in mole percent. Empirical Eq. (4.15) applies for the solubility along the coexistence curve of CO_2-clathrate-hydrate+aqueous liquid+CO_2-rich vapor. The mass transfer coefficient, k, has been predicted making use of the correlation specifically proposed for wall-to-fluid mass transfer in liquid-solid fluidized beds by Schmidt et al. (1999)[91] given in Eq. (4.16).

$$k = \frac{D}{d_{\mathrm{ps}}}[0.14\mathrm{Re}_s^{0.33}\mathrm{Sc}_s^{0.33} + 0.13(1-\epsilon)(\epsilon-\epsilon_{\mathrm{pb}})\mathrm{Re}_s^{-0.33}\mathrm{Sc}_s^{0.33}\mathrm{Ar}_s^{0.67}] \tag{4.16}$$

Alternatively, the analogy between heat and mass transfer has been used to determine the mass transfer coefficient. Haid's (1997) [40] correlation for the prediction of heat transfer between wall and liquid in liquid-solid fluidized beds has been taken as basis for the analogy. The mass transfer coefficient, k, is then obtained from Eq. (4.17).

$$k = \mathrm{Sh}\frac{D}{d_{\mathrm{ps}}}\frac{1-\epsilon}{\epsilon} \tag{4.17}$$

The wall temperature in Eq. (4.14) is derived from the energy flow through the heat exchanger wall as given in Eq. (4.18).

$$T_{w,i} = T_{\mathrm{sol}} - \frac{U_i A_i (T_s - T_{\mathrm{ref}})}{\alpha_i A_i} \tag{4.18}$$

where U_i is the overall heat transfer coefficient which can be derived from Eq. (4.19).

$$\frac{1}{U_i} = \frac{1}{\alpha_i} + \frac{d_i \ln(\frac{d_o}{d_i})}{2\lambda_w} + \frac{d_o}{d_i}\frac{1}{\alpha_o} \tag{4.19}$$

The heat transfer coefficient inside the fluidized bed is derived from Eq. (4.20).

$$\alpha_i = \mathrm{Nu}_h \frac{\lambda_s}{d_{\mathrm{ps}}}\frac{1-\epsilon}{\epsilon} \tag{4.20}$$

While Nu_h has been obtained making use of a correlation proposed by Haid (1997) [40]. The superficial velocity was around 0.28 m s^{-1} leading to Re_h numbers in the range of 40000 to 80000. The bed porosity was $\epsilon = 0.85$.

$$\mathrm{Nu}_h = 0.0734\mathrm{Re}_h^{0.75}\mathrm{Pr}^{0.63} \tag{4.21}$$

The heat transfer coefficient in the annular space takes place as falling film heat transfer and has been obtained from Schnabel (2010) [93].

$$\alpha_o = \frac{\lambda_{\mathrm{ref}}\mathrm{Nu}_{\mathrm{ref}}}{(\frac{\mu_{\mathrm{ref}}^2}{\rho_{\mathrm{ref}}^2}g)^{1/3}} \tag{4.22}$$

In which, the refrigerant Nusselt number $\mathrm{Nu}_{\mathrm{ref}}$ is the average of laminar and turbulent flow.

$$\mathrm{Nu}_{\mathrm{ref}} = \sqrt{\mathrm{Nu}_{\mathrm{lam}}^2 + \mathrm{Nu}_{\mathrm{turb}}^2} \tag{4.23}$$

With Nusselt number of laminar and turbulent flow

$$\mathrm{Nu}_{\mathrm{lam}} = 0.9\mathrm{Re}_{\mathrm{film}}^{-1/3} \tag{4.24}$$

$$\mathrm{Nu}_{\mathrm{turb}} = 0.00622\mathrm{Re}_{\mathrm{film}}^{0.4}\mathrm{Pr}_{\mathrm{film}}^{0.65} \tag{4.25}$$

In which Reynolds number for the film is defined as Eq. (4.26).

$$\mathrm{Re}_{\mathrm{film}} = \frac{c_r \dot{m}_{\mathrm{ref}}}{\mu_{\mathrm{ref}}} \tag{4.26}$$

c_r is the circulation ratio and has been estimated from the refrigerant pump characteristic to be 48.

Energy conservation is derived then for each control volume as Eq. (4.27)

$$\dot{m}_H^{j+1} h_H^{j+1} + \dot{m}_{\mathrm{sol}}^{j+1} h_{\mathrm{sol}}^{j+1} + \dot{Q}_j = \dot{m}_H^j h_H^j + \dot{m}_{\mathrm{sol}}^j h_{\mathrm{sol}}^j \tag{4.27}$$

In which,

$$\dot{Q} = U_i A_i \Delta T_{\log} \tag{4.28}$$

4.5. MATHEMATICAL MODEL OF THE COLD STORAGE OF CO_2 SLURRY

Fig. 4.5 shows a schematic of the storage vessel of CO_2 hydrate slurry. It is both connected to the fluidized bed where the crystals are produced and to the melting heat exchanger in which part of the flow is molten. Fig. 4.5 also shows that a cooling load, $\dot{Q}_{\mathrm{load}}$, is applied to the slurry flow as it passes the melting heat exchanger. The storage vessel is very well insulated and the temperature between environment and storage is quite small so that it can be assumed that the energy input from the environment through the insulation material is zero. The storage vessel is considered to be well-mixed so that a single control volume can represent the conditions encountered in practice. The enthalpy at the outlet of the melting heat exchanger is given by Eq. (4.29).

$$h_{m\_\mathrm{hex\_out}} = h_{m\_\mathrm{hex\_in}} + \frac{\dot{Q}_{\mathrm{load}}}{\dot{m}_{m\_\mathrm{hex}}} \tag{4.29}$$

The enthalpy of the slurry at the inlet of the storage vessel is given by Eq. (4.30)

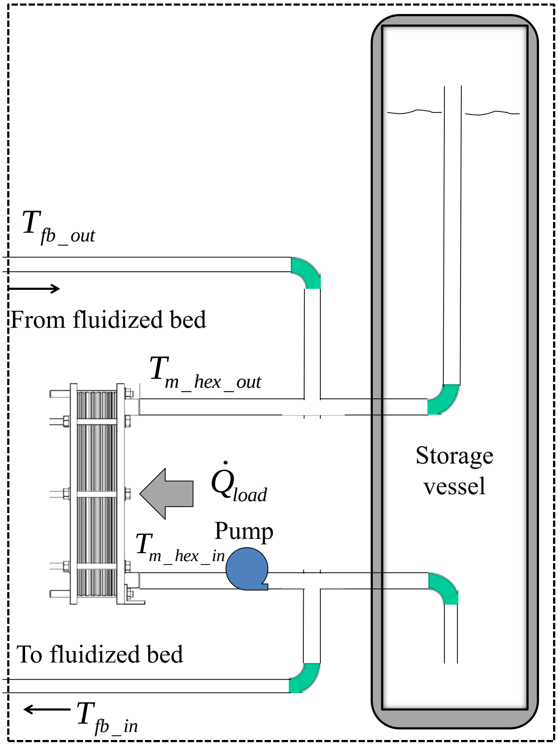

Figure 4.5: Connection of the storage vessel and melting heat exchanger. Partially molten slurry from the melting heat exchanger and slurry from the fluidized bed mix and flow into the storage vessel.

$$h_{\text{sv\_in}} = \frac{\dot{m}_{m\_\text{hex}} h_{m\_\text{hex\_out}} + \dot{m}_{fb} h_{fb\_\text{out}}}{\dot{m}_{m\_\text{hex}} + \dot{m}_{\text{fb}}} \tag{4.30}$$

The energy input from the pump is negligible so that $T_{\text{sv}_{\text{out}}} = T_{m_{\text{hex}_{\text{in}}}} = T_{\text{fb}_{\text{in}}}$ and the enthalpy at the outlet of the storage vessel is given by Eq. (4.31)

$$h_{\text{sv\_out}} = f(T_{\text{sv\_out}}, w_{H\_\text{sv}}, w_{\text{CO}_2}) \tag{4.31}$$

The hydrate mass concentration at the outlet of the melting heat exchanger follows from the melting enthalpy of the crystals as given in Eq. (4.32).

$$w_{H\_m\_\text{hex\_out}} = w_{H\_\text{sv}} - \frac{\dot{Q}_{\text{load}}}{\dot{m}_{m\_\text{hex}} \times \Delta h_H} \tag{4.32}$$

So that the hydrate mass concentration at the inlet of the storage vessel can be obtained from Eq. (4.33).

$$w_{H\_sv\_in} = \frac{\dot{m}_{m\_hex} w_{H\_m\_hex\_out} + \dot{m}_{fb} w_{H\_fb\_out}}{\dot{m}_{m\_hex} + \dot{m}_{fb}} \tag{4.33}$$

The hydrate mass concentration in the storage vessel as a function of time can finally be obtained from Eq. (4.34).

$$w_{H\_sv} = \int \frac{(\dot{m}_{m_{hex}} + \dot{m}_{fb}) w_{H\_sv\_in} - (\dot{m}_{m\_hex} + \dot{m}_{fb}) w^{t-1}_{H\_sv}}{\rho_{sv} V_{sv}} dt \tag{4.34}$$

Where the superscript $t-1$ indicates the value from the previous time step.

4.6. RESULTS

4.6.1. EXPERIMENTAL RESULTS AND MODEL VALIDATION

EXPERIMENTAL PHENOMENON

From the sight-glass installed in the system shown in Fig. 4.1, the hydrate formation process can be visualized. Fig. 4.6 shows how the solution circulating through the system changes from solution to slurry. The transition from solution to slurry is instantaneous.

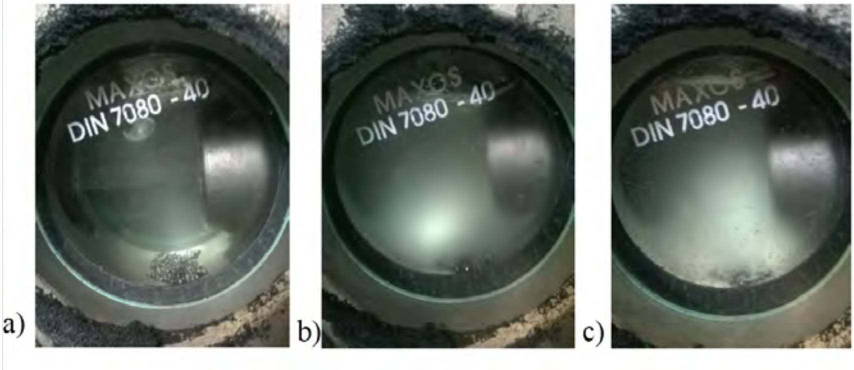

Figure 4.6: Transition from solution to slurry a) before hydrates are formed b) few hydrates are formed; c) more hydrates are formed indicated by the turbid solution.

CALCULATION OF HYDRATE GROWTH RATE

The experimental set-up has been designed to allow for continuous removal of the hydrate slurry from the storage vessel. For this purpose the set-up is equipped with a pressure controller which adds CO_2 vapor to keep the pressure in the system constant when experiments are done in open system configuration. A liquid level controller in the storage vessel allows for the injection of additional water so that the level is maintained. The CO_2 vapor added is consumed by the production of hydrates in the fluidized bed heat exchanger. In this way it is possible to determine experimentally the CO_2 consumption and to determine the growth rate from it. Fig. 4.7 illustrates the data obtained during a specific experiment. The CO_2 consumption has been divided by the average temperature driving force because the evaporating temperature is not constant during the experiments and as the evaporating temperature decreases the CO_2 consumption increases. For this particular experiment the consumption is in average 4.6 kg h^{-1} K^{-1} and the average temperature difference is 1.6 K so that the CO_2 consumption is 7.5 kg h^{-1}. Assuming an occupancy of 70%, the hydrate production rate is then 32.2 kg h^{-1}. Similar experiments have been executed at different average evaporating temperatures so that the effect of driving force on hydrate production could be identified.

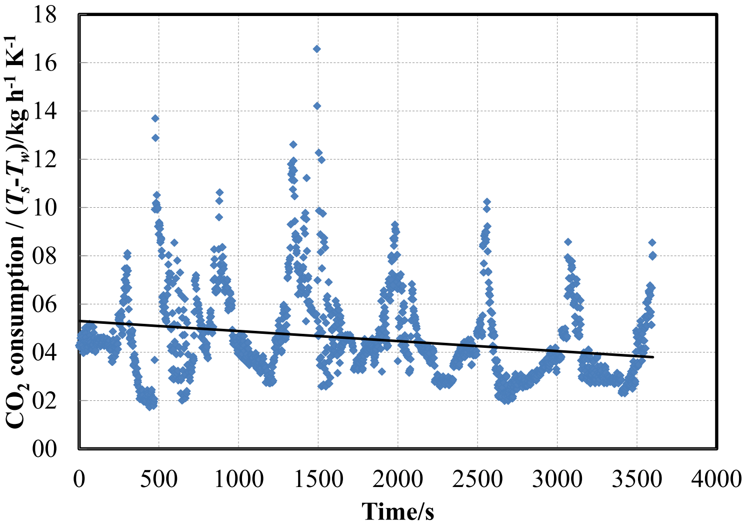

Figure 4.7: Ratio of CO_2 consumption and driving temperature difference bulk-to-wall as a function of time for the fluidized bed operating at 35.3 bar, inlet temperature of 8.6 °C and outlet temperature of 8.3 °C during 1 hour on the 4th of December 2014.

Originally Eq. (4.11) has been used to calculate the CO_2 diffusion coefficient in the solution, but this seemed to lead to an over prediction of the mass transfer when the heat and mass transfer analogy was applied. According to the Stokes-

Einstein equation, the diffusivity of liquids is influenced by the viscosity and temperature of the liquids as shown in Eq. (4.35).

$$\frac{D_{T_1}}{D_{T_2}} = \frac{T_1}{T_2}\frac{\mu_{T_1}}{\mu_{T_2}} \tag{4.35}$$

For this reason, Eq. (4.11) was rewritten to Eq. (4.36) to include the effect of higher viscosity of the slurry

$$D = \frac{\mu_{\mathrm{sol}}(T)}{\mu_s(T)} \exp\left[-(\frac{716.748}{T-126.9}) - 15.9\right] \tag{4.36}$$

Table 4.3 shows the comparison of experimental and predicted solid production as a function of refrigerant temperature when mass transfer equations (Eqs.(4.16), (4.17) and (4.36)) are used in the hydrate growth model for open systems. The correlation by Schmidt et al. (1999) [91] and analogy give results which show the same trends as the experiments. For instance between the 3rd and the 4th experiment, where only the inlet hydrate fraction has been changed, both the experimental and prediction by Schmidt et al. (1999)[91] show a decrease of about 40% of the hydrate growth rate. The analogy based on Haid's heat transfer correlation predicts a higher reduction. It also shows that the solid concentration influences hydrate growth rate significantly which can be explained as follows: as the hydrate concentration increases the slurry viscosity significantly increases, leading to a significant decrease of the mass transfer coefficient. This is also probably the reason why the analogy using Lu et al.'s [63] equation predicts the trend incorrectly: Eq. (4.11) has no relation to the viscosity. Table 4.3 also shows the analogy when the modified diffusion coefficient Eq. (4.36) is used and it is clear that it gives a reasonable prediction of the experiments.

Table 4.3: Comparison between the experimental hydrate production rate and the production rate predicted by the fluidized bed heat exchanger model for open systems.

ρ_s	P	w_{initial}	T_{in}	T_{evap}	ΔT	G_{exp}	G_{Schmidt}	G_{Analogy}	$G_{\mathrm{Analogy\_new}}$
kg m^{-3}	bar	%	°C	°C	K	kg h^{-1}	kg h^{-1}	kg h^{-1}	kg h^{-1}
1019	31.0	19.3	7.7	2.5	1.38	15.6	8.3	57.1	28.8
1017	31.0	8.7	8.2	3.1	1.23	8.2	7.0	31.3	23.7
1017	35.3	8.9	8.6	3.1	1.64	32.2	9.76	55.3	41.87
1022	35.6	33.8	8.7	3.1	1.67	22.0	6.3	53.4	14.13

Fig. 4.8 shows the density change of the solution with pressure and temperature for a closed system where no CO_2 is added during the experiment. The

system is cooled down gradually while hydrates are formed what is indicated by the increase of density in comparison with the solution density given by Eq. (4.3). Fig. 4.8 also shows the predicted slurry density which follows from the hydrate growth rate. The prediction based on the mass and heat transfer analogy appears to lead to a better prediction of the mass transfer process.

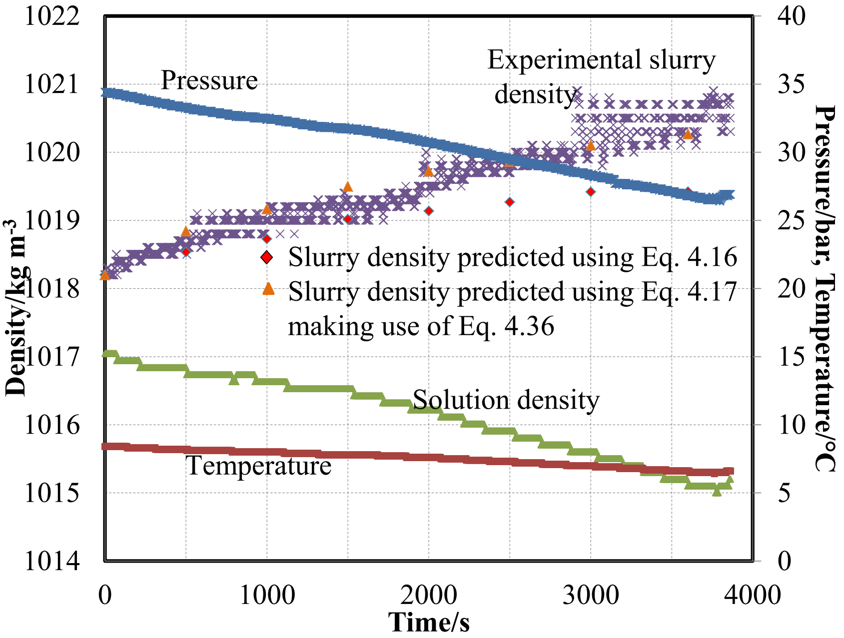

Figure 4.8: Experimental temperature, density and pressure at the fluidized bed inlet as a function of time. The figure also shows the solution density, making visible when hydrates are present.

Fig. 4.9 shows the change of solid (hydrate) fraction in a closed system under the conditions of the experiment reported in Fig. 4.8. Hydrate growth rate can be derived then from the change of solid fraction as 13.2 kg h^{-1} (volume of the total system is ca. 120 liter), which is quite comparable with the open system experiments reported in Table 4.3. The average operating conditions during this experiment are: pressure = 32.2 bar; slurry inlet temperature = 7.9 °C and evaporating temperature is 2.2 °C. Fig. 4.9 also shows the predicted solid concentration of the slurry that follows from the heat and mass transfer models. Again the prediction based on the heat and mass transfer analogy appears to reproduce the experimental data more accurately.

OVERALL HEAT TRANSFER COEFFICIENT DURING HYDRATE FORMATION PROCESS

The experimental overall heat transfer coefficient is calculated from the heat removed through the wall of the fluidized bed heat exchanger, Eq. (4.37).

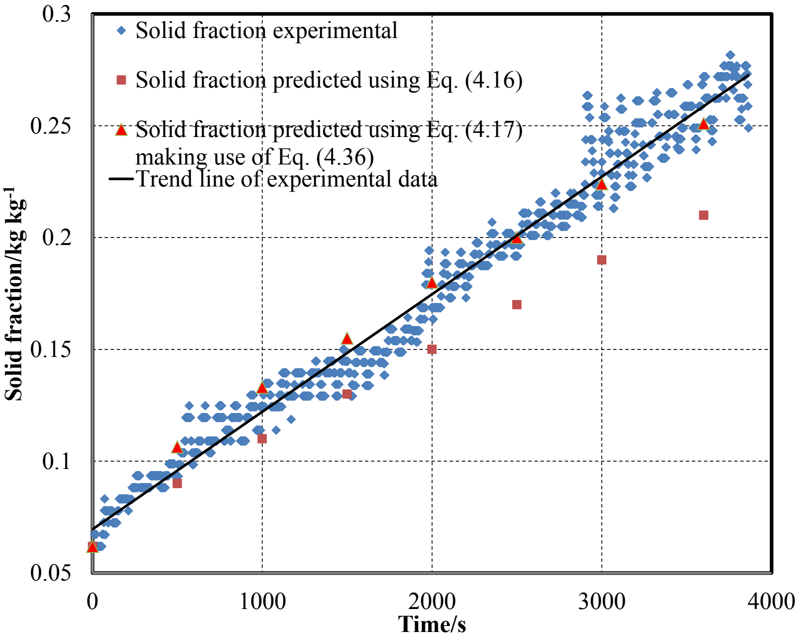

Figure 4.9: Solid fraction change in a closed system for the conditions of the experiment reported in Fig. 4.8. The solid line gives the trend line of the experimental data.

$$U_{i\_\text{exp}} = \frac{\dot{Q}_{\text{fb}}}{A_i \Delta T_{\log}} \tag{4.37}$$

The experimental fluidized bed heat transfer coefficient has been derived from Eq. (4.19) taking the heat transfer resistances of tube wall and evaporating refrigerant into account. Fig. 4.10 shows a comparison between the experimental and predicted heat transfer coefficient of the fluidized bed generator for one of the experiments. The figure also includes the ±5% lines making it clear that the data show a very good match indicating that Haid's correlation is capable of predicting heat transfer in fluidized beds for the production of CO_2 hydrates.

The maximum hydrate concentration attained during the experiments was 45%.

4.6.2. SYSTEM INCLUDING LHTS WITH A CONSTANT COOLING LOAD

The performance of the LHTS system with a constant cooling load of 4 kW has been investigated. The initial solid fraction in the system is 40 wt%. The results of the melting and solidification processes of the LHTS system are shown in Fig. 4.11. It can be observed that in the beginning, the production rate of hydrates

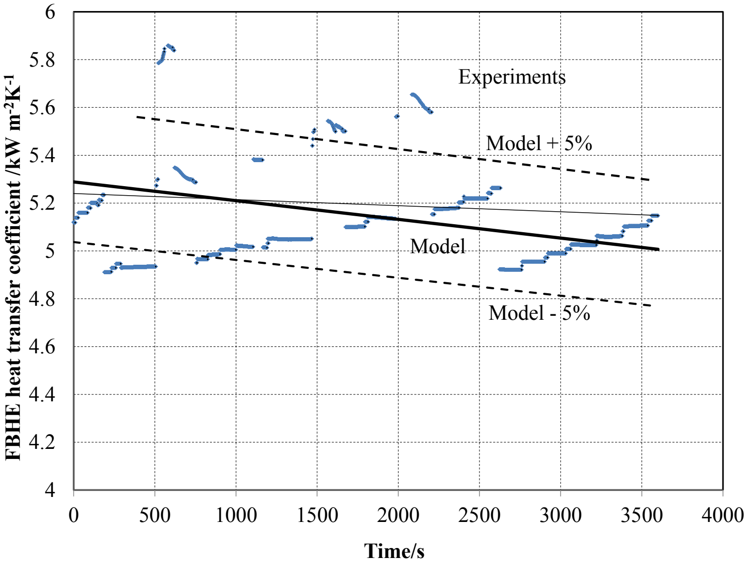

Figure 4.10: Comparison of the experimental and predicted fluidized bed heat transfer coefficient during slurry production in a closed system.

is lower than its melting rate. This can be explained by the fact that a high solid fraction gives a high viscosity of slurry which decreases the hydrate production rate according to the discussion in the last section. The solid fraction in the LHTS system becomes constant when the solid fraction has decreased to about 39.7 wt%. From this condition on, the production rate of hydrates in the FBHE equals to the melting rate of solids in the LHTS system.

4.6.3. SYSTEM INCLUDING LHTS WITH A VARIABLE COOLING LOAD

In this case, the cooling demand is not constant over time. The weather of Dutch climate (the five hottest days during the year of 1965 are selected) was used for the estimation of the cooling demand of a specific building. Three office rooms in the specific building have been adopted as the reference load for this study (Fan et al., 2014 [29]). Fig. 4.12 shows the flow chart of the conventional (Fig. 4.12a) and alternative (Fig. 4.12b CO_2 hydrate slurry) refrigeration system. The evaporation temperature in the conventional system is 2 °C.

The results of melting and solidification processes for the conventional and alternative refrigeration systems are shown in Fig. 4.13. The total energy consumption in the conventional system only takes the compressor power consumption into account as the power consumption of the pump to deliver water to the building is comparably small. While in the alternative system, an extra power

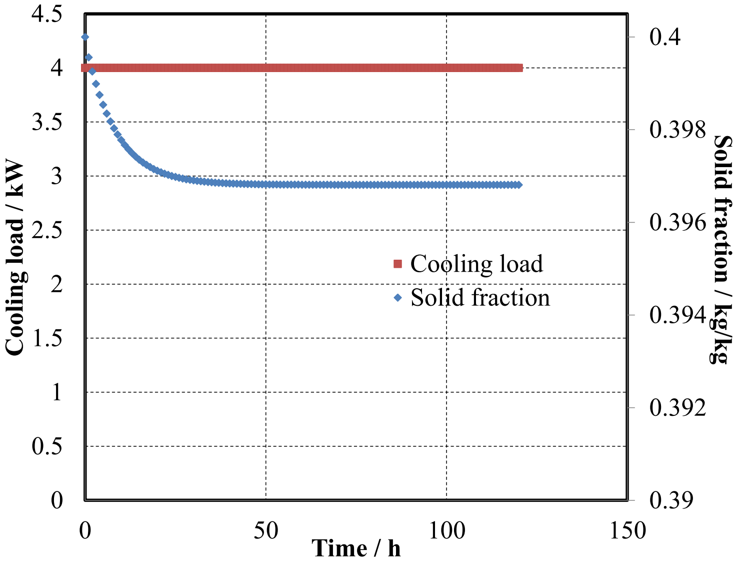

Figure 4.11: The results of solidification and melting processes when the cooling load is constant.

consumption is needed in the generation cycle of CO_2 hydrate slurry (Pump1).

Fig. 4.13a shows the power consumption in the conventional system. It shows a consistent trend of cooling demand and power consumption. The change of COP of the conventional system is shown in Fig. 4.13b. The average COP for this case is 4.8 as shown in Table 4.4. Fig. 4.13c shows the results of power consumption when hydrates are produced during the night time with a 70 liter LHTS system. Here hydrates are produced after 7 pm if the concentration of hydrates is lower than 10 wt%. It indicates that the storage tank is not big enough to shift the energy demand to night time generation of hydrate slurry totally, and it gives a COP of 4.4. Fig. 4.13d shows the power consumption when a 700 L storage tank is combined with the hydrate slurry generation system. It shifts the energy demand mostly to night time generation of hydrate slurry. It gives a higher COP of 5.8 as shown in Table 4.4, which is 23% higher than the conventional system. Therefore, it can be expected that for normal summer days, the energy efficiency can be significantly improved by using this alternative system with night time production. As Fig. 4.13d illustrates part of the slurry production needs to take place during the day. The average summer day will have lower cooling demand than these five peak days. In average days all the required slurry can be produced at night with higher COPs. This is illustrated in Fig. 4.13e which considers a total of 10 days. The average COP now becomes 6.9 (43% higher than the reference system).

Table 4.4: Performance of conventional and alternative refrigeration system.

System	Total cooling demand	Total energy consumption	Average COP
	kWh	kWh	5/10 days
Conventional	190.5	40.25	4.8
LHTS 70 L	190.5	43.6	4.4
LHTS 700 L	190.5	32.8	5.8/6.9

4.7. CONCLUSIONS

CO_2 hydrate slurry was selected as the PCM for the proposed application due to its high latent heat. A single tube fluidized bed heat exchanger was chosen for CO_2 hydrate slurry production, which gave an experimental production rate of up to 32 kg h^{-1} with a 0.5 m^2 cooled surface area.

A model has been proposed for the prediction of the CO_2 hydrate crystals production rate in fluidized bed heat exchangers. The model is based on existing heat and mass transfer correlations for fluidized bed heat exchangers and predicts the experiments data accurately.

The numerical model has been combined with an LHTS and used to predict the system performance during the five hottest days of the reference climate data of the Netherlands.

The COP of the system composed of fluidized bed for hydrate generation and LHTS appears to be 23% to 43% higher than the COP of a conventional system.

The heat transfer coefficient during hydrate generation in the fluidized bed heat exchanger was around 5000 W m^{-2} K^{-1} during the experiments.

During the experiments with continuous removal of the hydrate slurry so that the solid concentration was maintained constant, solid concentrations up to 35% could be maintained in the system.

During experiments in which only the originally injected CO_2 was consumed, concentrations up to 45% have been realized.

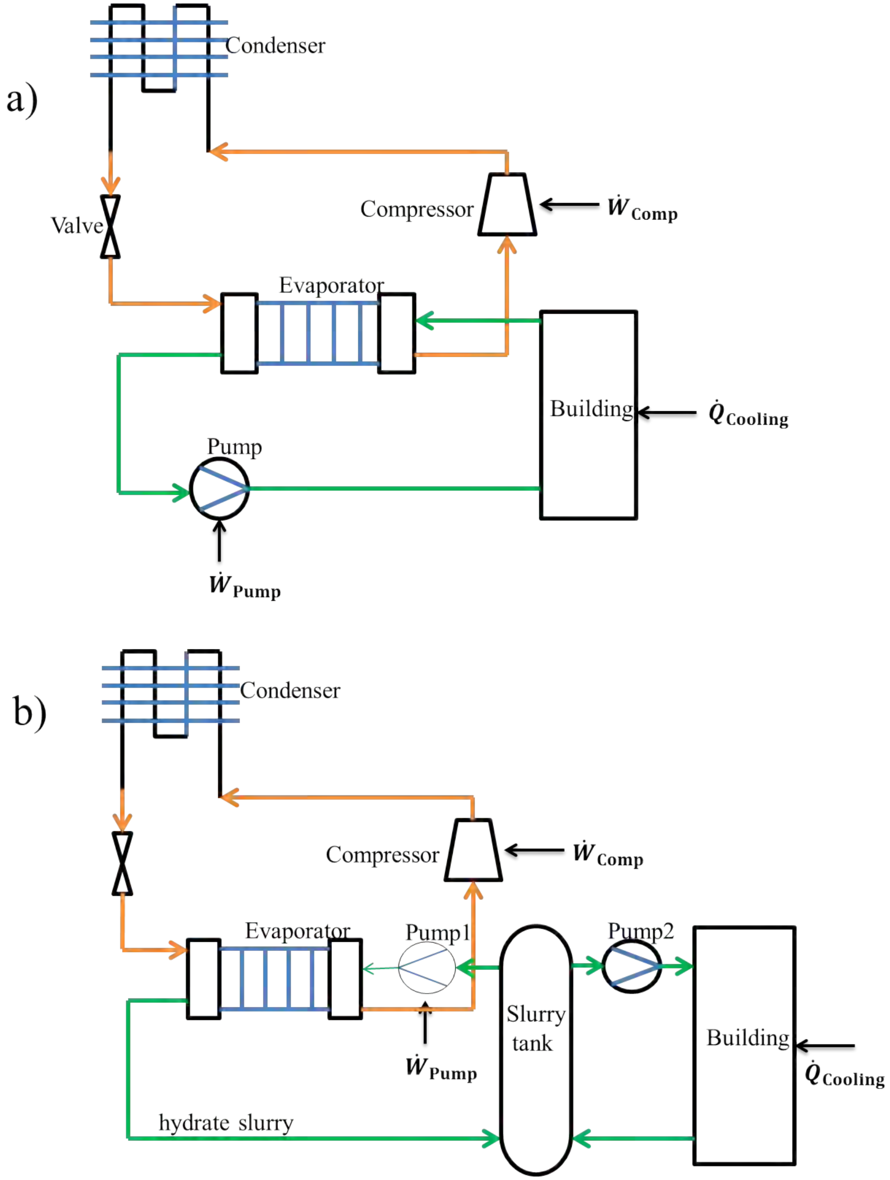

Figure 4.12: Diagram of the conventional and alternative refrigeration system. a) Conventional refrigeration system; b) Alternative refrigeration system with CO_2 hydrate slurry as secondary refrigeration fluid.

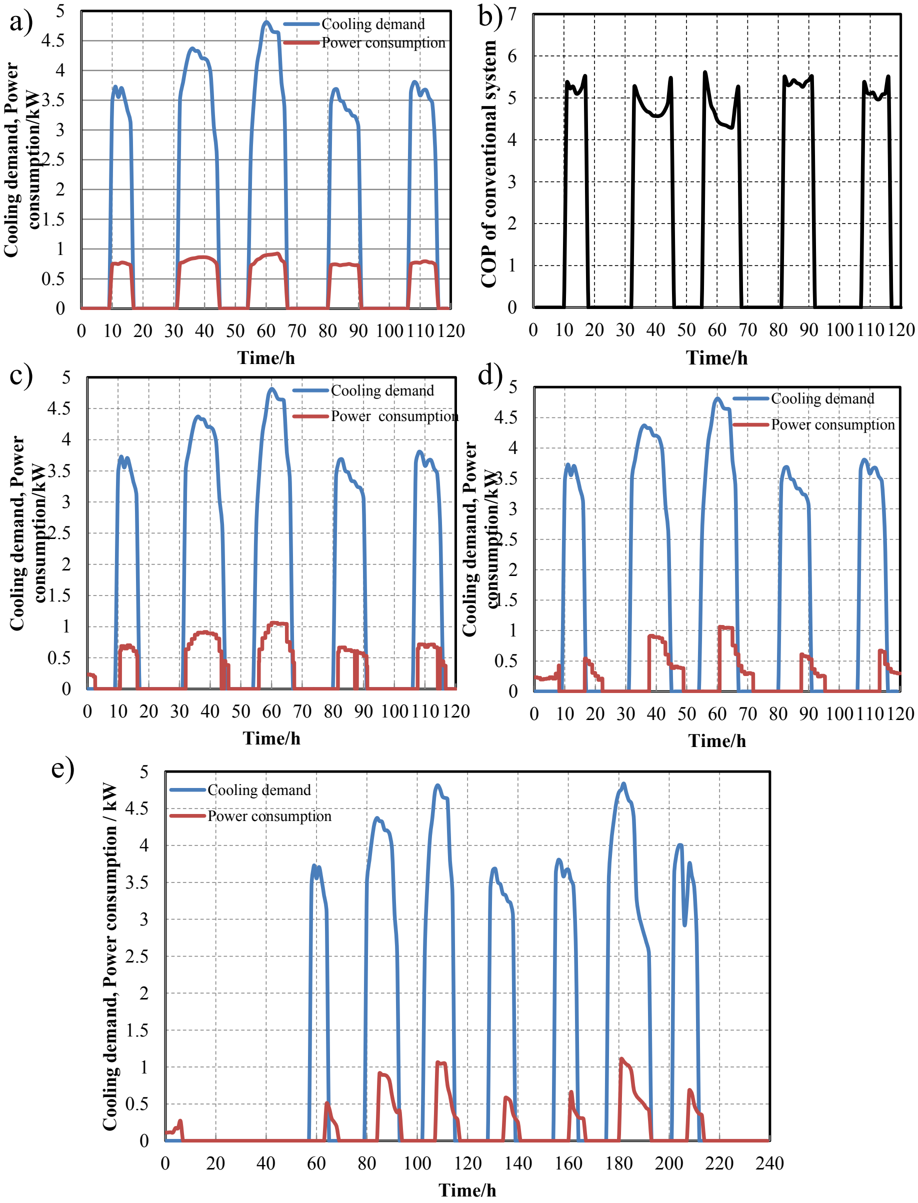

Figure 4.13: Performance of conventional and alternative refrigeration system with variable cooling demand. a) Cooling demand and power consumption of conventional refrigeration system during 5 days; b) COP of the conventional refrigeration system during 5 days; c) Cooling demand and power consumption of alternative refrigeration system with night time crystal generation combined with a 70 Liter LHTS system during 5 days; d) Cooling demand and power consumption of alternative refrigeration system with night time crystal generation combined with a 700 Liter LHTS system during 5 days; e) Cooling demand and power consumption of alternative refrigeration system with night time crystal generation combined with a 700 Liter LHTS system during 10 days.

5

EFFECT OF TYPE-III ANTI-FREEZE PROTEINS ON CO_2 HYDRATE FORMATION

This chapter introduces the influence of a gas hydrate formation preventer in order to use a simpler generator, for example, the coil heat exchanger mentioned in Chapter 2. In this way the investment of a project can be reduced.

Parts of this chapter have been published in Chemical Engineering Science, 167, 42-53 (2017) [134].

5.1. INTRODUCTION

Sari et al. (2008)[89] have studied the formation of CO_2 hydrate slurry in a double tube heat exchanger. They injected high pressure CO_2 into cooled solution to form hydrate slurry under temperature range 1.5 ~ 2°C and pressure about 35 bar. In their case, formation and dissociation are processed alternatively. This low temperature of hydrate slurry is not beneficial when the slurry is applied in air-conditioning systems. Marinhas et al. (2006)[69] studied CO_2 hydrate slurry flow in tubes. The total volume of their experimental loop is 0.297 L, with flow velocity maximum 0.93 m s^{-1}. The experimental device is placed in an air-controlled room horizontally. Hydrate dissociation is processed after 2 hours of formation. The experimental condition of their experiments is along the Lw-H-V (aqueous-hydrate-vapor) line. Yang et al. (2011)[121] studied CO_2 hydrate formation in a fin-tube heat exchanger. The diameter of the tube is 8 mm. There are 180° bends in the tube exchanger. The longest stable run has lasted for more than 1 h and was limited by the recirculation of process water. All of the investigations mentioned above have one thing in common, in their apparatus, there is no free space for gas phase, all the gas is dissolved into the solution. Jerbi et al. (2010)[48] studied CO_2 hydrate slurry formation and dissociation in the same apparatus as Marinhas et al. (2006)[69]. They did two different types of experiments: 1) open system: firstly cool down water/solution to subcooling, and then inject CO_2 into the subcooled solution to form hydrate (Pre-cooling) and the pressure is maintained by filling CO_2 continuously. 2) closed system: firstly inject CO_2 into water making a CO_2-saturated solution, and then cool down the solution until hydrates are formed (Pre-injection), no extra CO_2 is charged during the process. It is concluded from their experiments that the continuous filling of CO_2 in the open system provides a force for hydrate formation, which results in a larger amount of hydrates formation in the same period compared with that in the closed system. However, it's easier to obtain the hydrate formation rate from gas consumption in the second method (closed system).

Formation of gas hydrates in oil and gas pipelines and processing equipment is something that the petroleum industry is most concerned about since it can lead to flow blockage and severe economic loss[102]. Chapter 4 introduces the production of CO_2 hydrate slurry in a Fluidized Bed generator, which has been patented by Waycuilis and York [116]. However, the construction of such a system with a fluidized bed heat exchanger requires a large investment which is not cost-effective for industry. Simpler coil heat exchangers are expected to significantly improve the cost-effectiveness of these systems. The generator introduced in Chapter 2 is used in this chapter to produce CO_2 hydrate slurry. CO_2 gas is injected to the system by a long tube to mix with water (containing antifreeze proteins (AFPs) or not). The CO_2 saturated water solution is cooled down to form hydrates. However, this process is different from the second method mentioned by Jerbi et al. (2010). A gas volume is maintained above the liquid and the solution is continuously sprayed into the gas phase. The apparatus of Jerbi et al. (2010) is completely filled with the solution so that there is no separate gas volume. The vessel used in this study has approximately 1.5 L filled with the gas phase. The gas volume prevents large pressure changes in the system. The extremely rapid formation rate attained in these heat exchangers cannot be controlled, so that a blockage of the flow always limits the operation as shown in Fig. 5.1. In order to use this simpler generator to produce CO_2 hydrate continuously, it is necessary to slow down the formation rate and so to prevent the blockage. Addition of a hydrate inhibitor is proposed to control the hydrate formation process so that the slurry remains pumpable.

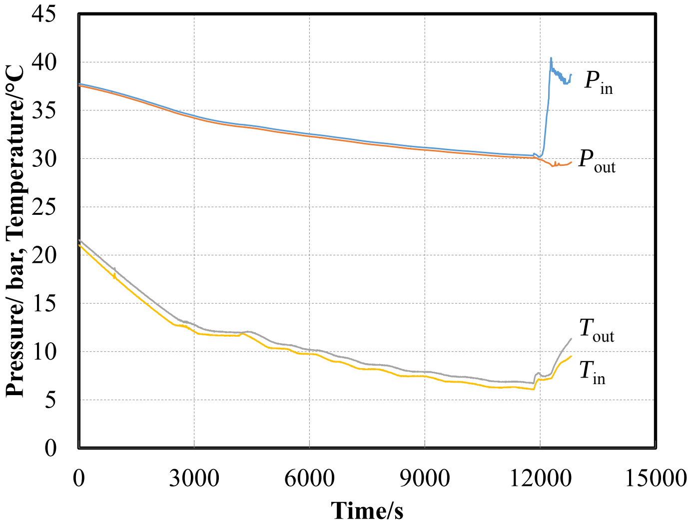

Figure 5.1: Experimental data of the system pressures and temperatures showing that CO_2 hydrate formation is too fast to be controlled in the coil heat exchanger.

It is known that thermodynamic hydrate inhibitors (THIs) including sodium chloride, methanol and glycol are the most popular hydrate inhibitors in the oil and gas industries (Yousif, 1996 [126]; Ebeltoft et al., 1997 [26]; Talaghat, 2014a,b [106][107]). However, most of the thermodynamic inhibitors have to be used at high concentrations (10-50 wt%) in order to be effective which makes them less attractive (Kelland et al., 2006 [52]). Kinetic hydrate inhibitors (KHIs) are thought to be a better alternative for hydrate formation control. PVP (polyvinyl pyrrolidone), PVCap (polyvinyl caprolactam), N-Vinyl pyrrolidone-co-N-Vinyl caprolactam [poly (VP/VC)], and some lactam terpolymers are typical commercial KHIs. It has been proved that KHIs cannot avoid hydrate formation but can hinder hydrate nucleation or/and growth by adsorbing to nucleation sites or/and growth sites (Yang and Tohodi, 2011 [122] and Fernando and Kelland, 2013 [32]). Sakaguchi et al. (2003) [88] studied the inhibition of PVP and PVCap on structure-II hydrate crystals. They found the addition with 0.2 wt% of PVCap could strongly inhibit the hydrate growth along the interface. The addition of PVP even changes the morphology of hydrate crystals growing along the interface. Anti-Freeze Proteins (AFPs) have been proved to be efficient and comparable to the commercial polymeric inhibitors on inhibition of gas hydrate formation by Shadi et al. (2008) [95]. Additionally, AFPs are 'green inhibitors' making them acceptable for both environment and human safety (Walker et al., 2015 [114]).

Anti-Freeze Proteins (AFPs) refer to a class of poly-peptides produced by certain vertebrates, plants, fungi and bacteria that permit their survival in subzero environments[12]. There are different types of AFPs as shown in Table. 5.1.

Table 5.1: Details of different types of AFPs.

Characteristic	AFGP	Type I AFP	Type II AFP	Type III AFP	Type IV AFP
Mass (kDa)	2.6-33	3.3-4.5	11-24	6.5	12
Key properties	AAT repear; disaccharide	Alanie-rich α -helix	Disulfide bonded	B-sandwich	Alaninerich helical bundle
Natural source	Antarctic Notothenioids; northern cods	Right-eyed flounders; sculpins	Sea raven; smelt; herring	Ocean pout; wolfish; eel pout	Longhorn sculpin

*1 Da = 1 gram per mole; *AFGP: antifreeze glycoprotein.

Antson et al. (2001) [8] studied the mechanism of type-III AFPs on ice growth. They confirm that type-III AFPs can make energetically favorable interactions with several ice surfaces, in which way inhibiting crystal growth. Kutschan et al. (2014) [57] studied the dynamic mechanism of AFPs on inhibiting of ice growth and derived a correlation of the induction time as a function of concentration. The depression of the freezing temperature of four different AFPs types have been investigated as shown in Fig. 5.2, which shows that the addition of AFP increases the depression temperature of freezing, which means the formation of ice is more difficult. Bagherzadeh et al. (2015) [10] pointed out that the ice-binding AFPs can act as a gas hydrate inhibitor. Celik et al. (2010) [13] pointed that AFPs also modestly contribute to ice crystal superheating during melting, so that the action between AFPs and the ice surface results in a separation of the freezing point and the melting point, which is a phenomenon termed thermal hysteresis. And they mentioned the temperature change by thermal hysteresis could be about 0.5 K for moderate thermal hysteresis AFPs, such as type-III AFPs.

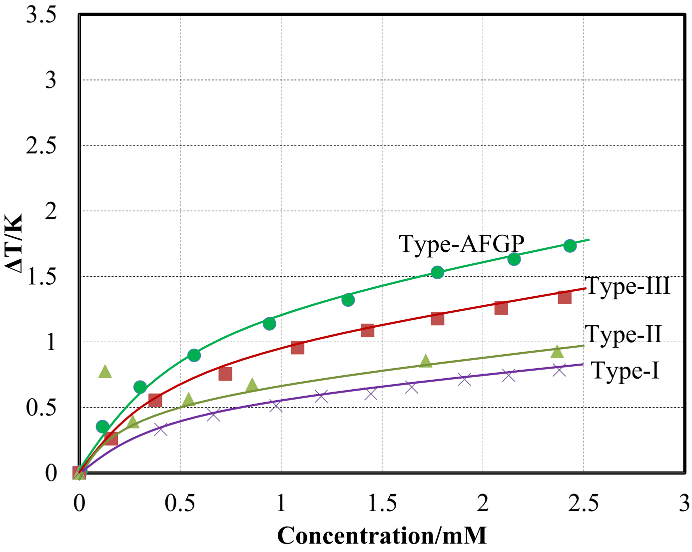

Figure 5.2: Supercooling degree before nucleation starts for four different classes of AFP structures (from [57]) variation with concentration.

In this chapter the effect of type-III AFPs on CO_2 hydrate formation rate in a coil heat exchanger is investigated. The experimental results are compared to those obtained using other additives including poly[VP/VC], which is the leading KHI on the market, and thus serve as good references when testing the KHI potential of the AFPs. A general hydrate growth equation is used to derive the change in experimental mass transfer coefficient of CO_2 from bulk liquid phase to the crystal layer. The results can be used to guide the design of a crystallizer when continuous CO_2 hydrate slurry is to be produced.

5.2. EXPERIMENT

5.2.1. EXPERIMENTAL APPARATUS

The experimental set-up used in this chapter is the same as the one shown in Chapter 2. The water filled in the system is ultra-deionized water which is used to make sure that nothing can affect the hydrate formation except the selected additive as it is well-known that electrolyte ions (like Na^+, Mg^{2+} and Cl^- etc) can inhibit the formation of gas hydrate. The experimental apparatus was filled with the ultra-deionized water and circulated to clean the system before any experiments are processed. The total volume of the solution filled in the system is 2.5 L. It includes 1.5 L solution in the storage vessel and 1.0 L solution in the connection tubes.

Details of the accuracy of the measuring instruments and derived parameters have been reported in Chapter 2, Table 2.1.

5.2.2. EXPERIMENTAL PROCEDURE

As the validation of the experimental system has been done in Chapter 2, the experiments are processed directly with CO_2 water solution. Experiments were run for long periods and generally the system was maintained at constant temperature driving force for at least 30 minutes so that quasi-steady state conditions would apply. The pressure drop when CO_2 solution flows in the system is shown in Fig. 5.3.

Fig. 5.3 shows a comparison of predicted and experimental pressure drop of water and CO_2 water solution under similar conditions as a function of flow rate. The concentration of CO_2 in the solution in the test is in the range of 2-3 mol%, which can be derived from Diamond and Akinfiev (2003)[18] along the coexistence of aqueous liquid + CO_2-rich liquid + CO_2-rich vapor. It indicates that the pressure drop of water test can be well predicted, with error 1.9% and 3.7% for flow rate 70 kg h^{-1} and 80 kg h^{-1} respectively. Fig. 5.3 also shows that when CO_2 is added, so that the operating pressure rises to about 30 bar, the pressure drop increases. Notice that Fig. 5.3 concerns operating conditions in the aqueous solution – gas region in which there is no hydrate formation. Under these conditions not all CO_2 gas is dissolved and small CO_2 gas bubbles circulate through the system. Again the pressure drop is reasonably well predicted when a two-phase multiplier of 1.14 is applied to the pressure drop predicted for single phase liquid flow. This is indicated in the figure by the dotted line. If a Lockhart–Martinelli based two-phase pressure drop prediction method (Fsadi and Whitty, 2016 [35]; Lockhart and Martinelli, 1949 [61]) is used, such multiplier corresponds to a non-dissolved gas fraction of less than 0.2%. The under-prediction of the pressure drop at lower flows indicates that with lower velocities the gas fraction increases while with higher flows the pressure drop is over-predicted because the gas frac-

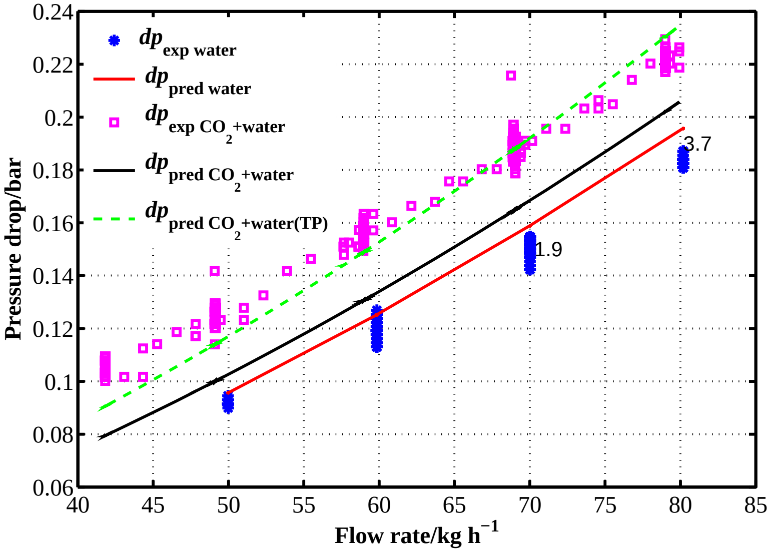

Figure 5.3: Pressure drop during pure water and water+CO_2 experiments at similar temperature. When CO_2 is added to the water the pressure in the system rises from slightly above atmospheric pressure to around 30 bar. The lowest line shows the predicted pressure drop of water; the intermediate line shows the predicted single phase pressure drop of the solution; the top line (dotted) shows the predicted two-phase pressure drop of the solution taking the effect of non-dissolved CO_2 gas into account.

tion reduces.

The heat transfer characteristics of the system with CO_2 solution is investigated. The experimental overall heat transfer coefficient of the system is calculated based on the energy balance that follows from the measured temperatures, pressures and flow rates as shown in Eq. (5.1).

$$U_{\text{exp}} = \frac{\dot{m}\Delta h - \dot{m}\frac{\Delta P}{\rho_S} - \dot{Q}_{\text{loss}}}{A\Delta T_{\text{log}}} \tag{5.1}$$

The energy loss in Eq. (5.1) has been estimated to be equal to 3 W by calculating it from the length of the tube and its insulation thickness. Compared with the maximum cooling capacity, 0.3 kW, the energy loss is very small.

The general overall heat transfer coefficient without hydrates formation is calculated by Eq. (5.2) which is based on the internal area of the coil.

$$\frac{1}{U} = \frac{1}{\alpha_i} + \frac{d_i \ln\frac{d_o}{d_i}}{2\lambda_w} + \frac{d_i}{d_o}\frac{1}{\alpha_o} \tag{5.2}$$

The external heat transfer coefficient h_o is derived from Eq. (5.3) which has been validated in Chapter 2. The internal heat transfer coefficient is predicted with the correlation proposed by Xin and Ebadian (1997) [119], which is obtained experimentally for the local heat transfer around helical pipes for laminar regimes. Since, as discussed above, the gas fraction in the solution flow is very small, this single-phase flow equation is assumed to apply for the CO_2-water solution.

$$\alpha_o = 1.4\dot{q} + 30.697 \tag{5.3}$$

Fig. 5.4 shows the comparison of the predicted and experimental overall heat transfer coefficient of CO_2+water solution. It indicates that Eq. (5.2) under predicts the experimental results, however, the average deviation is within ±10%, which is considered acceptable.

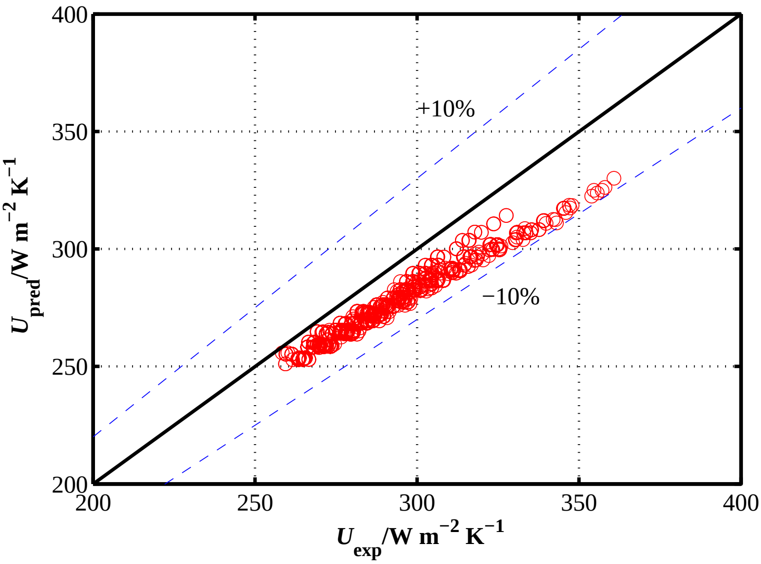

Figure 5.4: Comparison of experimental and predicted overall heat transfer coefficient for water+CO_2 solution test.

After validation, water is firstly filled into the set-up, then CO_2 is filled until a certain pressure is reached. Experiments are firstly processed without the addition of AFPs to determine the initialization point of hydrate formation and the condition for which blockage of the flow occurs. After that, the system is drained and cleaned by water before new solution with the addition of AFPs is filled. The type-III AFP used in the experiments was purchased from A/F Protein

Canada Inc. The solution with or without AFPs in the coil is cooled by the two thermostatic baths filled with tap water from 10 °C with steps of 0.5 K until there are crystals appearing in the sight glasses. Fig. 5.5 shows the photos taken before and after hydrates appear in the sight glass. The effective cooling capacity of each bath is 0.3 kW. The warm bath is kept at a temperature higher than the cold bath, in this way, part of the crystals formed in the cold bath will melt. In this way, solidification and melting processes of crystals allow for the fluid to remain pumpable even at higher solid concentrations.

Figure 5.5: Hydrate formation periods. Left: before hydrates appear; Center: In the middle of hydrate formation; Right: Blockage in the end of hydrate formation.

5.3. EXPERIMENTAL RESULTS

The experiments have been conducted by maintaining the temperature of the two thermostatic baths at a low temperature as mentioned in Chapter 2. Each temperature set-point combination for the two baths is maintained for at least 30 minutes. When the temperature set points are changed the system requires some time to stabilize. This non-stationary period is not considered in the processing of the data so that steady state correlations can be used for the evaluation of the data.

5.3.1. EXPERIMENTAL RESULTS WITHOUT ADDITION OF AFPS

Figs. 5.6-5.8 show the temperature/pressure profile, supercooling degree, energy flow/overall heat transfer coefficient and pressure drop of three experimental conditions. The solution velocity of these three cases is 0.56 m s^{-1}, 0.68 m s^{-1} and 0.85 m s^{-1} respectively. The solution temperature is controlled by the two thermostatic baths and is given in Fig. 5.6a. Fig. 5.6a shows that due to the low pressure in the process, there is a gas refilling during the experiment in order to reach the hydrate formation region. The gas refilling is indicated by the sudden pressure increase before hydrates are formed (starting by the dashed red line) in Fig. 5.6b. While for the other two cases, gas filling is done at least one day before, and a high pressure is maintained before experiments are done, so there is no gas filling in the experimental day. The temperature difference between the solution and corresponding equilibrium temperature under the same pressure, which is defined as $dT = T_{\text{sol}} - T_{\text{sat}}$, is used to show how far the solution deviates from equilibrium, while the equilibrium temperature is derived from Sabil (2009)[87] as $T_{sat} = -0.0072P^2 + 0.6874P - 6.4999$. The differences between the inlet and outlet solution temperature and saturation are shown in Fig. 5.6c. The accuracy of these temperatures differences is ± 0.03 K. The figure indicates that the temperature difference of the inlet temperature of solution reached -1.5 K before a blockage took place. For case 2 and case 3, the deviation from saturation is – 1.2 K and 0.4 K, respectively. This shows that the flow velocity influences the hydrates formation: the higher the velocity, the lower the temperature difference which leads to a blockage. Fig. 5.6d shows the change of sensible energy flow, $\dot{Q}$, and of the overall heat transfer coefficient during the experiment. The sensible energy flow $\dot{Q}$ is derived from $\dot{Q} = \dot{m}c_p(T_{\text{in}} - T_{\text{out}})$ and excludes the latent heat of hydrate formation. Figs. 5.7d and 5.8d show that when the temperature crosses the saturation line, $\dot{Q}$ decreases, indicating that when the temperature of solution decreases below the saturation temperature, there are crystals formed, which is marked by the dashed vertical line. And correspondingly, there is a pressure increase which is shown in Figs. 5.7e and 5.8e. However, as the crystals are formed there is no $\dot{Q}$ decrease and also no pressure increase in case 1 as shown in Fig. 5.6d and Fig. 5.6e respectively. It is possibly because in case 1, crystals are formed in the solution because of too many gas bubbles in the solution due to gas refilling, while for the other two cases, CO_2 gas was already dissolved into the solution. In this later case, crystals are more likely formed on the wall due to the lower temperature of the wall. The dissolution heat and crystal formation heat cancelled out resulting the level out of $\dot{Q}$. Fig. 5.6e also shows significantly larger oscillation of the pressure drop than Fig. 5.7e and Fig. 5.8e, indicating that crystals are passing the pressure sensors. Figs. 5.7d and 5.8d also show that the $\dot{Q}$ value presents very large instantaneous changes during the formation period. This is caused by a change of set-point of the thermostatic bath which induces a temperature change of the solution. Since T_{in} and T_{out} are measured at the same instant, such temperature changes lead to a jump in the $\dot{Q}$ value and as a results also of the corresponding U value.

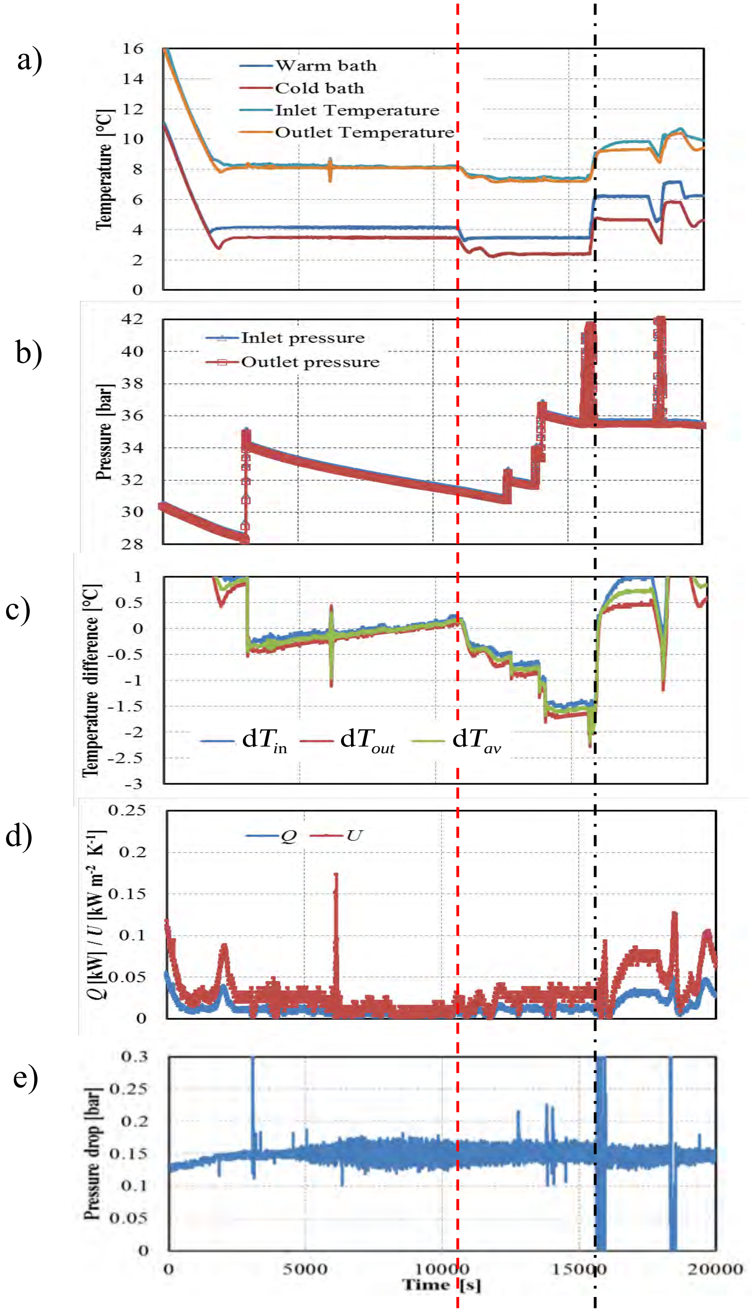

Figure 5.6: Experimental results for water+CO_2 test during hydrate formation period with solution velocity of 0.56 m/s: a) temperature change, b) pressure change, c) Temperature difference change; d) energy flow/heat transfer coefficient change; e) pressure drop change.

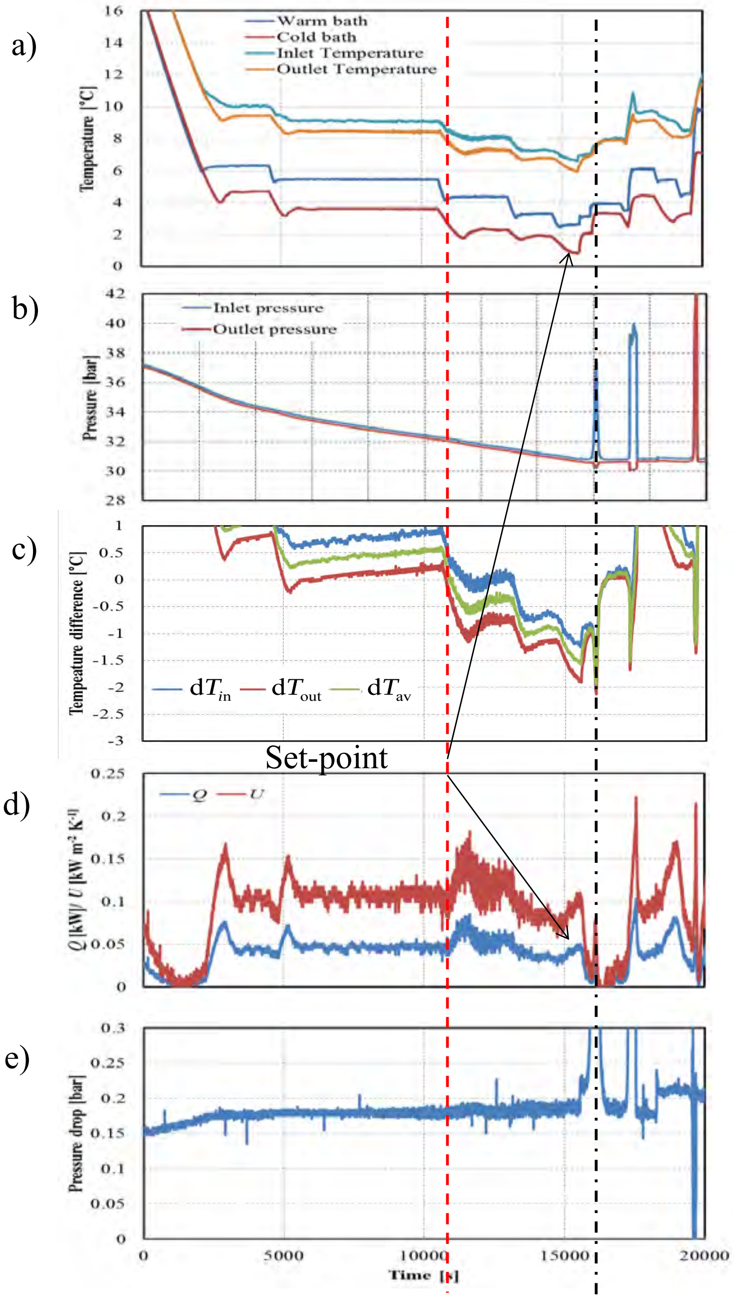

Figure 5.7: Experimental results for water+CO_2 test during hydrate formation period with solution velocity of 0.68 m/s: a) temperature change, b) pressure change, c) Temperature difference change; d) energy flow/heat transfer coefficient change; e) pressure drop change.

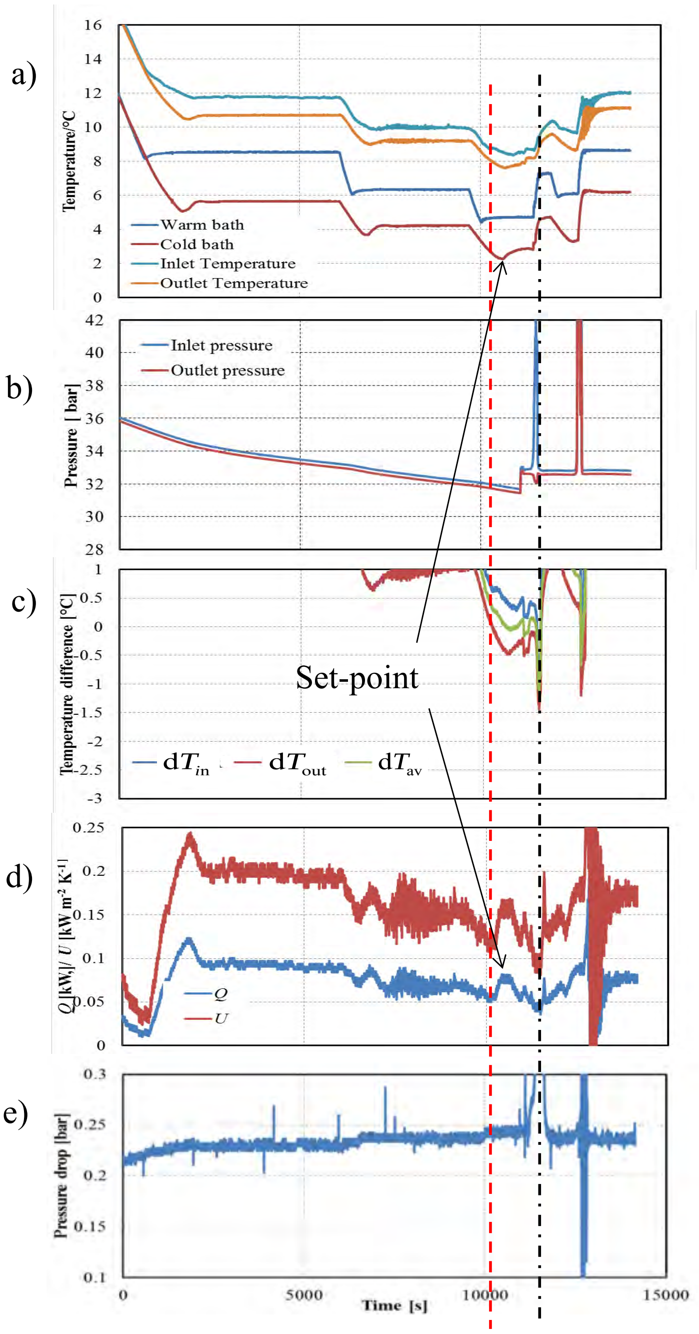

Figure 5.8: Experimental results for water+CO_2 test during hydrate formation period with solution velocity of 0.85 m/s: a) temperature change, b) pressure change, c) Temperature difference change; d) energy flow/heat transfer coefficient change; e) pressure drop change.

From the three cases, it is concluded that hydrates start forming when the temperature of solution is slightly below the equilibrium temperature. The second conclusion is that the higher the solution velocity, the easier the hydrates start forming on the wall. So a lower velocity will be adopted in the next experiments. Additionally when gas is refilled during an experiment, CO_2 gas will not totally be dissolved into the solution before hydrates start forming. In the later experiments with the addition of AFPs, CO_2 gas is firstly filled to the system at least one day before the experiments are executed.

5.3.2. EXPERIMENTAL RESULTS WITH THE ADDITION OF AFPS

As discussed above, the experiments with the addition of AFPs have been done under low velocity (0.56 $\mathrm{m\,s^{-1}}$) of the solution and CO_2 gas has been filled in advance to the experiments. Two cases of CO_2 hydrate formation with the addition of 10 ppm AFPs are shown as Figs. 5.9-5.10. Fig. 5.9c indicates an inlet temperature difference of -1.9 K when the system blocks while Fig. 5.10c shows -1.7 K for case 2. This is caused by the larger temperature difference of the two baths. Fig. 5.9a shows that the temperature difference between the two baths is maintained at 1.5 K while that is 2.0 K for case 2 shown in Fig. 5.10a. For the two cases, the solution velocity is 0.56 $\mathrm{m\,s^{-1}}$, and no gas has been refilled during the experiments. Notice that for the cases without addition of AFPs, shown in Figs. 5.6-5.8, the solution velocity has been varied and in the case of Fig. 5.6 gas has been refilled. Solution velocity has less impact than gas refilling on the results as illustrated in Figs. 5.6-5.8. For this reason the case shown in Fig. 5.7 is used for comparison with Figs. 5.9-5.10. Results show that the temperature difference when blockage occurs is similar for both with and without addition of AFPs, indicating a small effect of the additive. Figs. 5.9d and 5.10d show the same impact of the set-point change as discussed above.

Experimental results with higher concentration of AFPs (20 ppm - 50 ppm) are shown in Appendix D.

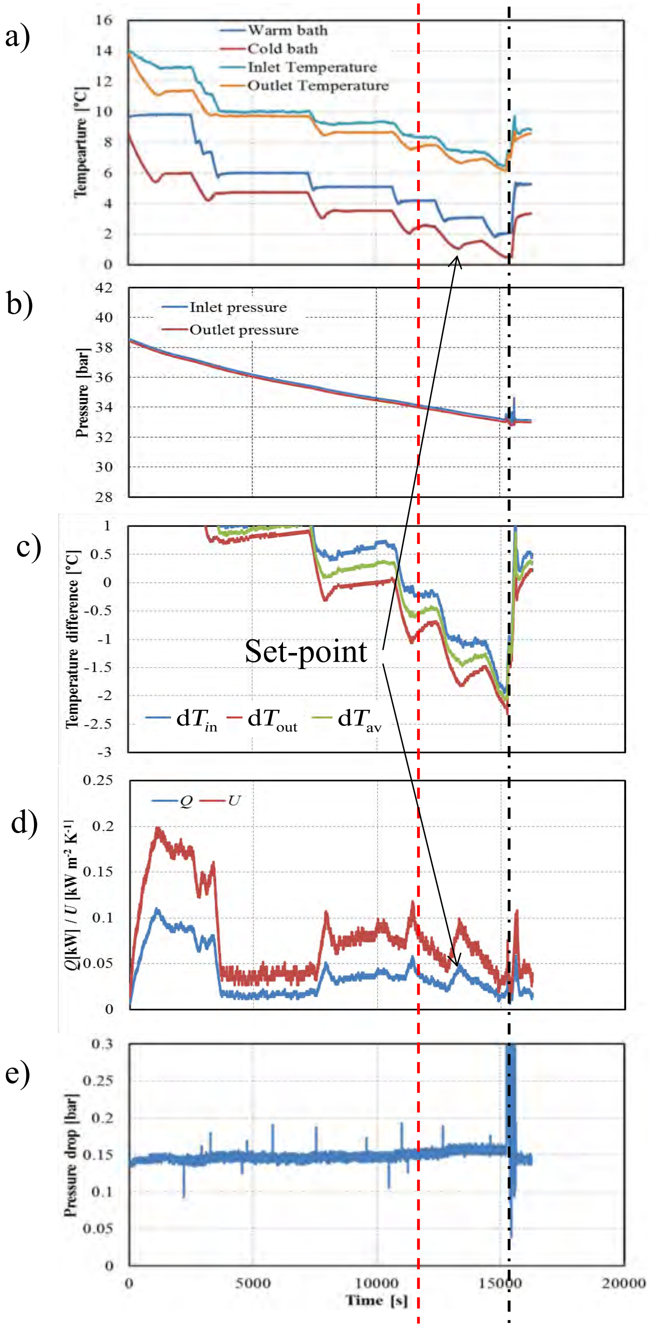

Figure 5.9: Experimental results for water+CO_2+AFPs test during hydrate formation period with solution velocity of 0.56 m/s case 1: a) temperature change, b) pressure change, c) Temperature difference change; d) energy flow/heat transfer coefficient change; e) pressure drop change.

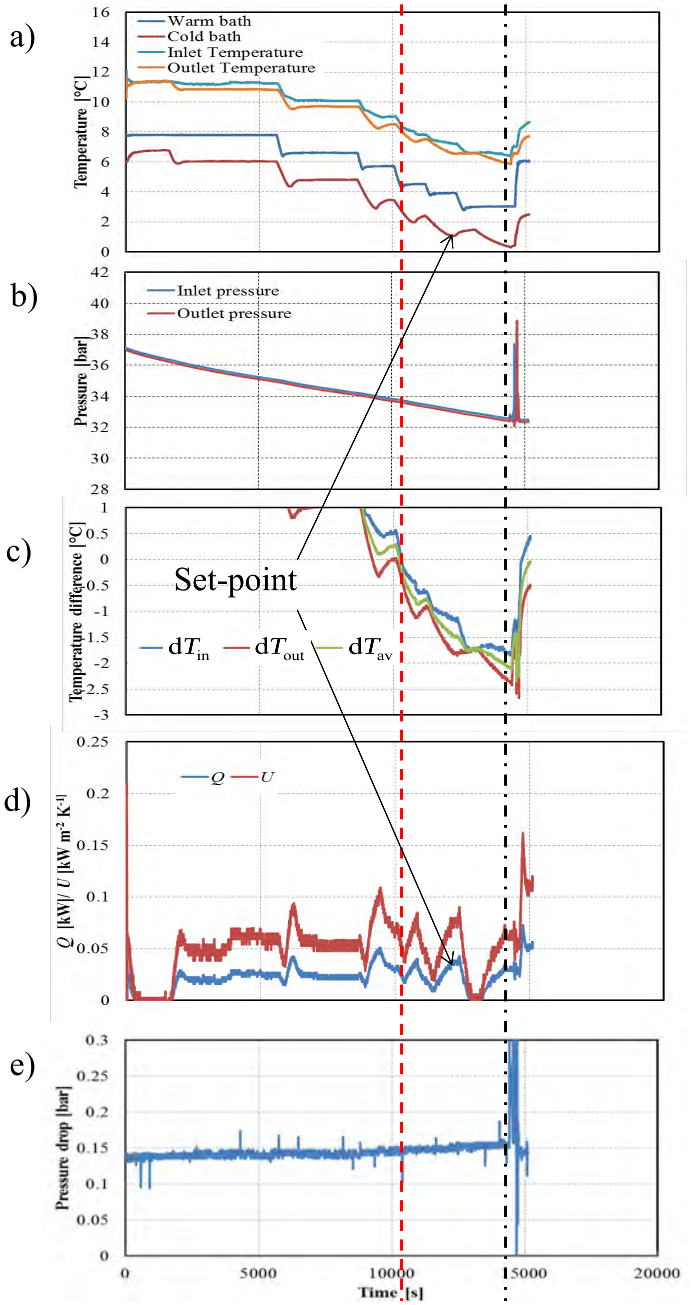

Figure 5.10: Experimental results for water+CO_2+AFPs test during hydrate formation period with solution velocity of 0.56 m/s case 2: a) temperature change, b) pressure change, c) Temperature difference change; d) energy flow/heat transfer coefficient change; e) pressure drop change.

5.3.3. DISSOLUTION OF CO_2 GAS INTO THE AQUEOUS SOLUTION

Before hydrates can be formed, CO_2 gas has firstly to be dissolved into the aqueous solution. Therefore, the dissolution rate of CO_2 also influences the hydrate formation rate to some extent. Experiments for longer time have been conducted to investigate the effect of AFPs on gas dissolution.

Fig. 5.11 shows the experimental density change along with the system pressure for three cases: a) without the addition of AFPs; b) with 10 ppm AFPs; c) with 10 ppm AFPs and longer period. Fig. 5.11a shows that without AFPs, the density of the solution increases when the pressure decreases because of the dissolution of CO_2 into water. The density goes to a constant value within about 33 minutes (2000 seconds); Fig. 5.11b shows that the density doesn't go to a constant value for the whole day experiment (7 hours); Fig. 5.11c shows that the solution reaches saturation only after 7 hours of operation. The effect of the addition of AFPs appears to be limiting the first step in hydrate formation (the dissolution rate is more than 12 times slower): the CO_2 dissolution from gas to the liquid aqueous solution. This corresponds to the assumption of the simplified hydrate growth model of Skovborg and Rasmussen (1994) [101], in which the authors assume the dissolution step to be the limiting step in hydrate formation.

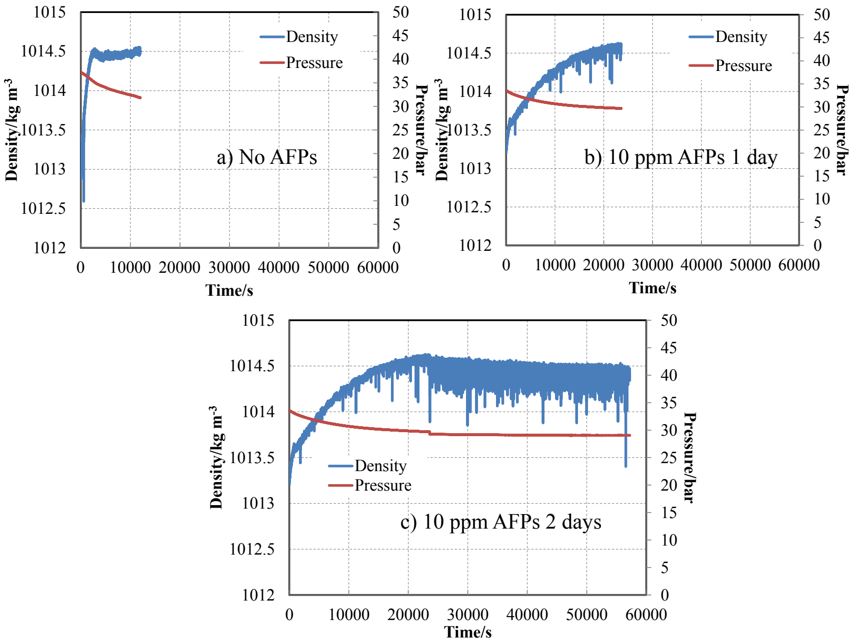

Figure 5.11: Solution density change along with pressure for three different cases: a) No AFPs; b) 10 ppm AFPs; c) 10 ppm AFPs longer period.

5.4. HYDRATE GROWTH RATE

5.4.1. EXPERIMENTAL HYDRATE GROWTH RATE

According to the discussion in section 5.3 when there is no gas refilling taking place, crystals are expected to form on the wall of tube schematically illustrated in Fig. 5.12. Fig. 5.12a shows the cross flow area when a crystal thickness of δ_H is attained. The flow diameter decreases from d_i to d_H. Fig. 5.12b shows a detail of the crystal layer. Equilibrium is assumed at the interface crystal layer / solution. The diffusion layer indicates the region through which CO_2 is transported to the interface. The crystal layer adds an extra thermal resistance. Therefore, when there is hydrate formation, the overall heat transfer coefficient would change according to the equation below

$$\frac{1}{U_H} = \frac{d_i}{d_H}\frac{1}{\alpha_i} + \frac{d_i \ln\frac{d_o}{d_i}}{2\lambda_w} + \frac{d_i \ln\frac{d_i}{d_H}}{2\lambda_H} + \frac{d_i}{d_o}\frac{1}{\alpha_o} \tag{5.4}$$

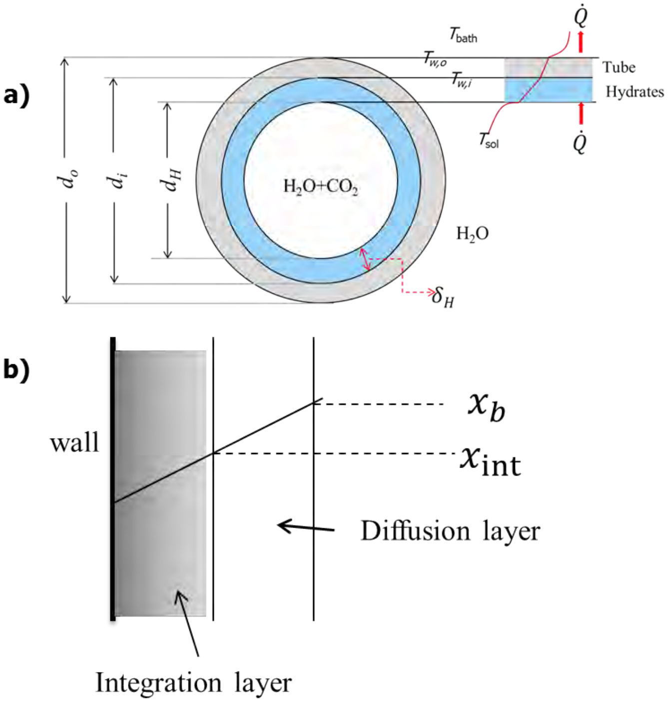

Figure 5.12: a) Hydrates form on the internal wall of the coil, while the generation heat is removed by the external fluid. b) CO_2 diffuses from the bulk liquid to the diffusion layer and integrates in the crystal layer.

In which, the thermal conductivity of CO_2 hydrate solid, λ_w , has been taken as 0.54 W m^{-1} K^{-1} for the relevant temperature range according to the value reported by Sloan and Koh (2008)[102].

The experimental crystal thickness, $\delta_H = (d_i - d_H)/2$, can then be derived from Eqs. (5.1), (5.2) and (5.4) for the cases shown in Fig. 5.7 and Fig. 5.9. Then experimental linear growth rate of crystals can be predicted by Eq. (5.5).

$$G_{\text{lin}} = \frac{d_i - d_H}{2\Delta t} \tag{5.5}$$

Figs. 5.13-5.14 show the overall heat transfer coefficient change as well as the diameter change due to the adherence of crystals to the wall for the two experiments represented in Figs. 5.7 and 5.9 respectively. Fig. 5.13a shows that the deviation of experimental and predicted overall heat transfer coefficient is 25% before hydrates are formed. While the deviation for Fig. 5.14a is larger (40%), indicating the influence of AFP on heat transfer. d_H is then derived taking the deviation of the overall heat transfer coefficient into account. Figs. 5.13b and 5.14b show the change of d_H.The instantaneous increase of the hydrate layer diameter shown in both figures corresponds to the moments illustrated in Figs. 5.7 and 5.9 when the set-point of the thermostatic bath is changed and has no physical meaning. A decrease of 3.3 mm has been reached within 66.7 minutes before a blockage occurred for the case without additive shown in Fig. 5.13b. Fig. 5.14b indicates that a thickness of 0.8 mm has been reached and maintained for a relatively long time (66.7 minutes). This indicates the effect of the addition of AFPs.

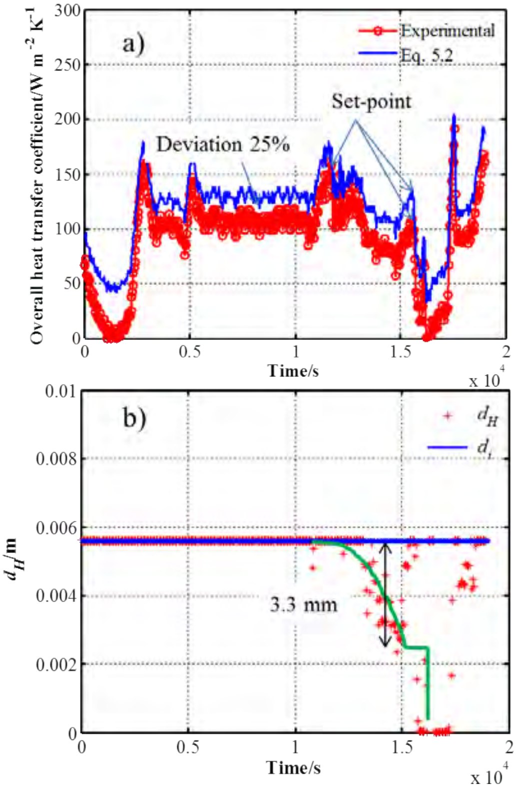

Figure 5.13: a) Comparison of experimental and predicted overall heat transfer coefficient for the case of no addition of AFPs shown in Fig.5.7; b) Diameter change during hydrate formation period.

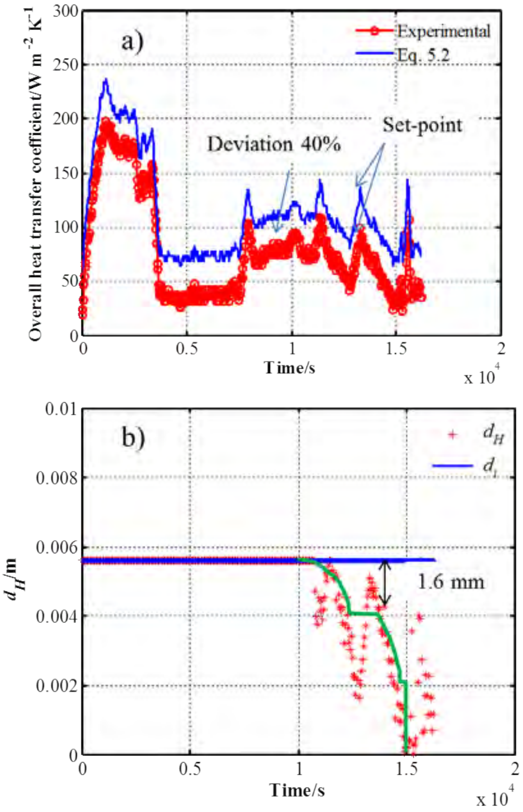

Figure 5.14: a) Comparison of experimental and predicted overall heat transfer coefficient for the case with 10 ppm AFPs shown in Fig.5.9; b) Diameter change during hydrate formation period.

Sabil (2009)[87] studied the kinetic formation of CO_2 hydrate and derived the gas consumption rate. Shen et al. (2016)[97] investigated the kinetic effect of [Py14]-Br on the formation of CO_2 hydrate. An inhibition effect has been determined with lower concentration of [Py14]-Br. The inhibition of AFP and poly (VP/VC) on methane hydrate growth has been investigated by Shadi et al. (2008)[95]. The results from these studies are used for comparison purposes.

Table 5.2 summarizes the influence of AFPs on CO_2 hydrate formation compared with the results from literature. It indicates that the maximum supercooling degree of CO_2 hydrate formation is only slightly influenced by the addition of AFPs. The mass growth rate, G, is derived from Eq. (5.5), $G = G_{\text{lin}} A_H \rho_H$, with the hydrate density of 1036 kg m^{-3}, which is obtained from Zhou et al. (2015)[133]. Results show that the mass growth rate from this research is higher than that reported by Sabil (2009)[87] and Shen et al. (2016)[97]. For one reason, turns in the coils make the formation easier; for another reason, the calculation is based on the whole coil, while in reality it's quite possible that hydrates form on only parts of the coil. In this study the addition of 10 ppm reduces the hydrate formation rate by approximately 35%. With THF, the CO_2 hydrate formation rate is reduced by 27.2% according to Sabil (2009)[87]. With 0.1 wt% [Py-14]-Br, the CO_2 hydrate formation rate decreases by 17.6% according to Shen et al. (2016). Shadi et al. (2008)[95] have investigated the impact of AFP on the methane hydrate growth rate. For a pure methane/water mixture these authors found the growth rate slightly smaller than that reported for CO_2 hydrate. The growth rate is reduced by 38.2% with 70 ppm AFPs addition according to Shadi et al. (2008)[95]. And the effect is similar to that with 35 ppm poly (VP/VC). Comparing the results from this research (10 ppm) and that from Shadi et al. (2008)[95] (70 ppm), the growth rate of hydrate only slightly depends on the concentration of AFPs.

Table 5.2: Experimental hydrate formation results including the supercooling degree and hydrate growth rate. The results are compared with those from other researchers.

Concentration AFPs	dT_{max}	Growth rate kg h^{-1}			
ppm	K	This study	Sabil (2009)[87]	Shen et al. (2016)[97]	Shadi et al.(2008)[95]
0	1.2	0.128	0.0125	0.017	0.011
10	1.9	0.083			
0.1 wt% [Py-14]-Br				0.014	
35 Poly VP/VC					0.0068
70					0.0071

5.4.2. PREDICTION OF CRYSTAL GROWTH

Englezos et al. (1987)[28] developed a gas hydrate growth model based on crystallization and mass transfer theories. According to their model, hydrate growth is a three-step process:1) gas transport from gas phase to the liquid bulk phase; 2) dissolved gas diffuses from the bulk of the solution to the crystal-liquid interface; 3) reaction at the interface, which is an adsorption process describing the incorporation of gas molecules into the cavities of the water structure and the subsequent stabilization of the framework of the structured water.

Skovborg and Rusmussen (1994)[101] simplified the hydrate growth model of Englezos et al. (1987)[28] by assuming that the transport of gas molecules from the gas phase to the liquid phase is the rate-determining step in the hydrate formation process.

In the present experiments it is clear that the dissolution of CO_2 gas into the solution is a slow process as shown in Fig. 5.11. Although hydrate formation can only take place after dissolution, the hydrate formation itself also requires a driving force to take place. In other words, equilibrium dissolution can be attained without the formation of crystals at all, if there is no supersaturation for hydrate formation.

The crystal layer forms along the internal tube wall due to the lower temperature than the bulk solution, and increases to a thickness of δ finally as shown in Fig. 5.12. After that, crystals start flowing into the solution making the solution into a slurry. However, in this work, continuous formation of crystals without blockage could not be maintained for long period (operation was limited to around 4000 s). A general crystal growth equation is applied later to derive the experimental effect of the AFP additive on the gas diffusion rate.

It is expected that the diffusion rate of CO_2 gas in the solution is affected by the addition of AFPs which thereafter influence the formation of hydrates. For this reason, a model similar to the simplified model by Skovborg and Rasmussen (1994)[101] is adopted to derive an equation describing the hydrate growth rate Eq. (5.6). The equation is based on the CO_2 concentration driving force between the bulk liquid phase and the corresponding equilibrium condition at the hydrate interface. The equation is also based on the assumption that the heat transfer resistance around the particle is negligible in comparison with the mass transfer resistance.

$$G = k_L \rho_{\text{sol}} A_H (x_b^{\text{CO}_2} - x_{\text{int}}^{\text{CO}_2}) \tag{5.6}$$

k_l is the mass transfer coefficient of CO_2 gas at the gas-liquid interface. $x_b^{\text{CO}_2}$ is the mole fraction of CO_2 gas in the bulk liquid phase at the operating conditions of the heat exchange. $x_{\text{int}}^{\text{CO}_2}$ is the mole fraction of CO_2 gas in the liquid-crystal layer in equilibrium with the hydrate interface temperature. A_H is the internal hydrate layer area where crystals grow on.

The concentration at the bulk liquid phase, $x_b^{\text{CO}_2}$, can be derived from the equation obtained from Duan and Sun (2003)[25] which relates concentration, pressure and temperature.

$$\begin{aligned} x_b^{\text{CO}_2} = {} & (0.00142T_b^2 - 0.0599T_b - 0.00126T_bP \\ & -0.000859P^2 + 0.11987P + 0.2280)/100. \end{aligned} \tag{5.7}$$

The concentration of CO_2 at the liquid-crystal interface, $x_{\text{int}}^{\text{CO}_2}$, is obtained from Sabil (2009) [87] along the clathrate hydrate equilibrium line.

$$x_{\text{int}}^{\text{CO}_2} = (0.0116T_{\text{int}}^2 - 0.0091T_{\text{int}} + 1.7776)/100 \tag{5.8}$$

Where T in eqs.(5.7) and (5.8) is expressed in °C and P is expressed in bar.

The interface temperature, T_{int} , is the internal wall temperature ($T_{w,i}$) in this study, which could be obtained from the energy flow balance as

$$\begin{aligned}\dot{Q} &= \alpha_i A_i (T_{\text{av}} - T_{w,H}) \\ &= \frac{\lambda_H}{\delta_H} A_H (T_{w,H} - T_{w,i}) \\ &= \frac{\lambda_w}{\delta_w} A_w (T_{w,i} - T_{w,o}) \\ &= \alpha_o A_o (T_{w,o} - T_{\text{bath}})\end{aligned} \tag{5.9}$$

The experimental growth rate can be derived from Eq. (5.5). Combining this equation with eq. (5.6), the experimental mass transfer coefficient can then be obtained.

$$k_L = \frac{G_{\text{lin}} \rho_H}{\rho_{\text{sol}} (x_b^{\text{CO}_2} - x_{\text{int}}^{\text{CO}_2})} \tag{5.10}$$

The results are shown in Table 5.3. It shows that the mass transfer coefficient of CO_2 in the solution is reduced by approximately 21% when there are 10 ppm AFPs added. The results indicate that the addition of AFPs slows down the diffusion rate of CO_2 from bulk liquid phase to the crystal interface. Comparing these mass transfer rates with the dissolution rate, it is evident that the impact of the AFP additive has a significantly larger impact on the dissolution process rather than on the hydrate formation process.

Table 5.3: Experimental mass transfer coefficient with and without the addition of AFPs. The hydrate thickness, δ, and linear hydrate growth rate, G_{lin}, are also shown in the table.

x_{AFPs}	T_b °C	T_{int} °C	x_b mol%	x_{int} mol%	δ m	G_{lin} mm s^{-1}	k_L m s^{-1}
0	7.68	7.48	2.488	2.4358	0.00165	4.125e-4	3.17e-4
10 ppm	8.06	7.91	2.538	2.431	0.0008	2.67e-4	2.49e-4

Blockage is a frequently occurring problem for CO_2 hydrate production. If the addition of AFPs could help to slow down the formation rate, continuous production could be achieved. Unfortunately its effect is not sufficient to allow continuous operation. However, the results of this research, especially how much AFPs are required to slow down the hydrate formation successfully, are important when large crystallizers are to be used for continuous production of CO_2 hydrate.

5.5. CONCLUSIONS

CO_2 hydrates are formed in the solution when there are large amounts of gas bubbles in the bulk solution. However, hydrates will form on the wall of the exchanger when the gas is previously dissolved in the solution.

The supercooling degree of the solution is only slightly affected by the addition of AFPs.

The addition of type-III AFPs significantly slows down the dissolution rate of gas into the solution what can be concluded from the lower solution density increase rate.

A crystal growth equation has been used to predict the effect of AFP on the diffusion of CO_2 from bulk to crystal layer. Results indicate that with the addition of AFPs, the hydrate formation rate is reduced by approximately 35% what corresponds to a decrease of approximately 21% of the mass transfer coefficient.

In summary, with a low concentration of type-III AFPs, the dissolution rate of CO_2 from gas into the solution is significantly slowed down. The diffusivity of CO_2 gas from bulk liquid to the liquid-crystal layer is also limited by the addition of AFP. However, the effect of AFP on the dissolution process is significantly larger than on the diffusion process.

IV

CONCLUSION

6

CONCLUSIONS AND RECOMMENDATIONS

6.1. COLD STORAGE

Energy consumption increases every year and energy shortage becomes urging as a worldwide issue. Air conditioning and refrigeration systems consume large amounts of energy especially in hot areas. It is essential to find solutions to reduce this cooling requirement. Cold storage is generating and storing low temperature heat during low energy requirement time (during night, for example) and making use of the stored cold energy in peak time (day-time). In this way, energy consumption could be leveled out.

Hydrate slurry, which is composed of solids and solution, is a promising candidate for cold storage as well as cold delivery medium for air conditioning systems because of its high latent heat and relatively high fusion temperature. Water is normally used in traditional air conditioning systems in which only sensible heat is utilized. Hydrate slurry air conditioning systems make use of the latent (fusion) heat of the solids. In this way, the cooling capacity per weight of the fluid is significantly increased, thereby, the flow rate of the fluid is significantly reduced. The corresponding power consumption is reduced such as pump power. In addition, the high formation temperature of hydrate allows for the increase of evaporation temperature, which, correspondingly, reduces the power consumption of the compressor.

In this research, two kinds of hydrate slurry, TBAB hydrate slurry and CO_2 hydrate slurry, are investigated as cold storage media, including generation methods, flow and heat transfer characteristics, hydrate growth model development and their applications. The generation of TBAB hydrate slurry is conducted under ambient pressure, for this reason, the application of TBAB hydrate slurry is more attractive than other gas hydrate slurries. CO_2 hydrate slurry makes use of CO_2, which is the major component of green house gases. The melting heat of CO_2 hydrate is about 387 kJ kg^{-1}, which is significantly higher than that of ice. This makes the investigation of CO_2 hydrate slurry a relevant topic.

6.2. HYDRATE PRODUCTION

Three hydrate slurry generators have been introduced and discussed in this thesis: Coil-tube heat exchanger; Plate heat exchanger and Fluidized bed heat exchanger. The first one is the simplest compared with the other two. Compared with the straight tube generator, the use of coil-tube heat exchanger reduces the volume of the generator, which is more flexible for industry. However, it is not always workable for large-scale production. Fluidized bed heat exchanger works better in avoiding solid blockage of the generator according to its working principle discussed in Chapter 4. However, it is not cost-effective because of the complicated construction. A plate heat exchanger, which is more popular in industry than fluidized bed generator, is utilized in this research for a real TBAB hydrate slurry air conditioning system that has been discussed in Chapter 3.

The generator is always a large investment for hydrate slurry industrial applications. In order to use simple and cheap generators (such as coil tube exchanger rather than the other two), Antifreeze Proteins (AFPs) which have been proved to be ice growth preventers have been investigated. Results show that AFPs are able to slow down the growth rate of CO_2 hydrate by decreasing the diffusion rate of CO_2 from aqueous solution to the interface of liquid-crystal. In addition, AFPs are non-poisonous and environment friendly which enable their addition in future industrial applications.

By using a coil tube heat exchanger, operation with up to 40 wt% TBAB hydrate concentration of slurry can be maintained. However, CO_2 hydrate slurry can not be maintained for a long time with this heat exchanger. The addition of AFPs helps but still does not give a good result yet. With a fluidized bed heat exchanger, up to 35 wt% CO_2 hydrate slurry can be maintained with continuous removal of slurry.

6.3. MODEL DEVELOPMENT AND VALIDATION

The model developed by Pronk [84] for ice growth in a fluidized bed heat exchanger has been adopted in this thesis for both CO_2 and TBAB hydrate production. The application of this model for CO_2 and TBAB hydrate formation in the coil tube and plate heat exchanger individually assumes crystals form on the heat exchanger wall. With the increasing thickness of the crystal layer, the drag force from the fluid increases, when the drag force is enough, crystals formed on the wall are taken away to the solution. The model for CO_2 hydrate production in a fluidized bed heat exchanger takes no consideration of crystal layer on the exchanger wall as the stainless steel particles circulating in the heat exchanger remove away the formed crystals on the wall continuously.

The model indicates that the growth rate of hydrate depends on a driving force between the aqueous solution and the liquid-crystal surface. The model also shows that the hydrate growth rate is controlled by the mass transfer rate of the solute from the liquid solution to the liquid-solid interface. This phenomenon is also proved by the investigation of AFPs on preventing CO_2 hydrate growth which indicates the effect of AFPs is on the diffusion rate of CO_2 from bulk liquid to the crystal layer.

Heat transfer characteristic during hydrate generation has also been investigated. The transport properties of hydrate slurry have been investigated which has made clear that slurry is more viscous than water. Results also indicate that hydrate slurry above a certain solid concentration is a non-Newtonian fluid.

6.4. HYDRATE SLURRY APPLICATION

The advantage of hydrate slurry as cold storage medium has been presented in the introduction part. In Chapter 3, an air conditioning system for a small space which makes use of TBAB hydrate slurry as cooling medium is investigated. An energy saving of 73.5% has been predicted by using TBAB slurry, which results a reduction of CO_2 emission correspondingly. Chapter 4 describes the production and the possibility of the application of CO_2 hydrate slurry in air conditioning systems. The results show a possibility of a significant improvement (43%) of the coefficient of performance (COP) of the air conditioning system which makes use of CO_2 hydrate slurry compared with the conventional air conditioning systems.

In addition, the advantage of using hydrate slurry is more obvious when it is combined with a cold thermal energy storage system.

6.5. RECOMMENDATIONS

The generator is the most important component for the application of hydrate slurry in air conditioning systems. For CO_2 hydrate slurry there is no best generator found from this research, as the price of AFPs discussed in Chapter 5 is quite expensive. Therefore, it’s still necessary to look for new additives or new generators for the production of CO_2 hydrate slurry.

The control system is also important for the successful production. Especially the evaporating temperature needs to be accurately controlled.

APPENDIX A

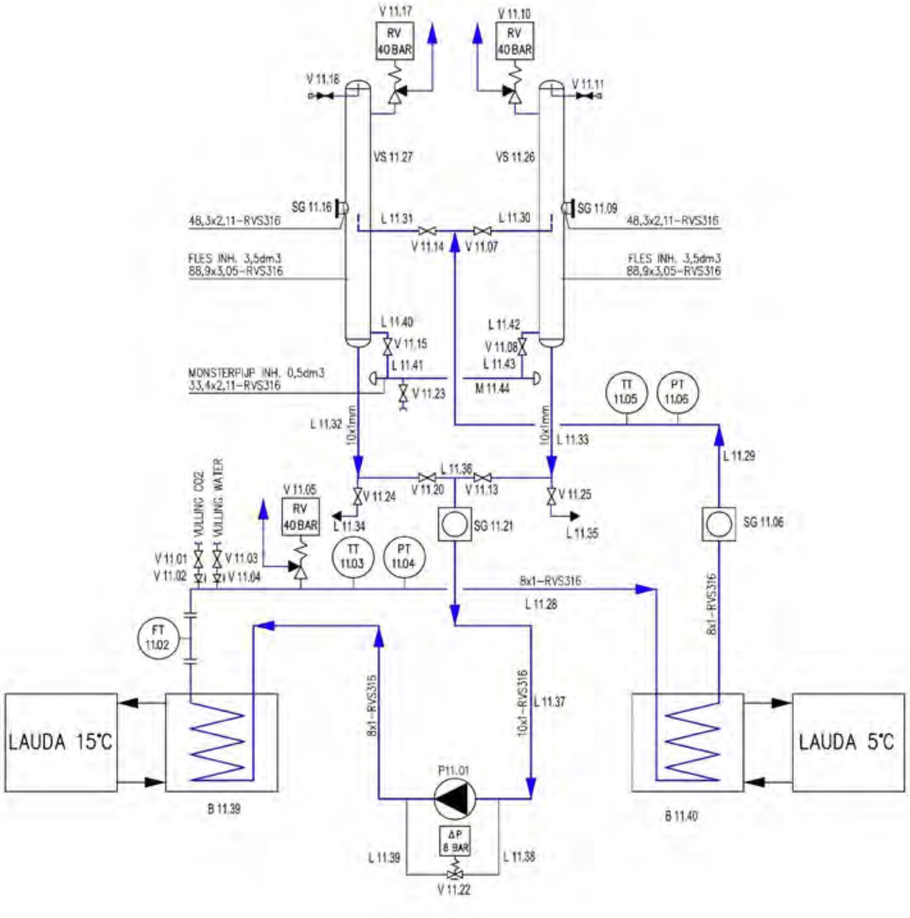

Figure 1: Process flow diagram of the system discussed in Chapter 2 and Chapter 5, including coil-tube heat exchangers in the two thermo-static baths (LAUDA), a gear pump for circulation, two vessels made of stainless steel which are insulated during the experiments conducted in this thesis.

APPENDIX B

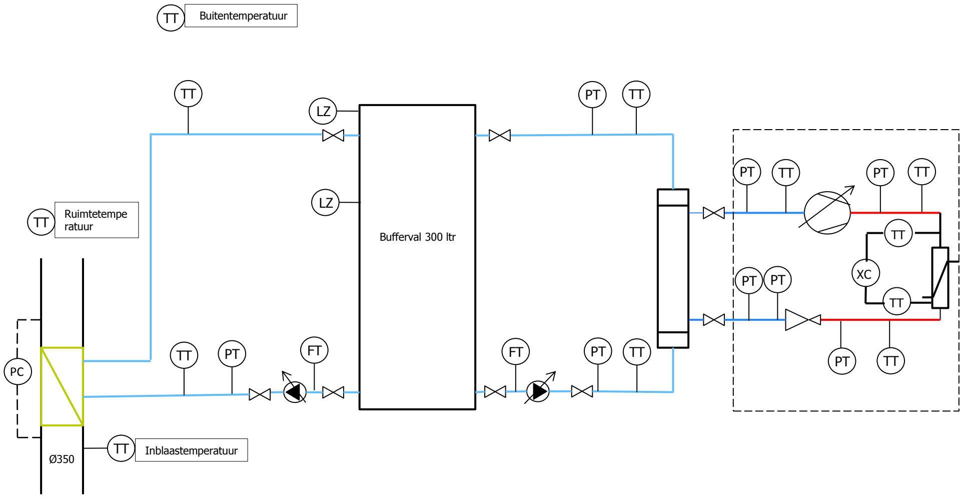

Figure 2: Process flow diagram of the system discussed in Chapter 3, including a tube-fin air-cooler, a plate heat exchanger for TBAB hydrate slurry generation, and a 300 L storage tank.

APPENDIX C

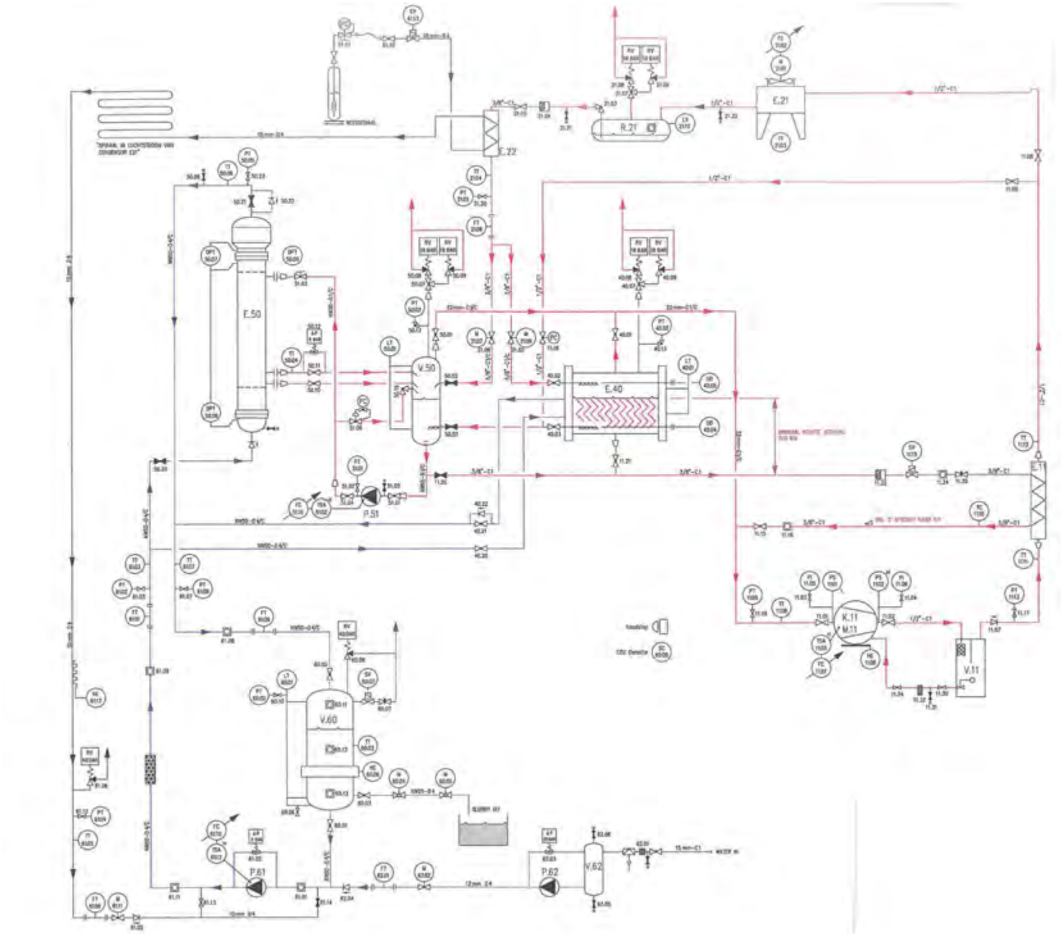

Figure 3: Process flow diagram of the system discussed in Chapter 4, containing a fluidized bed CO_2-hydrate generator and a CO_2-hydrate slurry cold storage vessel (V60). During the experiments reported in Chapter 4, the FBHE (E50) was used as generator. The system also includes a shell-and-plate generator (E40) which was not used during the experiments reported in this thesis

APPENDIX D

The effect of the addition of higher concentrations of AFPs (20 ppm - 50 ppm) is shown in this appendix.

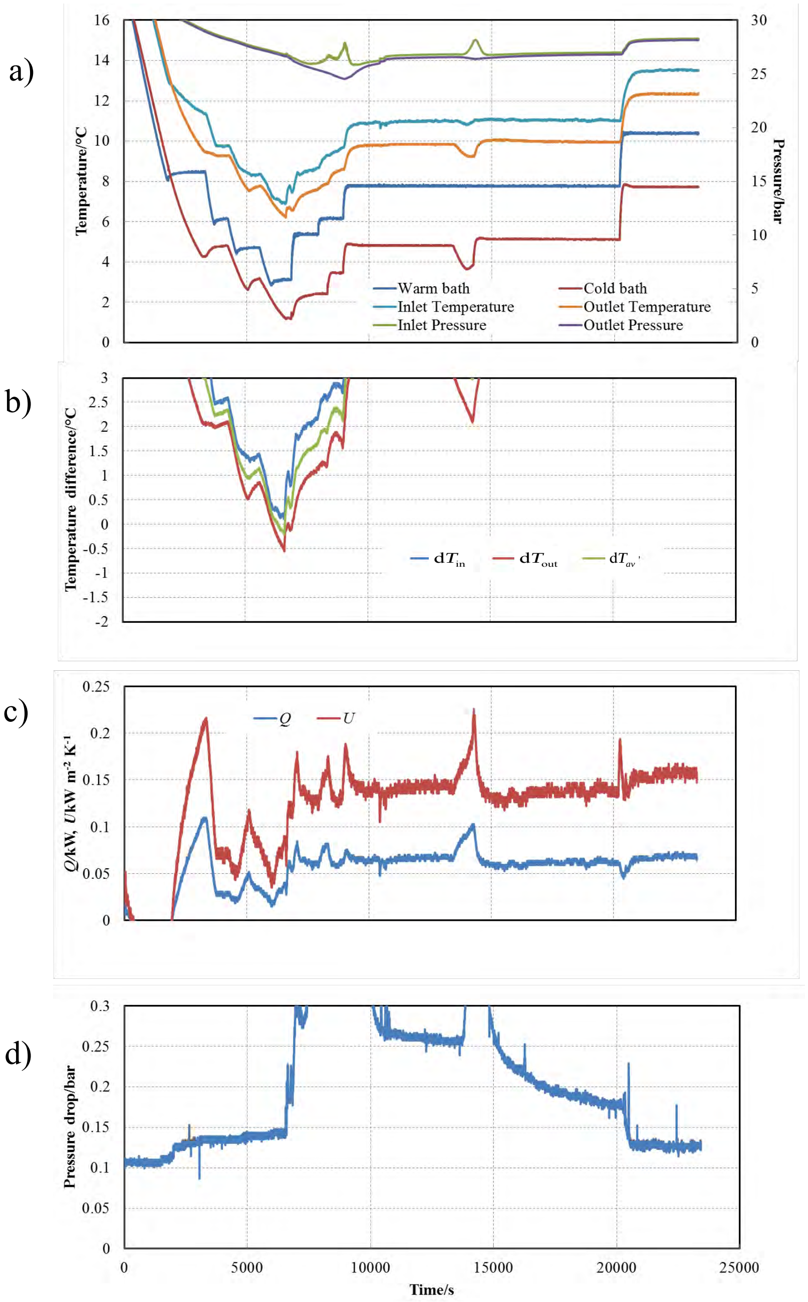

Figure 4: Experimental results for water+CO_2+AFPs (20 ppm) test including: a) temperature/pressure profile, b) supercooling degree, c) energy flow/heat transfer coefficient and d) pressure drop changes during hydrate formation period.

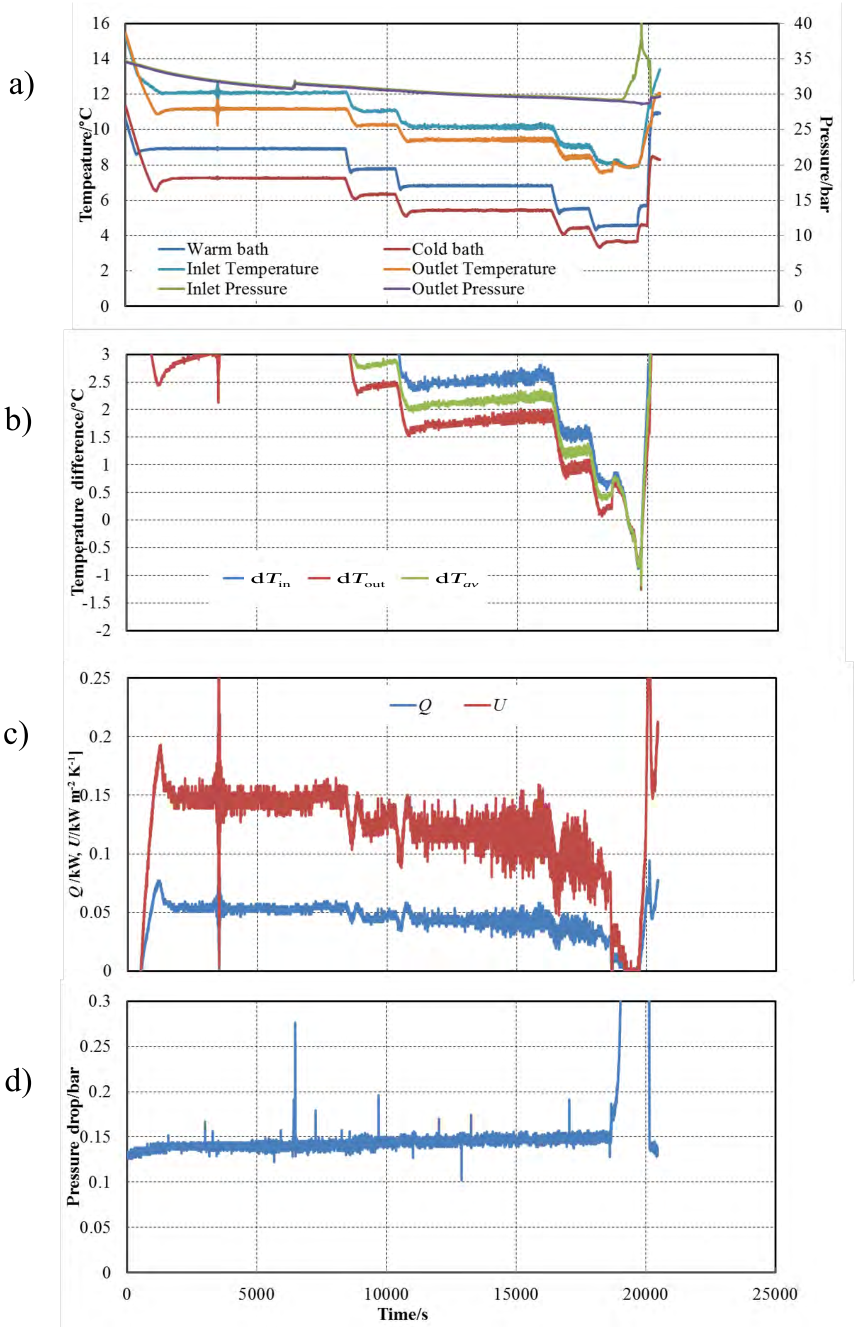

Figure 5: Experimental results for water+CO_2+AFPs (30 ppm) test including: a) temperature/pressure profile, b) supercooling degree, c) energy flow/heat transfer coefficient and d) pressure drop changes during hydrate formation period.

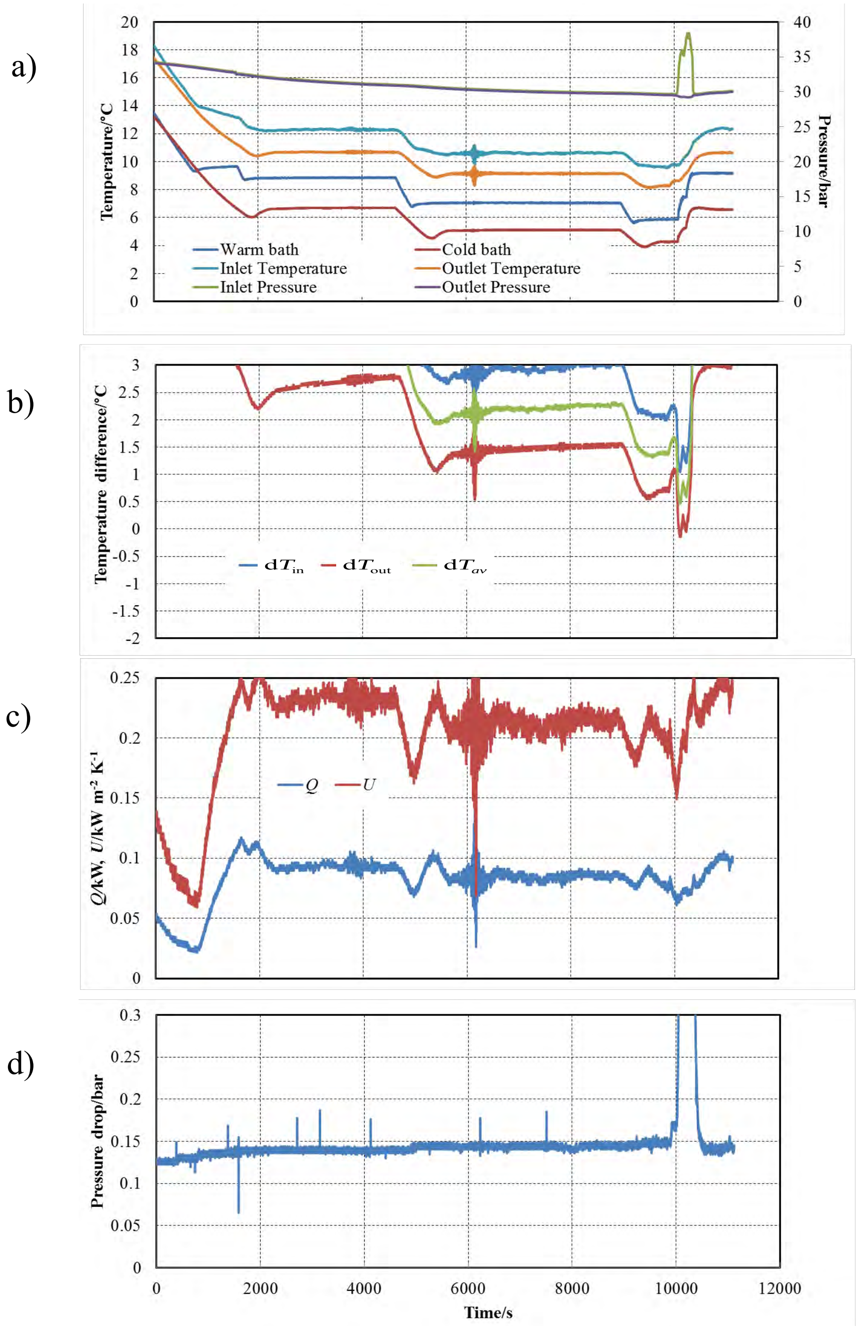

Figure 6: Experimental results for water+CO_2+AFPs (40 ppm) test including: a) temperature/pressure profile, b) supercooling degree, c) energy flow/heat transfer coefficient and d) pressure drop changes during hydrate formation period.

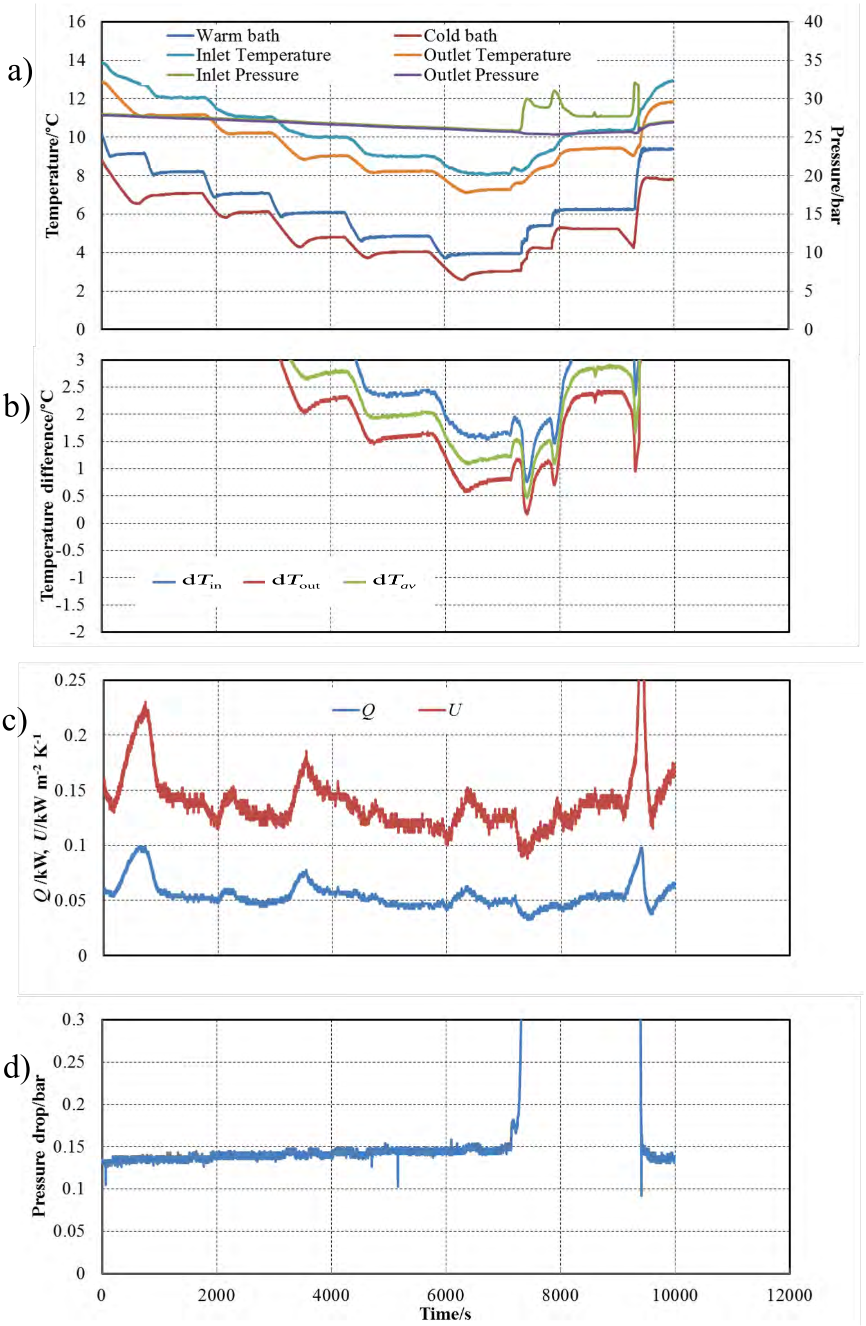

Figure 7: Experimental results for water+CO_2+AFPs (50 ppm) test including: a) temperature/pressure profile, b) supercooling degree, c) energy flow/heat transfer coefficient and d) pressure drop changes during hydrate formation period.

SUMMARY

From the results shown above for the concentrations of 20 ppm to 50 ppm AFPs, the temperature difference, $dT = T_{\mathrm{sol}} - T_{\mathrm{sat}}$, increases from 0.2 °C to about 2 °C.

The temperature difference is positive in the concentration range 20 - 50 ppm, indicating the possible equilibrium change when more than 20 ppm AFPs is added. Because of this, the hydrate growth rate can not be predicted with the equation used in Chapter-5.

The energy flow change as well as the pressure drop change along the hydrate formation period is similar as that 0-10 ppm which has been shown in Chapter 5.

REFERENCES

[1] A. Abhat. Low temperature latent heat thermal energy storage: heat storage materials. *Solar Energy*, 30:313–332, 1983.

[2] M.M. Abu-Khader. Plate heat exchangers-recent advances. *Renewable and Sustainable Energy Reviews*, 16:1883–1891, 2012.

[3] S. Adisasmito, R.J. Frank, and E.D. Sloan. Hydrates of carbon dioxide and methane mixtures. *Chemical & Engineering Data*, 36:68–71, 1991.

[4] F. Agyenim, N. Hewitt, P. Eames, and M. Smyth. A review of materials, heat transfer and phase change problem formulation for latent heat thermal energy storage systems (LHTESS). *Renewable and Sustainable Energy Reviews*, 14:615–628, 2010.

[5] M. Akiyama and K.C. Cheng. Boundary velocity method for laminar forced convection heat transfer in curved pipes. *International Journal of Heat and Mass Transfer*, 14:1659–1675, 1971.

[6] M. Ali. Experimental investigation of natural convection from vertical coiled tubes. *International Journal of Heat and Mass Transfer*, 37:665–671, 1994.

[7] Y. Allouche, S. Varga, C. Bouden, and A.C. Oliveira. Experimental determination of the heat transfer and cold storage characteristics of a microencapsulated phase change material in a horizontal tank. *Energy Conversion and Management*, 94:275–285, 2015.

[8] A.A. Antson, D.J. Smith, D.I. Roper, S. Lewis, L.S.D. Caves, C.S. Verma, S.L. Buckley, P.J. Lillford, and R.E. Hubbard. Understanding the mechanmism of ice binding by type iii antifreeze proteins. *Journal of Molecular Biology*, 305:875–889, 2001.

[9] T. Asaoka, H. Kumano, and M. Serita. Measurement of latent heat of tetra-n-butyl ammonium bromide. *International Journal of Refrigeration*, 36:992–997, 2013.

[10] S.A. Bagherzadeh, S. Alavi, and J.A. Ripmeester. Why ice binding type I antifreeze protein acts as a gas hydrate crystal inhibitor. *Physical Chemistry Chemical Physics*, 17:9984–9990, 2015.

[11] A.T. Bozzo, H.S. Chen, J.R. Kass, and A.J. Barduhn. The proprieties of hydrate of chlorine and carbon dioxide. *Desalination*, 16:303–320, 1975.

[12] Y.J. Cai, S. Liu, X.R. Liao, Y.R. Ding, J. Sun, and D.B. Zhang. Purification and partial characterization of antifreeze proteins from leaves of ligustrum lucidum ait. *Food and bioproducts processing*, 89:98–102, 2011.

[13] Y. Celik, L.A. Graham, Y.F. Mok, M. Bar, P.L. Davies, and I. Braslavsky. Superheating of ice crystals in antifreeze protein solutions. In *Proceedings of the National Academy of Science*, volume 107, pages 5423–5428, USA, 2010.

[14] K. Christensen and M. Kauffeld. Heat transfer characteristics in compact scraped surface ice slurry generators. In *International conference of Heat transfer Issues in Natural Refrigerants*, College Park, United States. International Institute of Refrigeration.

[15] S.W. Churchill and H.H.S. Chu. Correlating equations for laminar and turbulent free convection from a horizontal cylinder. *International Journal of Heat and Mass Transfer*, 18:1049–1053, 1975.

[16] A. de Gracia and L.F. Cabeza. Phase change materials and thermal energy storage for buildings. *Energy and Buildings*, 103:414–419, 2015.

[17] I.E.E. de Sera, H. Zhou, and C.A. Infante Ferreira. *Food Future Project Internal report: Experimental study on the continuous production of CO_2 hydrate slurry.* TU Delft, The Netherlands, 2014.

[18] L. Diamond and N. Akinfiev. Solubility of CO_2 in water from 1.5 to 100 °C and from 0.1 to 100 MPa: evaluation of literature data and thermodynamic modelling. *Fluid Phase Equilibria*, 208:265–290, 2003.

[19] I. Dincer. On thermal energy storage systems and applications in buildings. *Energy & Buidings*, 34:377–388, 2002.

[20] I. Dincer, S. Dost, and X.G. Li. Performance analyses of sensible heat storage systems for thermal applications. *Internal Journal of Energy Resource*, 21:1157–1171, 1997.

[21] I. Dincer and M.A. Rosen. Energetic, environmental and economic aspects of thermal energy storage systems for cooling capacity. *Applied Thermal Engineering*, 21:1105–1117, 2001.

[22] V. Donowski and S.G. Kandlikar. Correlating evaporation heat transfer coefficient of refrigerant R134a in a plate heat exchanger. In *Proceeding: Boiling 2000: Phenomena and Emerging Applications*, Alaska, 30 April - 5 May 2000.

[23] A.N. Dravid, K.A. Smith, E.W. Merrill, and P.L.T. Brain. Effect of secondary fluid on laminar flow heat transfer in helically coiled tubes. *AIChE*, 17:1114–1122, 1971.

[24] Z. Duan, J. Hu, D. Li, and S. Mao. Densities of the CO_2/H_2O and $CO_2/H_2O/NaCl$ systems up to 647 K and 100 MPa. *Energy and Fuels*, 22:1666–1674, 2008.

[25] Z.H. Duan and R. Sun. An improved model calculating CO_2 solubility in pure water and aqueous nacl solutions from 273 to 533 k and from 0 to 2000 bar. *Chemical Geology*, 193:257–271, 2003.

[26] H. Ebeltoft, Statoil, and M. Yousif. Hydrate control during deep water drilling: Overview and new drilling fluids formulations. In *SPE Annual Technical Conference and Exhibition*, San Antonio, Texas, 1997.

[27] D.K. Edwards, V.E. Denny, and A.F. Mills. *Transfer Processes*. Hemisphere, Washington D.C., 2nd ed edition, 1979.

[28] P. Englezos, N.E. Kalogerakis, P.D. Dholabhai, and P.R. Bishnoi. Kinetics of formation of methane and ethane gas hydrates. *Chemical Engineering Science*, 42:2647–2658, 1987.

[29] Z. Fan, C.A. Infante Ferreira, and A.H. Mosaffa. Numerical modelling of high temperature latent heat thermal storage for solar application combing with double-effect H_2O/LiBr absorption refrigeration system. *Solar Energy*, 110:398–409, 2014.

[30] G.Y. Fang, F. Tang, and L. Cao. Dynamic characteristics of cool thermal energy storage systems—a review. *Journal of Green Energy*, 13:1–13, 2016.

[31] M.M. Farid, A.M. Khudhair, S.K. Razack, and S. Al-Hallaj. A review on phase change energy storage: materials and applications. *Energy Conversion and Management*, 45:1597–1615, 2004.

[32] T. Fernando and M.A. Kelland. First investigation of the kinetic hydrate inhibitor performance of polymers of alkylated N-vinyl pyrrolidones. *Energy Fuels*, 27:3730–3735, 2013.

[33] Y.M. Ferng, W.C. Lic, and C.C. Chieng. Numerically investigated effects of difference dean number and pitch size on flow and heat transfer characteristics in a helically coil tube heat exchanger. *Applied Thermal Engineering*, 36:378–385, 2012.

[34] L. Fournaison, A. Delahaye, I. Chatti, and J.P. Petitet. CO_2 hydrates in refrigeration processes. *Industrial and Engineering Chemistry Research*, 43, 2004.

[35] A.M. Fsadni and J.P.M. Whitty. A review on the two-phase pressure drop characteristics in helically coiled tubes. *Applied Thermal Engineering*, 103:616–638, 2016.

[36] K. Futagami and Y. Aoyama. Laminar heat transfer in helically coiled tubes. *International Journal of Heat and Mass Transfer*, 31:387–396, 1988.

[37] V. Gnielinski. New equations for heat and mass transfer in turbulent pipe and channel flow. *Chemical Engineering*, 16:359–368, 1976.

[38] V. Gnielinski. Heat transfer in helically coiled tubes. In *VDI Heat Atlas, second edition*. Springer-Verlag, Berlin Heidelberg, 2010.

[39] V. Gudjonsdottir. Analysis of external influences on an OTEC cycle. Master thesis, TU Delft, The Netherlands, 2015.

[40] M. Haid. Correlations for the prediction of heat transfer to liquid-solid fluidized beds. *Chemical Engineering and Processing*, 36:2454–2462, 1997.

[41] D.H. Han, K.J. Lee, and Y.H. Kim. Experiments on the characteristics of evaporation of R410A in brazed plate heat exchangers with different geometric configurations. *Applied Thermal Engineering*, 23:1209–1225, 2003.

[42] Naoki Hara. New japanese chs thermal energy storage air conditioning systems aim for cross border energy conservation. *IIST World Forum*, 2010.

[43] H. Hayashi, S. Takao, H. Ogaoshi, and S. Matsumoto. Research and development on high-density cold latent-heat medium transportation technology. *Workshop of Annex 10 ECES IA, International Energy Agency*, 2000.

[44] IEA. International Energy Agency. *Key World Energy Statistics*, 2014.

[45] C.A. Infante-Ferreira. *MSc course wb4427-Refrigeration Technology and Application*. TU Delft, The Netherlands.

[46] L.A.A. Janssen and C.J. Hoogendoorn. Laminar convective heat transfer in helical coiled tubes. *International Journal of Heat and Mass Transfer*, 21:1197–1206, 1978.

[47] J.S. Jayakumara, S.M. Mahajania, J.C. Mandala, P.K. Vijayanb, and R. Bhoia. Experimental and CFD estimation of heat transfer in helically coiled heat exchangers. *Chemical Engineering Resource Des*, 86:221–232, 2008.

[48] S. Jerbi, A. Delahaye, L. Fournaison, and P. Haberschill. Characterization of CO_2 hydrate formation and dissociation kinetics in a flow loop. *International Journal of Refrigeration*, 33:1625–1631, 2010.

[49] C. E. Kalb and J.D. Seader. Heat and mass transfer phenomena for viscous flow in curved circular tubes. *International Journal of Heat and Mass Transfer*, 15:801–817, 1972.

[50] W. Kast and H. Nirschl. Pressure drop in single phase flow in pipes. In *VDI Heat Atlas, second edition*. Springer-Verlag, Berlin Heidelberg, 2010.

[51] M. Kauffeld, K.G. Christensen, S. Lund, and T.M. Hansen. Experience with Ice Slurry. In *Proceedings of 1st workshop on Ice Slurries*, pages 42–73, YverdonlesBains, Switzerland, 1999. IIR.

[52] M.A. Kelland, S. Thor, T. Tomita, and K. Mizuta. Studies on some alkylamide surfactant gas hydrate anti-agglomerants. *Chemical Engineering Science*, 61:4290–4298, 2006.

[53] D.G. Klaren and J.S. Van-der Meer. A fluidized bed chiller: a new approach in making slush ice. In *Industrial Energy technology conference Houston Proceedings*, Texas A & M University, 1991.

[54] H. Kumano, T. Hirata, and Y. Kobayashi. Flow and heat transfer characteristics of a tetra-n-butyl ammonium bromide hydrate slurry in the transition region. *International Journal of Refrigeration*, 35:2085–2092, 2012.

[55] H Kumano, T. Hirata, and T. Kudoh. Experimental study on the flow and heat transfer characteristics of a tetra-n-butyl ammonium bromide hydrate slurry (first report: Flow characteristics). *International Journal of Refrigeration*, 34:1953–1962, 2011a.

[56] H Kumano, T. Hirata, and T. Kudoh. Experimental study on the flow and heat transfer characteristics of a tetra-n-butyl ammonium bromide hydrate slurry (second report: Heat transfer characteristics). *International Journal of Refrigeration*, 34:1963–1971, 2011b.

[57] B. Kutschan, K Morawetz, and S. Thoms. Dynamical mechanism of antifreeze proteins to prevent ice growth. *Physical Review E*, 90:022711, 2014.

[58] G.A. Lane. *Solar heat storage: latent heat materials*, volume 2. USA CRC, Boca Raton, 1985.

[59] E.W. Lemmon, M.L. Huber, and M.O. McLinden. NIST standard reference database 23: Reference fluid thermodynamic and transport properties-refprop, version 9.0. 2013.

[60] C. Lirio and F. Pessoa. Enthalpy of dissociation of simple and mixed carbon dioxide clathrate hydrate. *Chemical Engineering Transactions*, 32:577–582, 2013.

[61] R.W. Lockhart and R.C. Martinelli. Proposed correlation of data for isothermal two-phase, two-component flow in pipes. *Chemical Engineering Progress*, 45:39–48, 1949.

[62] G.A. Longo and A. Gasparella. Refrigerant R134a vaporisation heat transfer and pressure drop inside a small brazed plate heat exchanger. *International Journal of Refrigeration*, 30:821–830, 2007.

[63] W. Lu, H. Guo, I.M. Chou, R.C. Burruss, and L. Li. Determination of diffusion coefficients of carbon dioxide in water between 268 and 473 K in a high-pressure capillary optical cell with in situ Raman spectroscopic measurements. *Geochimica et Cosmochimica Acta*, 115:183–204, 2013.

[64] Z.W. Ma and P. Zhang. Pressure drop and heat transfer characteristics of clathrate hydrate in a plate heat exchanger. *International Journal of Refrigeration*, 34:796–806, 2011.

[65] Z.W. Ma and P. Zhang. Pressure drop and heat transfer characteristics of tetra-n-butyl ammonium bromide clathrate hydrate slurry during flow melting and generating in a double-tube heat exchanger. *Experimental Thermal Fluid Science*, 44:227–234, 2013a.

[66] Z.W. Ma and P. Zhang. Influence of crystal layer on the flow and heat transfer characteristics during TBAB CHS generation in a double-tube heat exchanger. *International Journal of Thermal Science*, 68:173–180, 2013b.

[67] Z.W. Ma, P. Zhang, R.Z. Wang, S. Furui, and G.N. Xi. Forced flow and convective melting heat transfer of clathrate hydrate slurry in tubes. *International Journal of Heat and Mass Transfer*, 53:3745–3757, 2010.

[68] T.C.W. Mak and R.K. Mcmullan. Polyhedral clathrate hydrates x. structure of the double hydrate of tetrahydrofunan and hydrogen sulfide. *Chemical Physics*, 42:2732–2737, 1965.

[69] S. Marinhas, A. Delahaye, L. Fournaison, D. Dalmazzone, W. Furst, and J-P. Petitet. Modelling of the available latent heat of a CO_2 hydrate slurry in an

experimental loop applied to secondary refrigeration. *Chemical Engineering and Processing*, 45:184–192, 2006.

[70] R.K. Mcmullan and G.A. Jeffery. Polyhedral clathrate hydrates ix structure of ethylene oxide hydrate. *The Journal of Chemical Physics*, 42(8), 1965.

[71] J.W. Meewisse. *Fluidized Bed Ice Slurry Generator for Enhanced Secondary Cooling Systems*. Phd thesis, Delft University of Technology, 2004.

[72] A.B. Metzner and J.C. Reed. Flow of non-newtonian fluids-correlation of the laminar, transition, and turbulent-flow regions. *AIChE*, 1:434–440, 1955.

[73] P.A. Mirzaei and F. Haghighat. Modeling of phase change materials for applications in whole building simulation. *Renewable and Sustainable Energy Reviews*, 16:5355–5362, 2012.

[74] M.M. Mooijer-van den Heuvel, R. Witteman, and C.J. Peters. Phase behavior of gas hydrates of carbon dioxide in the presence of tetrahydropyran, cyclobutanone, cyclohexane and methylcyclohexane. *Fluid Phase Equilibria*, 182:97–110, 2001.

[75] P. Naphon and S. Wongwises. A review of flow and heat transfer characteristics in curved tubes. *Renewable Sustainable Energy Review*, 10:463–390, 2006.

[76] H.J. Ng and D.B. Robinson. Hydrate formation in systems containing methane, ethane, propane, carbon dioxide or hydrogen sulphide in the presence of methanol. *Fluid Phase Equilibria*, 21:145–155, 1985.

[77] D.N. Nkwetta and F. Haghighat. Thermal energy storage with phase change material-a state of the art review. *Sustainable cities and society*, 10:87–100, 2014.

[78] H. Ogoshi and S. Takao. Air-conditioning system using clathrate hydrate slurry. *JFE technical report*, (3):1–5, 2004.

[79] K. Ohgaki, Y. Makihara, and K. Takano. Formation of CO_2 hydrate in pure and sea waters. *Journal of Chemical Engineering of Japan*, 26:558–564, 1993.

[80] E. Oró, A. de Gracia, A. Castell, M.M. Farid, and L.F. Cabeza. Review on phase change materials (PCMs) for cold thermal energy storage applications. *Applied Energy*, 99:513–533, 2012.

[81] H. Oyama, W. Shimada, T. Ebinuma, Y. Kamata, S. Takeya, T. Uchida, J. Nagao, and H. Narita. Phase diagram, latent heat and specific heat of TBAB semi-clathrate hydrate crystals. *Fluid Phase Equilibrium*, 234:131–135, 2005.

[82] L Perez-Lombard, J. Ortiz, and C. Pout. A review on buildings energy consumption information. *Energy & Building*, 40:394–398, 2008.

[83] K. Pielichowska and K. Pielichowski. Phase change materials for thermal energy storage. *Material Science*, 65:67–123, 2014.

[84] P. Pronk. *Fluidized bed heat exchangers to prevent fouling in ice slurry systems and industrial crystallizers.* Phd thesis, Technology University of Delft, The Netherlands, 2006. URL:http://repository.tudelft.nl/islandora/object/uuid:e2cf9ec0-fedc-4480-a8ab-ddf7a3a7afea?collection=research.

[85] R.E. Raj, Z.R. Kennedy, and B.C. Pillai. Optimization of process parameters in flash pyrolysis of waste tyres to liquid and gaseous fuel in a fluidized bed reactor. *Energy Conversion and Management*, 67:145–151, 2013.

[86] J. Ramon, J.A. Medrana, F. Bimbela, L. Garcia, and J. Arauzo. Ni/Al-Mg-O solids modified with Co or Cu for the catalytic steam reforming of bio-oil. *Applied Catalysis B: Environmental*, 132-133:433–444, 2013.

[87] K. Sabil. *Phase Behaviour, Thermodynamics and Kinetics of Clathrate Hydrate Systems of Carbon Dioxide in Presence of Tetrahydrofuran and Electrolytes.* Phd thesis, Technology University of Delft, The Netherlands, 2009.

[88] H. Sakaguchi, R. Ohmura, and Y. Mori. Effects of kinetic inhibitors on the formation and growth of hydrate crystals at a liquid-liquid interface. *Journal of Crystal Growth*, 2003.

[89] O. Sari, J. Hu, S. Eicher, P. Egolf, and P. Homsy. Thermo physical and flow properties of CO_2 hydrate slurry. In *Proceedings of the 8th IIR Gustav Lorentzen Conference on Natural Working Fluids*, Copenhagen, 2008.

[90] K.G. Schmidt. Heat transfer to finned tubes. In *VDI Heat Atlas*. Springer-Verlag, Duisburg, Germany, 2010.

[91] S. Schmidt, J. Buchs, C. Born, and M. Biselli. A new correlation for the wall-to-fluid mass transfer in liquid-solid fluidized beds. *Chemical Engineering Science*, 54:829–839, 1999.

[92] T.E. Schmidt. *Die Warmeleistung berippter Oberflachen.* Deutscher Kaltetechnischer Verein, Heft 4, C.F. Muller Verlag, Karlsruhe, 1950.

[93] G. Schnabel. Heat transfer to falling films at vertical surfaces. In *VDI Heat Atlas*. Springer-Verlag, Berlin Heidelberg, 2010.

[94] J.D. Seader and E.J. Henley. Separation process principle. *John Wiley Sons*, 2006.

[95] AI-Adel Shadi, A.G. D. John, E.G. Rasha, and S. Phillip. The effect of biological and polymeric inhibitors on methane gas hydrate growth kinetics. *Fluid Phase Equilibria*, 267:92–98, 2008.

[96] A. Sharma, VV. Tyagi, C.R. Chen, and D. Buddhi. Review on thermal energy storage with phase change materials and applications. *Renewable and Sustainable Energy Reviews*, 13:318–345, 2009.

[97] X.D. Shen, L.L. Shi, Z. Long, X.B. Zhou, and D.Q. Liang. Experimental study on the kinetic effect of n-butyl-n-methylpyrrolidinium bromide on CO_2 hydrate. *Journal of Molecular Liquid*, 223:672–677, 2016.

[98] X.J. Shi and P. Zhang. A comparative study of different methods for the generation of tetra-n-butyl ammonium bromide clathrate hydrate slurry in a cold storage air-conditioning system. *Applied Energy*, 112:1393–1402, 2013.

[99] X.J. Shi and P. Zhang. Crystallization of tetra-n-butyl ammonium bromide clathrate hydrate slurry and the related heat transfer characteristics. *Energy Conversion Management*, 77:89–97, 2014.

[100] W. Shimada, T. Ebinuma, H. Oyama, Y. Kamata, and H. Narita. Free-growth forms and growth kinetics of tetra-n-butyl ammonium bromide semi-clathrate hydrate crystals. *Crystal Growth*, 274:246–250, 2005.

[101] P. Skovborg and P Rasmussen. A mass transport limited model for the growth of methane and ethane gas hydrates. *Chemical Engineering Science*, 49:1130–1143, 1994.

[102] E.D. Sloan and C.A. Koh. *Clathrate hydrates of natural gases.* Boca Raton, London, Newyork, 3rd edition, 2008.

[103] W. Song, R. Xiao, C. Huang, S. He, K. Dong, and Z. Feng. Experimental investigation on TBAB clathrate hydrate slurry flows in a horizontal tube: forced convective heat transfer behaviors. *International Journal of Refrigeration*, 32:1801–1807, 2009.

[104] W. Song, R. Xiao, C. Huang, S. He, K.J. Dong, and Z.P. Feng. Experimental investigation on TBAB clathrate hydrate slurry flow in a horizontal tube: Forced convective heat transfer behaviors. *International Journal of Refrigeration*, 32:1801–1807, 2009a.

[105] W.J. Song, R. Xiao, S.H. Huang, C.and He, K.J. Dong, and Z.P. Feng. Study on sonocrystallization of TBAB aqueous solution. In *8th IIR Conference on Phase Change Materials and Slurries for Refrigeration and Air Conditioning*, Karlsruhe, Germany, 2009b.

[106] M.R. Talaghat. Enhancement of the performance of modified stach as a kinetic hydrate inhibitor in the presence of polyoxides for simple gas hydrate formation in a flow mini-loop apparatus. *Journal of Natural Gas Science and Engineering*, 18:7–12, 2014a.

[107] M.R. Talaghat. Experimental investigation of induction time for double gas hydrate formation in the simultaneous presence of the PVP and L-Tyrosine as kinetic inhibitors in a mini flow loop apparatus. *Journal of Natural Gas Science and Engineering*, 19:215–220, 2014b.

[108] R. Tamme, T. Bauer, J. Buschle, D. Laing, H. Müller-Steinhagen, and W.D. Steinmann. Latent heat storage above 120°c for applications in the industrial process heat sector and solar power generation. *International Journal of Energy Research*, 32:264–271, 2008.

[109] H. Teng, A. Yamasaki, and Y. Shindo. Stability of the hydrate layer formed on the surface of a CO_2 droplet in high-pressure low-temperature water. *Chemical Engineering Science*, 51:4979–4986, 1996.

[110] D.G. Thomas. Transport characteristics of suspension: VIII. a note on the viscosity of newtonian suspensions of uniform spherical particles. *Journal of Colloid Science*, 20:267–277, 1965.

[111] A.T. Trueba, I.R. Radovic, J.F. Zevenbergen, C.J. Peter, and M.C. Kroon. Kinetic measurements and in situ raman spectroscopy study of the formation of tbaf semi-hydrates with hydrogen and carbon dioxide. *Internal Journal of Hydragen Energy*, 38:7326–7334, 2013.

[112] K.A. Udachin, C.I. Ratcliffe, and J.A. Ripmeester. Structure, composition, and thermal expansion of CO_2 hydrate from single crystal x-ray diffraction measurements. *Journal of Physical Chemistry B*, 105:4200–4204, 2001.

[113] J. Vlahakis, H.S. Chen, M. Suwandi, and A. Barduhn. *Report:The growth rate of ice crystals: Properties of carbon dioxide hydrate, a review of properties of 51 gas hydrates.* Syracuse University, United States, 1972.

[114] V.K. Walker, H. Zeng, H. Ohno, N. Daraboina, H. Sharifi, S. Alireza Bagherzadeh, S. Alavi, and P. Englezos. Antifreeze protein as gas hydrate inhibitors. *Canadian Journal of Chemistry*, 2015.

[115] F.S.K. Warnakulasuriya and W.M. Worek. Heat transfer and pressure drop properties of high viscous solutions in plate heat exchangers. *International Journal of Heat Mass Transfer*, 51:52–67, 2008.

[116] J.J. Waycuilis and S.D. York. Production of gas hydrate slurry using a fluidized bed heat exchanger. *United States Patent 2002*, page 6350928.

[117] M. Wendland, H. Hasse, and G. Maurer. Experimental pressure-temperature data on three- and four-phase equilibria of fluid, hydrate and ice phases in the system carbon dioxide-water. *Chemical Engineering Data*, 44:901–906, 1999.

[118] Y. Xie, G. Li, D. Liu, N. Liu, Y. Qi, D. Liang, K. Guo, and S. Fan. Experimental study on a small scale of gas hydrate cold storage apparatus. 2010.

[119] R. C. Xin and M.A. Ebadian. The effects of Prandtl numbers on local and average convective heat transfer characteristics in helical pipes. *Heat Fluid Flow*, 18:482–488, 1997.

[120] Y. Yan and T. Lin. Evaporation heat transfer and pressure drop of refrigerant R-134a in a plate heat exchanger. *Journal of Heat Transfer, Transactions of ASME*, 121:118–127, 1999.

[121] D. Yang, L.A. Le, R.J. Martinez, R. Currier, and D.F. Spencer. Kinetics of CO_2 hydrate formation in a continuous flow reactor. *Chemical Engineering*, 172:144–157, 2011.

[122] J. Yang and B. Tohidi. Characterization of inhibition mechanisms of kinetic hydrate inhibitors using ultrasonic test technique. *Chemical Engineering Science*, 66:278–283, 2001.

[123] S.O. Yang, I.M. Yang, Y.S. Kim, and C.S. Lee. Measurement and prediction of phase equilibria for water+CO_2 in hydrate forming conditions. *Fluid Phase Equilibria*, 17:75–89, 2000.

[124] A. Yokozeki. Solid-liquid-vapor phases of water and water-carbon dioxide mixtures using a simple analytical equation of state. *Fluid Phase Equilibria*, 222-223:55–66, 2004.

[125] J.H. Yoon, Y. Yamamoto, T. Komai, and H. Haneda. Rigorous approach to the prediction of the heat of dissociation of gas hydrates. *Industrial and Engineering Chemistry Research*, 42:1111–1114, 2003.

[126] M. Yousif. Effect of under-inhibition with methanol and ethylene glycol on the hydrate control process. In *In proceedings of the Offshore Technology Conference*, Houston, Texas, 1996.

[127] Z. Youssef, L. Hanu, T. Kappels, A. Delahaye, L. Fournaison, C. Zambrana, and C. Pollerberg. Experimental study of single CO_2 and mixed CO_2 + TBAB hydrate formation and dissociation in oil-in-water emulsion. *International Journal of Refrigeration*, 46:207–218, 2014.

[128] H. Zak. Air-conditioning in office buildings. Master thesis, TU Delft, The Netherlands, 2015.

[129] P. Zhang and Z.W. Ma. An overview of fundamental studies and applications of phase change material slurries to secondary loop refrigeration and air conditioning systems. *Renewable and sustainable energy reviews*, 16:5021–5058, 2012.

[130] P. Zhang, Z.W. Ma, and R.Z. Wang. An overview of phase change material slurries: MPCS and CHS. *Renewable Sustainable Energy Review*, 14:598–614, 2010.

[131] P. Zhang, X.J. Shi, and Z.W. Ma. Solid fraction determination in cold storage by tetra-n-butyl ammonium bromide clathrate hydrate slurry. *International Journal of Refrigeration*, 36:809–819, 2012.

[132] P. Zhang and J. Ye. Experimental investigation of forced flow and heat transfer characteristics of phase change material slurries in mini-tubes. *International Journal of Heat and Mass Transfer*, 79:1002–1013, 2014.

[133] H. Zhou, I.E.E. de Sera, and C.A. Infante Ferreira. Modelling and experimental validation of a fluidized bed based CO_2 hydrate cold storage system. *Applied Energy*, 158:433–445, 2015.

[134] H. Zhou and C.A. Infante Ferreira. Effect of type-III antifreeze proteins (AFPs) on CO_2 hydrate formation rate. *Chemical Engineering Science*, 167:42–53, 2017.

[135] H. Zhou, C. Vasilescu, and C.A. Infante Ferreira. Heat transfer and flow characteristics during the formation of TBAB hydrate slurry in a coil heat exchanger. *International Journal of Refrigeration*, 64:130–142, 2016.

SUMMARY

The research presented in this thesis focuses on the use of hydrate slurries in the air conditioning and refrigeration areas. Both experimental and mathematical methods have been used. Hydrate slurries have been suggested as promising cold storage materials that can be used in air conditioning systems due to their high latent heat (193 kJ/kg and 387 kJ/kg for the hydrates studied in this thesis) and positive phase change temperature (12.5 °C and 8.0 °C for the hydrates studied in this thesis). However, large scale industrial applications of hydrate slurries are still very limited. This suggests that more research efforts should be devoted to the demonstration of its advantages.

In the first part of the thesis, the importance of cold storage for energy saving purposes has been presented. Additionally, the selection of candidate methods of cold storage is discussed. Properties, for instance thermal properties, of hydrate slurries make them an attractive option for this application. The generation methods for hydrate slurries are also introduced. Plate heat exchangers and fluidized bed exchangers are proposed as favourable generators for the production of hydrate slurries. The application of these two generators is presented in Chapter 3 and Chapter 4 respectively. Coil tube heat exchangers are also used in this thesis taking economic reasons into consideration.

In the second part of the thesis, the investigation of tetra-butyl-ammonium-bromide (TBAB) hydrate slurries has been presented. In Chapter 2, a coil heat exchanger is used to produce TBAB hydrate slurries. It is experimentally demonstrated that it is possible to operate the coil heat exchanger up to crystal mass fractions of 40 wt%. The flow and heat transfer characteristics of the TBAB hydrate slurries have been investigated. The thickness of the crystal layer on the exchanger wall has also been studied. Chapter 3 focus on the application of TBAB hydrate slurries in an air conditioning system of a space of medium size (ca. 144 m^2). A plate heat exchanger is used as the slurry generator. Hydrate growth rate on the exchanger wall has been investigated by using a hydrate growth prediction model. Compared to the conventional air conditioning systems, which make use of water as distribution medium, the system making use of TBAB hydrate slurries shows a significant improvement (73.5%) of the energy efficiency.

In the third part of the thesis, the investigation of CO_2 hydrate slurries has been presented. Chapter 4 studies the production and application of CO_2 hydrate slurries in a similar way as discussed in the second part. The main dif-

ference is that a fluidized bed heat exchanger is used instead of a plate heat exchanger as a generator. Similar results are obtained, showing a significant improvement (43%) in the energy efficiency when slurries are used instead of the conventional air conditioning systems. When used to continuously produce CO_2 hydrate crystals and continuously extract the crystals from the system, it was possible to maintain a concentration of 35 wt% hydrate crystals in the solution. In closed loop operation, solid concentrations up to 40% could be attained.

In Chapter 5, the coil heat exchanger discussed in Chapter 2 is used to produce CO_2 hydrate slurries. However, the formation rate of CO_2 hydrate is too rapid to control in this generator. Therefore, a hydrate growth preventer (antifreeze proteins (AFPs)) is introduced to slow down the formation rate. The supercooling degree and the hydrate growth rate have been investigated to show the effect of these additives. Results indicate that with a low concentration of AFPs (10 ppm), hydrate formation rate could be reduced by 35%.

In summary, two kinds of hydrate slurries have been investigated in this thesis: TBAB hydrate slurries and CO_2 hydrate slurries. The performance of these two hydrate slurries in air conditioning systems have been discussed. Significant improvements in energy efficiency for both instances have been achieved in comparison with conventional air conditioning systems. Different generators for hydrate slurry production have also been studied. Fluidized bed heat exchangers can be successfully used to produce CO_2 hydrate slurries. However, its large investment makes it less attractive. Simpler generators, like tube heat exchangers, can be used to produce TBAB hydrate slurries, but for CO_2 hydrate slurries, these systems are prone to clogging. Antifreeze proteins (AFPs) have proved to be able to slow down the formation rate of hydrate and delay the clogging. In this way, it is possible to extend the operation time before clogging takes place.

SAMENVATTING

Het onderzoek in dit proefschrift richt zich op het gebruik van hydraatslurries in airconditioning en de koudetechniek, zowel experimenteel als theoretisch. Hydraatslurries kunnen interessant zijn om te gebruiken in koudeopslag vanwege hun hoge latente warmte (193 kJ/kg en 387 kJ/kg voor de gebruikte hydraten in dit proefschrift) en een smelttemperatuur boven 0 °C (resp. 12.5 °C en 8.0 °C). In de industrie is het gebruik van hydraatslurries echter nog gering. Meer onderzoek naar de voordelen van hydraatslurries is nodig.

Het eerste deel van dit proefschrift laat het belang zien van koudeopslag en introduceert een aantal materialen die daarvoor gebruikt kunnen worden. Bepaalde eigenschappen van hydraatslurries, bijvoorbeeld thermische eigenschappen, maken hydraatslurries een aantrekkelijke optie voor toepassingen in de koudeopslag. Ook de generatoren voor de productie van hydraatslurry worden besproken. In dit proefschrift richten we ons op twee generatoren: wervelbedwarmtewisselaars en plaatwarmtewisselaars (PHE) welke worden besproken in Hoofdstuk 3 en Hoofdstuk 4. Verder worden ook spiraalwarmtewisselaars gebruikt omdat deze relatief goedkoop zijn.

In het tweede deel worden twee hoofdstukken besteed aan het onderzoek naar tetra-butyl-ammonium-bromide (TBAB) hydraatslurries. In Hoofdstuk 2 wordt een spiraalwarmtewisselaar gebruikt als generator voor de productie van TBAB-hydraatslurries. Experimenten laten zien dat het mogelijk is om de spiraalwarmtewisselaar te laten werken tot kristalmassafracties van 40%. Verder richt Hoofdstuk 2 zich op de stroming en warmteoverdracht van TBAB-hydraatslurry en wordt gekeken naar de dikte van de kristallagen die zich afzetten op de wanden van de warmtewisselaar. Hoofdstuk 3 richt zich op the toepasbaarheid van TBAB-hydraatslurries in een airconditioningsysteem voor een gemiddelde grote ruimte (ca. 144 m^2). Een PHE wordt gebruikt voor de productie van de hydraatslurry. De hydraatgroei op de wanden van de warmtewisselaar wordt bestudeerd aan de hand van een groeimodel. Vergeleken met traditionele airconditioningsystemen, welke water gebruiken als distributiemedium, laat een systeem met TBAB-hydraatslurries een aanzienlijke verbetering in de energie-efficiëntie zien (van 73.5%).

Het derde deel richt zich op CO_2-hydraatslurry. In Hoofdstuk 4 wordt gekeken naar de productie en toepasbaarheid van CO_2-hydraatslurry op dezelfde manier als in het voorgaande deel. Hier gebruiken we echter een wervelbedwarmtewisselaar. Resultaten voor deze slurry zijn vergelijkbaar met die voor TBAB. Een aanzienlijke verbetering is te zien in de energie-efficiëntie (van 43%). Het was mogelijk om een massapercentage van 35% hydraatkristallen in het medium te behouden wanneer de generator continu CO_2-hydraatkristallen produceert. In een gesloten kring konden vaste-stofconcentraties van 40% behaald worden.

In Hoofdstuk 5 wordt de spiraalwarmtewisselaar uit Hoofdstuk 2 gebruikt voor de productie van CO_2-hydraatslurries. Er wordt echter te snel CO_2-hydraat gevormd in deze generator. Daarom wordt een 'Antifreeze Protein' (AFP) toegevoegd aan het medium die deze hydraatvorming tegen moet gaan. Vervolgens wordt gekeken naar de invloed van deze AFP's op de groeisnelheid en 'supercooling degree'. Resultaten laten zien dat met een kleine concentratie AFP's (10 ppm) de groeisnelheid met 35% omlaag kan worden gebracht.

In dit proefschrift zijn twee soorten hydraatslurries bestudeerd: TBAB- en CO_2-hydraatslurries. De efficientie van deze twee hydraatslurries in airconditioning is onderzocht en laten een significante verbetering in de efficiëntie zien vergeleken met traditionele systemen. Ook verschillende generatoren voor de productie van hydraatslurries zijn aan bod gekomen. Wervelbedwarmtewisselaars kunnen gebruikt worden voor de productie van CO_2-hydraatslurry, maar de relatief hoge kosten maken die een minder aantrekkelijke optie. Eenvoudigere generatoren, zoals de spiraalwarmtewisselaar kunnen TBAB-hydraatslurries produceren maar voor CO_2-hydraatslurry kunnen deze verstopt raken. Toegevoegde AFP's aan het medium laten zien dat het mogelijk is om de groeisnelheid van hydraten te verminderen en een verstopping uit te stellen.

Curriculum Vitæ

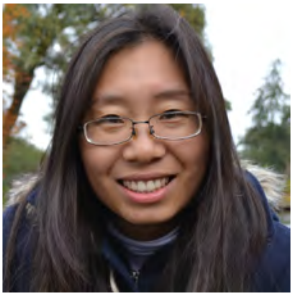

Hongxia Zhou

08-03-1986	Born in Shijiazhuang, Hebei province, China.

Education

2005-2009	Bachelor Heibei University of Technology Tianjin, China
2009-2012	Master for Chemical Engineering Guangzhou Institute of Energy Conversion Chinese Academy of Science Guangzhou, China
2012-2017	PhD. Mechanical Engineering Delft University of Technology Delft, The Netherlands

Thesis:	Hydrate slurry as cold energy storage and distribution medium
Promotor:	Prof. dr. Thijs Vlugt
CoPromotor:	dr. ir. C.A. Infante Ferreira

LIST OF PUBLICATIONS

JOURNAL PAPERS

1. **Hongxia Zhou**, **I.E.E.E. de Sera**, **Carlos Infante Ferreira**, *Modelling and experimental validation of a fluidized bed based* CO_2 *hydrate cold storage system*, Appl. Energy **158**, 433-445 (2015).

2. **Hongxia Zhou**, **Catalina Vasilescu**, **Carlos Infante Ferreira**, *Heat transfer and flow characteristics during the formation of TBAB hydrate slurry in a coil heat exchanger*, International Journal of Refrigeration **64**, 130-142 (2016).

3. **Hongxia Zhou**, **Carlos Infante Ferreira**, *Effect of type-III Anti-Freeze Proteins (*AFPs*) on* CO_2 *hydrate formation rate*, Chemical Engineering Science **167**, 42-53 (2017).

4. **Hongxia Zhou**, **Carlos Infante Ferreira**, *A real air-conditioning system using* TBAB *hydrate slurry combined with a latent heat thermal storage system*, In preparation.

CONFERENCE PAPERS

1. **Hongxia Zhou**, **Carlos Infante Ferreira**, *Design of a fluidized bed heat exchanger for* CO_2 *hydrate slurry production*, In Proceedings of 4th IIR conference on thermophysical properties and transfer processes of refrigerants, **Paper No.091**, Delft, The Netherlands (2013).

2. **Hongxia Zhou**, **Carlos Infante Ferreira**, *Influence of Anti-Freeze Proteins (*AFPs*) on the supersaturation of* CO_2 *hydrate formation*, 27th European Symposium on Applied Thermodynamics, Eindhoven, The Netherlands (2014).

3. **Hongxia Zhou**, **Carlos Infante Ferreira**, *The effect of type-III antifreeze proteins (*AFPs*) on* CO_2 *hydrate formation*, In Proceedings of the 15th International Refrigeration and Air conditioning conference, **Paper No.2405**, Purdue, USA (2014).

4. **Hongxia Zhou**, **Carlos Infante Ferreira**, *Heat transfer and flow characteristics during the formation of* TBAB *hydrate slurry*, In Proceedings of the 11th IIR Gustav Lorentzen conference on natural refrigerants, **Paper No.027**, Hangzhou, China (2014).

5. **Hongxia Zhou**, **I.E.E.E. de Sera**, **Carlos Infante Ferreira**, CO_2 *hydrate slurry production in a fluidized bed heat exchanger*, In Proceedings of the 24th IIR International Congress of Refrigeration, **Paper No.292**, Yokohama, Japan (2015).

6. **Hongxia Zhou**, **Carlos Infante Ferreira**, TBAB *hydrate slurry based latent heat thermal storage system*, In Proceedings of the 11th IIR Conference on phase change materials and slurries for refrigeration and air conditioning, **Paper No.013**, Karlsruhe, Germany (2016).
7. **Hongxia Zhou**, **Carlos Infante Ferreira**, *Investigation of hydrate growth rate on the interface between liquid and solid film*, In Proceedings of the 16th International Refrigeration and Air conditioning conference, **Paper No.2262**, Purdue, USA (2016).

ACKNOWLEDGEMENTS

It is impossible to fulfill a PhD successfully without the help of others. I am grateful to all the people that have supported me to accomplish this difficult task. First of all, I want to thank my supervisor/co-promotor Dr.ir. Carlos Infante Ferreira for providing me a PhD project position and for his excellent guidance and patience through out of the project. Carlos is an extremely nice supervisor to work with. He is always ready to talk with even though he is busy with lectures and reports. The discussions with him are always smooth and harmonious. His suggestion is always helpful and valuable. I still remember the first day I arrived at the TU Delft. He introduced me to all the people in our group, that day I was so shy and he was so happy ··· The great knowledge he possesses is what I really admire. The English of me was quite awful when I just started my PhD, the patience of Carlos gave me much courage.

Secondly I want to show my thanks to Prof. dr.ir. Thijs Vlugt, who has a cute FB profile among all my FB friends. Thijs is the leader of my group, even though we didn't talk too much, the rich knowledge he posses still encourage me a lot. I saw several times that he left office by cycling, which is never be possible in China as a professor. Thijs is also a very good father, he even shared interesting stuff of his daughter, Sophie, with group colleagues. Thanks him also for giving me this opportunity to work here.

I also want to thanks the people in the laboratory who helped me quite a lot in arranging things for my set-up, Michel van den Brink, Jaap van Raamt, Eugene Straver, without them, I could not complete my work successfully.

I would like to appreciate all the supporting staff in our department, Rob van den Boogaard, Helma Duijndam Nieuwpoort, Ilona Holstein-Pouwels, Leslie van Leeuwen, Saskia van der Meer. They have made my work in the department easier.

I also thanks the Guangzhou Elites Project of Guangzhou Municipal Government for their financial support, without which, it's impossible for me to come here for my PhD study. I would also want to thank the Koude Groep Delft/Wageningen for their financial support for the experimental facilities.

I would like to thank all my colleagues in the group of Engneering Thermodynamics (ETh). Catalina Vasilescu and Dennis Van De Bor, who have already left TU Delft, give great help in both of my research and life. Dennis helped me making floor when I moved to a new apartment which is really appreciated.

Others including Mahinder Ramdin, Mariette de Groen, Pablo Englebienne, Julia Boschan, Dion Koeze, Hassan Hashemi, Vilborg Gudjonsdottir, they have given nice talk and good suggestions. Special thanks to Remco Hens and Dion Koeze, who helped checking the Dutch writing in SAMENVATTING.

I appreciate the friendly and creative atmosphere created by many colleagues in the Process and Energy department, such as Zhaochuan Fan, Xiangmei Meng, Liyuan Fan, Likun Ma, Meng Wang and Xu Huang. Enjoying together with Chinese food in the Process and Energy canteen, which leaves me with good memories. I also thanks some friends met here in other faculties, with them, the life in the Netherlands becomes more colorful.

I also need to thanks my parents and my elder brother, without their support, I could not be able to decide to come abroad and meet so many excellent persons.

Finally to my husband Yuewei Ma. We met each other here in the Netherlands, which is definitely amazing for both of us. I have to say without him I could not be able to finish my PhD successfully, and without him, my life could not be so happy.

Hongxia Zhou
Delft, The Netherland